

**PROCESSING-STRUCTURE-PROPERTY
RELATIONSHIPS OF SURFACE POROUS POLYMERS
FOR ORTHOPAEDIC APPLICATIONS**

A Dissertation
Presented to
The Academic Faculty

By

Nathan Timothy Evans

In Partial Fulfillment
of the Requirements for the Degree
Doctor of Philosophy in the
School of Materials Science and Engineering

Georgia Institute of Technology

May 2016

Copyright © 2016 Nathan Timothy Evans

**PROCESSING-STRUCTURE-PROPERTY
RELATIONSHIPS OF SURFACE POROUS POLYMERS
FOR ORTHOPAEDIC APPLICATIONS**

Approved by:

Dr. Ken Gall, Advisor
Chair, Department of Mechanical
Engineering and Materials Science
Duke University

Dr. Meisha L. Shofner
School of Materials Science and
Engineering
Georgia Institute of Technology

Dr. Robert E. Guldberg
Woodruff School of Mechanical
Engineering
Director, Institute for Bioengineering
and Bioscience
Georgia Institute of Technology

Dr. Satish Kumar
School of Materials Science and
Engineering
Georgia Institute of Technology

Dr. David L. McDowell
School of Materials Science and
Engineering
Woodruff School of Mechanical
Engineering
Georgia Institute of Technology

Date Approved: April 1, 2016

ACKNOWLEDGEMENTS

I would first like to thank Ken Gall who was much more than just a graduate advisor. Ken taught me to think more critically and broadly, and always encouraged me to probe for deeper understanding of my work while providing a greater context of how it would apply in the real world. He taught me to become a better teacher, writer, researcher, and entrepreneur. I would also like to acknowledge my other committee members, Bob Guldberg, David McDowell, Meisha Shofner, and Satish Kumar, for giving their valuable insight and time towards my research.

While many people played a role in the completion of this work, none were as instrumental as Brennan Torstrick. Through many thoughtful discussions and travels to conferences and business plan competitions, his collaboration increased the quality of this work, and his friendship made it more fun. I would especially like to thank him for the many μ CT scans he ran on my behalf.

This work would also not have been possible without the help of the many outstanding undergraduates whom I had the chance to work with and mentor. I would like to thank Robert Carson, Katie Poynter, Haley Harris, Melissa Cross, Maxwell Young, Chase Eckert, Sangeetha Thevuthasan, Kevin Chirackal, Jenny Boothy, Annie Macedo, Cambre Kelly, Cory Turbyfield, Jacob Saban, and Joanna Gochuico for their hard work, valuable discussions, countless hours making and testing samples, and for giving me the opportunity to learn how to better mentor and lead. A special thank you to Daniel Whittingslow who was instrumental in discovering the methods used to make surface

porous PEEK, and who was always a source of encouragement and laughter. I am truly honored to have worked with every one of these individuals.

My time at Georgia Tech would not have been the same without the guidance and support of my colleagues and friends at MedShape and Vertera Spine, who are without a doubt the finest group of engineers and scientists I know. I would like to thank Kat Smith, Jack Griffis, Mateo Garcia, and Tim Nash for allowing me to learn from them and for providing valuable feedback. I would like to thank Kurt Jacobus for his generosity and wise advice about careers and life. I would like to thank Allen Chang, Stephen Lafoon, and Chris Lee for making the dream of commercializing the technology in this thesis come true. Finally, I would like to thank David Safranski and Ken Dupont for their mentorship, numerous manuscript edits, inspiration, and comradery through it all.

Many people at Georgia Tech played a critical role in the success of this research. I would like to thank Angela Lin for her help with the μ CT work, and JD Huggins for his help keeping the fatigue frame in the Hi-Bay up and running. I would like to thank the incredible MSE staff, particularly Susan Bowman, LaJuana Whitner-Bason, and Linda Roberson, for their support along the way and for getting things done in the face of bureaucratic obstacles.

A special thank you goes out to my TI:GER team – Matthew Kroge, Brad Schweizer, and Anne Hewitt – for all their efforts in seeking out a commercial opportunity for our work. Our two years of presentations, reports, and competitions together were a highlight of my time in graduate school. You each taught me to communicate more effectively and you made my research more rewarding. I would also like to thank Margi

Berbari, Marie Thursby, and Richard DiMonda for their support and guidance throughout the TI:GER program.

I must thank Solvay Specialty Polymers for their generous funding and for providing samples promptly whenever we would ask for them. A special thank you to Shawn Shorrock, Jamal El-Hibri, and Judy Melville who believed in our work and provided invaluable help along the way.

Finally, I would like to thank my family. I would like to thank my mom and dad for all their love and support. I am grateful that they taught me how to work hard, to never give up, and to have a curious mind. I would like to thank my brother and sister, Brent and Emily, for their friendship and willingness to listen to me talk about my research throughout the years. I would like to thank my in-laws, Robert and Janine Howard, who never wavered in their support, and who allowed me to marry their daughter during the beginning of graduate school. Most importantly, I would like to thank my wife, Raina. She was my biggest cheerleader and source of encouragement along the way, and she always supported me in all my endeavors. I am thankful for how well she understood my research and how proud she is of me. Her support means more to me than she will ever know.

TABLE OF CONTENTS

ACKNOWLEDGEMENTS	iii
LIST OF TABLES	viii
LIST OF FIGURES	x
LIST OF ABBREVIATIONS	xv
LIST OF SYMBOLS	xvii
CHAPTER 1: INTRODUCTION	1
1.1. Motivation	1
1.2. Research Objectives	2
CHAPTER 2: BACKGROUND	5
2.1. Structure and Properties of Polyether-ether-ketone (PEEK)	5
2.2. Use of PEEK as an Orthopaedic Implant	8
2.3. The Mechanical Properties of Polymers	16
CHAPTER 3: EXPERIMENTAL TECHNIQUES	24
3.1. Materials	24
3.2. Sample Preparation	24
3.3. Characterization	28
CHAPTER 4: THE CREATION OF A HIGH-STRENGTH SURFACE POROUS LAYER FOR IMPROVED OSSEOINTEGRATION	38
4.1. Introduction	38
4.2. Materials and Methods	40
4.3. Results	41
4.4. Discussion	47
4.5. Conclusion	54
CHAPTER 5: EFFECTS OF PORE SIZE ON THE MECHANICAL PROPERTIES AND CELLULAR RESPONSE OF SURFACE POROUS PEEK	55
5.1. Introduction	55
5.2. Materials and Methods	57
5.3. Results	59
5.4. Discussion	70
5.5. Conclusions	76
CHAPTER 6: IMPACT OF SURFACE POROSITY AND TOPOGRAPHY ON THE MECHANICAL BEHAVIOR OF HIGH STRENGTH BIOMEDICAL POLYMERS	77
6.1. Introduction	77
6.2. Materials and Methods	81
6.3. Results	82

6.4.	Discussion	95
6.5.	Conclusion	109
CHAPTER 7: MECHANICAL PROPERTIES OF THE SURFACE POROUS LAYER OF PEEK-SP		110
7.1.	Introduction	110
7.2.	Materials and Methods	112
7.3.	Results	113
7.4.	Discussion	122
7.5.	Conclusions	127
CHAPTER 8: CONCLUSIONS		129
REFERENCES		136
VITA		156

LIST OF TABLES

Table 2.1. Definition of terms on a stress-strain curve	17
Table 3.1. Structures of polymers used in this study	25
Table 4.1. Molecular weight distribution.....	42
Table 5.1. Pore size, strut spacing, strut thickness, porosity, interconnectivity, and thickness values of the surface porous layer of PEEK-SP of various pore sizes. * p < 0.01 vs SP-250, ^ p < 0.05 versus SP-350 (1-way ANOVA, Tukey). Mean ± S.D.	61
Table 5.2. Measured load-bearing tensile strength, total area tensile strength, failure strain, load-bearing tensile modulus, and total area tensile modulus of PEEK-IM and PEEK-SP. The load-bearing area, A _{LB} , includes only the cross-sectional area of the polymer materials, ignoring void area. The total area, A _T , assumes void area contributes to load bearing area and is thus the measured sample dimensions. * p < 0.01 versus IM, ^ p < 0.05 versus SP-250 (1-way ANOVA, Tukey). Mean ± S.E.	66
Table 6.1. The effects of surface roughness on the in vitro response of osteoblasts and human mesenchymal stem cells (hMSCs). The roughness (Ra) of rough samples in these studies ranged from 2-7µm and the smooth comparisons from 0.2-0.6µm.....	78
Table 6.2. Tensile strength, failure strain, elastic modulus, and toughness values of the polymers used in this study (n=5). Values represent the average ± one standard deviation.	83
Table 6.3. Surface roughness values (R _a in µm) of the surface roughened polymers tested compared to injection molded samples (n=5). Values represent the average ± one standard deviation.	83
Table 6.4. Strut spacing, strut thickness, percent porosity, and pore layer thickness of the surface porous polymers used in this study. Values represent the average ± one standard deviation.....	85
Table 6.5. Measured strength, failure strain, modulus, and toughness of the polymers with different surface conditions (n=5). Values represent the average ± one standard deviation. (* designates statistical difference between modified samples and injection molded samples, # between longitudinal and transverse samples, and ^ between transverse and surface porous with p<0.05).	88
Table 6.6. Percent crystallinity of PEEK with various thermal processing histories as measured by FTIR and DSC. Values represent the average ± one standard deviation. * designates statistical difference between groups and IM (p<0.01) and ^ significance between SP-QA180 and SP-QA300 (p<0.05).	93

Table 6.7. Measured strength, failure strain, and modulus of the polymers with different thermal processing histories (n=5). Values represent the average \pm one standard deviation. (* designates statistical difference between surface porous samples and injection molded samples and # between the quenched/annealed samples and the as-processed PEEK-SP with $p < 0.05$).	94
Table 6.8. Measured strength, failure strain, and modulus of samples tested to understand whether topographical effects were cumulative. Values represent the average \pm one standard deviation.	95
Table 7.1. Pore morphology of PEEK-SP samples used in compression testing.	113
Table 7.2. Modulus and yield strength of the PEEK-SP samples tested in this study. Values represent the average \pm one standard deviation.	114
Table 7.3. Shear strength and modulus of fully porous samples with two different percent porosities.	119
Table 7.4. Measured mass loss after 100 cycles. No significant differences were found between any of the samples.	120

LIST OF FIGURES

Figure 1.1. The materials science paradigm	2
Figure 2.1. Chemical structure of PEEK	5
Figure 2.2. Representative stress-strain curves of injection molded PEEK	7
Figure 2.3. S-N curve of injection molded PEEK	7
Figure 2.4. Typical stress-strain curve of a thermoplastic polymer.....	16
Figure 2.5. Stress-strain curve for amorphous plastic.....	18
Figure 2.6. Stress-strain curve for a semi-crystalline polymer	19
Figure 2.7. Deformation mechanism for semi-crystalline polymers	20
Figure 3.1. A schematic of the surface porous processing. (1) Polymer samples are placed on a bed of salt (t_0) and heated under pressure for the desired time (2 and 3, t_1). Once the polymer is extruded through the salt spacing, samples are cooled at a controlled rate (4, t_2) and then leached in deionized water (5). The final structure consists of a solid core with a thin porous surface layer (6). Introduction of surface porosity results in expansion of the total construct, indicated by the change in height, Δh	25
Figure 3.2. Temperature profiles of the oven and mold for a representative processing sample.	26
Figure 3.3. Representative force as a function of displacement for a sample processed on the hotplate.....	27
Figure 3.4. The modeled 2D temperature field across the height of the sample.	27
Figure 3.5. Schematic of the PEEK-SP cross-sectional areas used in stress calculations. The processing increases cross-sectional areas due to the creation of pores. However, the load-bearing area, A_{LB} , is representative of the initial area of PEEK material, assuming volume conservation. The total area, A_T , is the sum of the load-bearing area and the area of the pore network, A_{PORE}	31
Figure 3.6. Schematic of the interfacial shear testing setup.	34
Figure 4.1. Microstructural characterization of PEEK-SP: (a) μ CT reconstruction of PEEK-SP structure showing representative pore layer cross-section. Note the cubic pore morphology due to cubic sodium chloride crystals. Scale bar is 1 mm. (b) Strut spacing histogram as characterized by micro-CT. (c,d) SEM micrographs of the PEEK-SP pore network. Images confirm cubic pore morphology and pore interconnectivity detected by μ CT.	42

Figure 4.2. Representative stress-strain curves of solid PEEK and PEEK-SP calculated using both A_{LB} and A_T 43

Figure 4.3. S-N curve comparing the fatigue behavior of PEEK-SP using the load-bearing, A_{LB} , and the total area, A_T , to solid PEEK, PMMA, and bulk porous tantalum tested by another group [111]. Arrows denote tests that were halted after reaching 10^6 cycles (solid PEEK, PEEK-SP), which is defined as the runout stress. 44

Figure 4.4. Interfacial shear strength of PEEK-SP compared to smooth PEEK and sintered PEEK-BP with the shear strength of trabecular bone shown in the shaded region [112]. Asterisks (*) indicate $p < 0.05$ 45

Figure 4.5. μ CT reconstructions of bone growth into PEEK-SP and adjacent to smooth PEEK surfaces (dashed boxes) at 6 and 12 weeks show the extent of bone ingrowth. Images are oriented with the lateral side on top. Insets show magnified views of ingrown bone. PEEK implants are not depicted due to thresholding difficulties of μ CT reconstructions. An angled view is presented to visualize the extent of bone intrusion into the porous surface layer. Note the cubic morphology of bone in the surface porous PEEK samples, suggesting complete growth into the cubic pores. Scale bars on μ CT images are 1 mm. 46

Figure 4.6. Bone ingrowth of PEEK-SP and smooth PEEK surfaces: (a,c) Representative histological images of fibrous tissue formation on smooth PEEK faces at six and twelve weeks, respectively. (b,d) Representative histological images of bone ingrowth within PEEK-SP faces at six and twelve weeks, respectively. Osteoid stained deep red; mineralized bone stained green; fibrous tissue stained light orange; and PEEK material is seen in brown. (e,f) Representative mineral attenuation maps from μ CT at approximately the same cross sections as (c,d). Blue represents lower mineral density and red indicates high mineral density. Scale bar is 200 μ m. 48

Figure 4.7. Ashby plot of elastic moduli and ultimate strengths for several orthopaedic biomaterials and bone that have been reported in the literature [8, 17, 107, 115-119]. Solid-filled ellipses represent fully dense materials and porous-filled ellipses represent porous materials. While cortical bone does possess low porosity, it is grouped with the fully dense materials for this comparison. Each material, with the exception of porous tantalum and polyether-ketone-ketone (PEKK), has both solid and porous properties included to illustrate the reduction in properties due to porosity. PEEK-SP is indicated by a porous layer outlining the solid-filled circle. Superscript 't' refers to materials tested in tension and 'c' indicates compression. Daggers (\dagger) indicate yield strengths where ultimate strength was not reported. Pound signs (#) indicate bending modulus when elastic modulus was not reported. Asterisks (*) indicate values tested by our group. Ellipse central location and size represents reported mean and plus or minus one standard deviation, respectively, where available. 50

Figure 5.1. Pore size histograms as characterized by μ CT for (A) PEEK-SP-250, (B) -SP-350 and (C) -SP-450. Dotted lines represent Gaussian fits of each data set. 60

Figure 5.2. Representative μ CT reconstructions of the surface and cross section of PEEK-SP. PEEK-SP-250 is shown on the left, PEEK-SP-350 in the middle, and PEEK-SP-450 on the right. Scale bar is 1mm.	61
Figure 5.3. Functionally graded porosity with the pore size decreasing from $\sim 500\mu\text{m}$ to $\sim 200\mu\text{m}$ over the 5mm pore layer thickness.	62
Figure 5.4. Pore size as a function of layer thickness in the functionally graded sample.	62
Figure 5.5. Bimodal pore size distribution for sample processed with two different salt crystal sizes.	63
Figure 5.6. μ CT reconstructions of PEEK-SP showing variations in pore layer thickness.	63
Figure 5.7. Optical microscope image showing a PEEK-SP HA composite.	63
Figure 5.8. Representative stress-strain curves of PEEK-IM and PEEK-SP.	65
Figure 5.9. S–N curves comparing the fatigue behavior of PEEK-IM and PEEK-SP of different pore sizes. Arrows denote tests that were halted after reaching 10^6 cycles which was defined as the runout stress.	65
Figure 5.10. Interfacial shear strength of PEEK-SP compared to the strength of the PEEK-IM contacting adhesive, with the shear strength of trabecular bone shown in the shaded region [112, 151]. $\forall p < 0.001$ versus all SP groups (1-way ANOVA, Tukey). Mean \pm S.E.	67
Figure 5.11. (A) hOB and (B) hMSC proliferation measured by DNA incorporation of EdU 48 hours after seeding on smooth PEEK, PEEK-SP of various pore sizes, Ti6Al4V and TCPS. $\forall p < 0.01$ versus all SP groups (1-way ANOVA, Tukey). Mean \pm S.D.	68
Figure 5.12. (A) MC3T3 mediated calcium deposition on PEEK-SP groups compared to smooth PEEK, Ti6Al4V and TCPS in growth media and osteogenic media. HEK cell and acellular cultures were used to determine the extent of noncell mediated mineralization. Osteo: $\forall p < 0.001$ versus all SP groups; Acellular: $\# p < 0.001$ versus all groups, $* p < 0.05$ (2-way ANOVA, Tukey). (B) DNA content of parallel cultures on the same groups as in (A). Growth: $\% p < 0.001$ versus all PEEK groups; Osteo: $** p < 0.01$ (2-way ANOVA, Tukey) (C) ALP activity of same-well cultures as (B). Osteo: $\wedge p < 0.05$ versus all SP groups, $\# p < 0.01$ versus all groups, $* p < 0.05$. (2-way ANOVA, Tukey). Mean \pm S.D.	69
Figure 5.13. VEGF secretion from MC3T3-E1 cells on PEEK-SP groups compared to machined smooth PEEK, Ti6Al4V and TCPS in growth media and osteogenic media. $\forall p < 0.05$ versus all SP groups, $* p < 0.05$ (2-way ANOVA, Tukey). Mean \pm S.D.	70

Figure 6.1. Representative images of the surface of PEEK taken via the LEXT microscope: (A) injection molded, (B) longitudinally roughened, (C) transversely roughened, and (D) surface porous.	84
Figure 6.2. Representative μ CT reconstructions of the surface and cross section of PEEK-SP.	84
Figure 6.3 Representative stress-strain curves of the polymers with different surface conditions: (a) PEEK, (b) PEEK/PPSU, (c) PPSU, (d) PC, (e) PES, (f) PPS.	86
Figure 6.4. The change in toughness with various surface topographies relative to injection molded samples.	89
Figure 6.5. S–N curves comparing the fatigue behavior with various surface conditions: (a) PEEK, (b) PPSU, (c) PEEK/PPSU, (d) PC, (e) PES, (f) PPS. Arrows denote tests that were halted after reaching 10^6 cycles for PEEK samples and 10^5 cycles for the other polymers, which is defined as the runout stress.	90
Figure 6.6. Representative stress-strain curves of PEEK with various thermal processing histories.	94
Figure 6.7. (A) The percent decrease in toughness from injection molded samples with longitudinal roughness as a function of the ratio of the upper to lower yield strength. (B) The percent decrease in toughness from injection molded samples with surface porosity as a function of the failure strain of injection molded samples.	98
Figure 6.8. Percent decrease in strength of polymers with the creation of a surface porosity versus the fracture toughness.	102
Figure 6.9. (A) Endurance limit of commercial alloys (aluminum, steel, titanium, zinc, and magnesium alloys) versus yield strength. (B) Endurance limit of the polymers used in this study versus yield strength.	103
Figure 6.10. Normalized endurance limit of the polymers used in this study versus fracture toughness.	104
Figure 7.1. Stress-strain response of PEEK-SP-350 relative to the response of just the solid and pore layer components only.	114
Figure 7.2. Stress-strain behavior of the pore layer isolated from the stress-strain response of PEEK-SP. The response demonstrates the typical three staged response of porous foam materials: linear elasticity (i.e. bending), plastic yielding (i.e. buckling), and densification.	115
Figure 7.3. (a) Experimental modulus of PEEK-SP samples compared to the theoretical modulus predicted by Equation 1. (b) Experimental yield strength of PEEK-SP samples compared to the theoretical yield strength predicted by Equation 2.	116

Figure 7.4. Microstructural response of PEEK-SP to deformation. (a) Plot of average percent porosity versus strain with the stress-strain plot included for comparison. The red line is a representative stress-strain curve from Figure 7.1 demonstrating good agreement between the two tests. Error bars represent \pm one standard deviation. (b) Plot of average strut spacing versus strain \pm one standard deviation. 117

Figure 7.5. μ CT reconstructions of the porous layer at various strains. 118

Figure 7.6. Characterization of the pore structure as a function of deformation in three regions of a representative sample: bottom 1/3 of pore layer at the pore-solid interface, middle 1/3 of pore layer, and top 1/3 of pore layer at pore-air interface. (a) Percent porosity as a function of strain. (b) Strut spacing as a function of strain. 119

Figure 7.7. Images of the surface before and after abrasion. (a) Pictures of the surface before and after abrasion. 120

Figure 7.8. Representative μ CT reconstructions of surfaces before and after abrasion. (A) Cross-section of PEEK-SP-250 pre-abrasion. (B) PEEK-SP-250 post-abrasion. (C) Surface of PEEK-SP-250 pre-abrasion. (D) Surface of PEEK-SP-250 post-abrasion. .. 121

Figure 7.9. Relationship between the percent porosity and the pore layer thickness. 124

Figure 7.10. Percent porosity as a function of normalized pore depth for the thinnest pore layer (0.69 mm) and thickest pore layer (2.79 mm). 126

LIST OF ABBREVIATIONS

PEEK	polyetheretherketone
PMMA	polymethylmethacrylate
PC	polycarbonate
PPSU	polyphenylsulfone
PPS	polyphenylene sulfide
PES	polyethersulfone
MRI	magnetic resonance imaging
CT	computed tomography
HA	hydroxyapatite
B-TCP	β -tricalcium phosphate
CF	carbon fiber
TCPS	tissue culture polystyrene
μ CT	microcomputed tomography
BV	bone volume/material volume
TV	total volume
SEM	scanning electron microscope
GPC	gel permeation chromatography
DSC	differential scanning calorimetry
FTIR	fourier transform infrared spectroscopy
ATR	attenuated total reflectance
SP	surface porous
BP	bulk porous

IM	injection molded
PDI	polydispersity index
FDA	Food and Drug Administration
VEGF	vascular endothelial growth factor
MSC	mesenchymal stem cells
BMP	bone morphogenetic protein
PRP	platelet-rich plasma
TGF	transforming growth factor
hOB	human femoral osteoblasts
ALP	alkaline phosphatase
DNA	deoxyribonucleic acid
HEK	human embryonic kidney
ECM	extracellular matrix

LIST OF SYMBOLS

T_g	glass transition temperature
T_c	crystallization temperature
T_m	melting temperature
X_c	percent crystallinity
H_f	enthalpy of fusion
H_c	enthalpy of fusion of fully crystalline samples
A_{lb}	load-bearing area
A_t	total area
A_{pore}	area of pore network
M_n	number average molecular weight
M_w	weight average molecular weight
E	Young's modulus
V_f	pore volume fraction
σ_y	yield strength

SUMMARY

Polyetheretherketone (PEEK) is the material of choice in many orthopaedic applications including spinal interbody fusion and soft tissue repair. Despite its widespread clinical use, PEEK often fails to integrate with the surrounding bone and tissue which can lead to implant loosening and ultimately failure. A novel surface porous structure has been proposed, where limiting the porosity to the surface will maintain the mechanical properties necessary for load bearing applications while providing a surface for improved osseointegration.

To meet the overall goal of creating a surface porous structure, this work is divided into three aims: (1) to develop a process to create a surface porosity on polymeric implants and reliably control the porous architecture, (2) to understand the effect of surface porosity structure on the monotonic and cyclic properties of PEEK, and (3) to determine the effect of an extruded surface porosity and topography on the monotonic and cyclic properties of a broad range of thermoplastic polymers with various chemistries and crystallinities.

The initial chapters demonstrate the ability to reliably create surface porous PEEK (PEEK-SP) using a melt extrusion and porogen leaching process. Careful control of the processing parameters including the temperature, time, displacement/force, and porogen size/shape resulted in tunable porous microstructures optimized for bone ingrowth. The pore layer thickness and pore size were systematically varied and the pore network was highly interconnected. These chapters also explored the bulk mechanical properties of PEEK-SP. It was shown that the surface porosity results in samples with significantly decreased failure strain but that samples still strained past their yield; in addition, the

strength was highly preserved. No change in modulus was observed. Fatigue testing demonstrated that the surface porosity resulted in a decrease in fatigue strength.

Chapter 6 explored the effect of surface porosity and surface roughness on the mechanical properties of a range of thermoplastics with varying chemistries and crystallinities and showed that there is a great disparity in the notch sensitivity of polymers that correlates to the polymers fracture toughness. The link between polymer structure and the ability to maintain strength with notches was studied and it was found that amorphous polymers with large ratios of upper to lower yield points are more notch sensitive while crystalline polymers with smaller differences between their upper and lower yield strength maintained their strength and ductility to a greater degree. In all cases, the greatest effect of notches was the decrease in failure strain and toughness; strength was affected to a much smaller degree. Notches also resulted in a large decrease in the fatigue strength of the polymers. In all cases, the decrease in fatigue strength was greater than the decrease in monotonic strength.

Chapter 7 investigated the deformation mechanics of the pore layer. Compressive testing revealed that the pore layer deforms in the typical three staged linear elastic, plastic, and densification stages characteristic of porous materials. There was no effect of pore size on the observed properties and all the experimental moduli and yield strengths decreased with increasing porosity and were in good agreement with foam theory. *In situ* μ CT compression revealed that the pore layer can be deformed to 50% strain and still maintain over 70% of the original pore volume for bone ingrowth. Abrasion testing demonstrated that PEEK-SP does not wear at a higher rate than smooth PEEK but instead the pores deform and collapse with no subsequent increase in particle shedding.

Finally, preliminary data demonstrated the ability of PEEK-SP to promote osseointegration. Cells grown on PEEK-SP had greater proliferation and mineralization compared to smooth PEEK and Ti6Al4V, suggesting enhanced differentiation. These results were independent of pore size and suggested the ability of PEEK-SP to facilitate bone ingrowth and improve the integration of the implant. The potential of PEEK-SP was further demonstrated by implantation in a rat femoral segmental defect model. Histological examination and μ CT analysis provided evidence of bone ingrowth as early as 6 weeks. The degree of fibrous encapsulation in and around the porous surface was greatly reduced in comparison to the smooth PEEK surfaces also implanted. Furthermore, the morphology of the ingrown bone was cubic in nature, suggesting complete growth into the cubic pores.

CHAPTER 1

INTRODUCTION

1.1. Motivation

Polymeric implants provide many advantages over their metal counterparts for orthopaedic applications including post-operative MRI compatibility and a modulus close to that of natural bone. Polyether-ether-ketone (PEEK) is one such material. First developed for use in the aerospace industry due to its high strength-to-weight ratio, PEEK has been used as a biomaterial in orthopaedic, spinal, and trauma applications since the late 1980s [1]. In addition to its outstanding mechanical properties, PEEK also is very resistant to chemical, thermal, and radiation degradation. Because it is a thermoplastic it can be processed relatively cheaply by injection molding and it can easily be machined.

PEEK has been most widely used as a material for intervertebral fusion devices in spinal fusion surgery and in anchors for soft tissue fixation. In fact, PEEK is the most common material used in the \$1.1 billion interbody fusion device market and is the second most common material in the \$500 million suture anchor market [2]. It has also replaced metallic implants in many other applications including craniofacial and foot and ankle and is emerging as a material choice in dental and total joints. However, because PEEK is inert and has low surface energy due to its hydrophobic surface, there is very little cell adhesion and implants suffer from poor osseointegration [1, 3, 4]. There is therefore great clinical and scientific interest in improving the integration with bone and the surrounding tissue.

To promote the osseointegration of PEEK, many avenues have been explored, including the control of surface roughness [4], the use of composites [5-10], coatings [11,

12], and plasma treatments [13, 14]. Many of these techniques have shown promising results *in vitro* and *in vivo*, but have many drawbacks associated with them such as scalability, stability after sterilization, and a decrease in mechanical properties [5, 15, 16]. One promising solution is the introduction of porosity and studies have shown increased integration of porous PEEK with bone [15]. However, there is a severe decrease in mechanical properties (strength, failure strain, fatigue life) with increasing porosity. Despite its widespread use, no current technique used to increase the osseointegration of PEEK maintains the favorable properties of the implant while realizing improved integration with the bone and surrounding tissue.

1.2. Research Objectives

The *overall goal* of this research is to create a thin porous surface layer on a solid PEEK device that maintains the structural integrity necessary for load-bearing applications. The structure-processing-property (**Figure 1.1**) relationships are systematically studied to create an implant material that optimizes the potential for osseointegration and best preserves PEEK's mechanical properties.

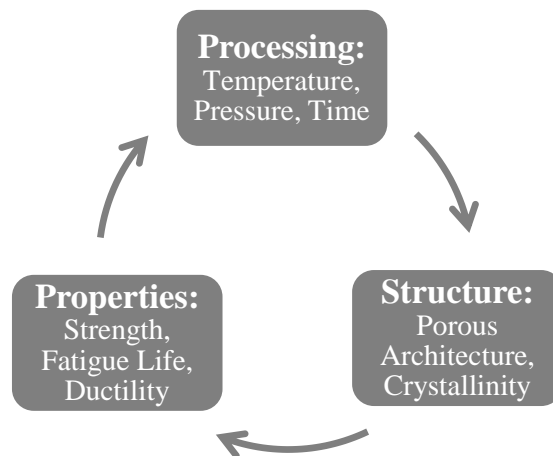


Figure 1.1. The materials science paradigm

A few preliminary biological results will be studied to demonstrate the potential for improved osseointegration. To help elucidate the effect of a surface porosity on the properties of PEEK, the surface porous processing is performed on a variety of polymers. The research objectives of this thesis have been divided into three specific aims:

Specific Aim I: Develop a process to create a surface porosity on polymeric implants and reliably control the porous architecture by varying the processing conditions.

The porous architecture can be altered by controlling the porogen size and shape. Furthermore, it is demonstrated that by systematically varying the time, temperature, and pressure at which the polymer is processed, the surface porous structure can be further controlled to yield optimal pore depth, interconnectivity, and total porosity.

Specific Aim II: Understand the effect of surface porosity structure on the monotonic and cyclic properties of PEEK.

Porosity has been shown to increase the osseointegration of implants as it stimulates osteogenesis [17]. However, as porosity increases, the structural integrity of an implant decreases as load-bearing area is lost and stress concentration effects are introduced. Using the process developed in Aim I, surface porous PEEK samples with highly interconnected pores of a controlled size and layer thickness were created. These samples were tested in monotonic tension, tensile fatigue, compression, shear, and wear to determine the effects of surface porosity on the properties of PEEK.

Specific Aim III: Determine the effect of an extruded surface porosity and topography on the monotonic and cyclic properties of a broad range of thermoplastic polymers with varying chemistries and crystallinities.

To provide better understanding the effect of extruded surface porosity on PEEK, the melt extrusion and porogen leaching process was used to create a surface porosity on five other polymers: polycarbonate (PC), poly (phenyl sulfone) (PPSU), poly (phenylene sulfide) (PPS), poly (ether sulfone) (PES), and 50/50 PEEK/PPSU blend. The resulting samples were tested in monotonic tension and compared to PEEK; selected surface porous polymers were also be run in fatigue. In addition, the effect of surface roughness on the tensile properties of the polymers was also studied. Correlations between the decreases in properties from the addition of porosity with known material properties are drawn.

CHAPTER 2

BACKGROUND

2.1. Structure and Properties of Polyether-ether-ketone (PEEK)

Polyether-ether-ketone (PEEK) is a semi-crystalline linear polycyclic aromatic thermoplastic with a unique combination of physical and mechanical properties. A member of the polyaryletherketone family, PEEK has an aromatic molecular backbone, with combinations of ketone and ether functional groups between the aryl rings. The chemical formula of PEEK is shown in **Figure 2.1**.

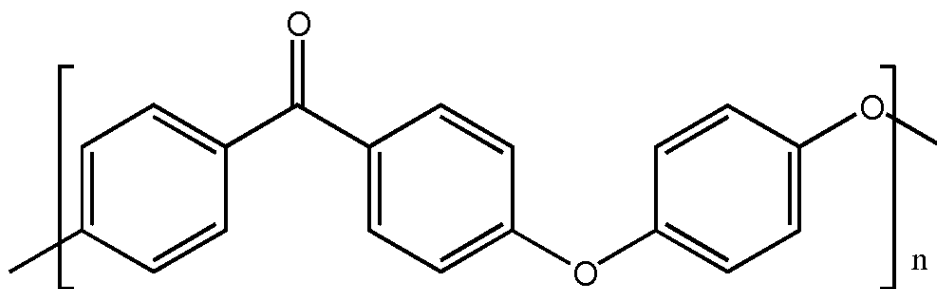


Figure 2.1. Chemical structure of PEEK

PEEK is typically 20-35% crystalline and therefore has a two-phase morphology consisting of crystalline regions dispersed in amorphous regions [18]. However, a broader range of crystallinities (0-40%) can be produced, depending on the prior processing. The PEEK unit cell dimensions have been reported as $a = 7.75 \text{ \AA}$, $b = 5.86 \text{ \AA}$, and $c = 10.0 \text{ \AA}$, resulting in a crystal density of 1.400 g/cm^3 [19]. As a semi-crystalline polymer, PEEK has three typical thermal transitions: a glass transition ($T_g \approx 150^\circ\text{C}$), crystallization temperature ($T_c \approx 285^\circ\text{C}$), and a melting temperature ($T_m \approx 340^\circ\text{C}$).

The structure of PEEK confers outstanding chemical resistance. The resonance stabilized chemical structure of PEEK results in delocalization of higher orbital electrons along the entire macromolecule, making it extremely unreactive and inherently resistant to chemical, thermal, and post-irradiation degradation [1]. After polymerization, PEEK is chemically inert and insoluble in all conventional solvents at room temperature, with the exception of 98% sulfuric acid. In addition to its chemical resistance, PEEK displays remarkably high resistance to gamma and electron beam radiation which are commonly used sterilization processes [20-22]. The inertness and stability of PEEK helps explain its biocompatibility and lack of toxicity [23, 24].

The mechanical properties of PEEK, like any thermoplastic polymer, are influenced by both temperature and strain rate [25-27]. The main effect of strain-rate is an increase in modulus with an increase in the rate of deformation. However, in clinical applications, strain rate should not be of primary concern for PEEK biomaterials [1]. Within the context of biomaterial applications, where the expected operating thermal environment is around 37°C (body temperature), the elastic behavior of PEEK is relatively insensitive to temperature [1]. The yielding, plastic flow, and fracture behavior of PEEK, however, display greater sensitivity to test temperature below the glass transition than elastic properties. The mechanical behavior of PEEK is also influenced by molecular weight as well as the size and orientation of the crystalline regions [28, 29]. In general, the modulus and yield strength of PEEK increase with increasing crystallinity, but the molecular weight has no detectable effect on these properties. In contrast, both crystallinity and molecular weight independently influence the toughness. Toughness increases with increasing molecular weight and decreases with increasing crystallinity.

Though many polymers do not possess properties sufficient for load-bearing applications, PEEK's relatively high strength, modulus, and toughness make it suitable for use in applications such as soft tissue repair, spine, and craniofacial. A typical tensile stress-strain curve of PEEK is shown below in **Figure 2.2**.

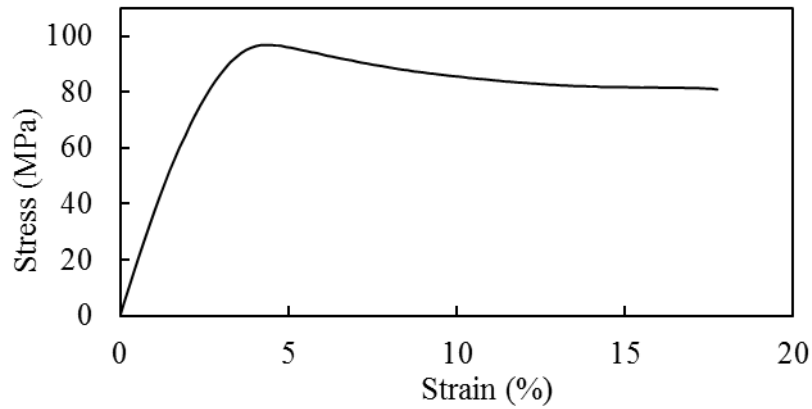


Figure 2.2. Representative stress-strain curves of injection molded PEEK

As shown, PEEK has high strength (>90 MPa), good ductility (>15%), and a modulus (3.4 GPa) in the range of human bone. In addition, PEEK has outstanding fatigue resistance which is important due to the cyclic loading experienced by orthopaedic implants (**Figure 2.3**).

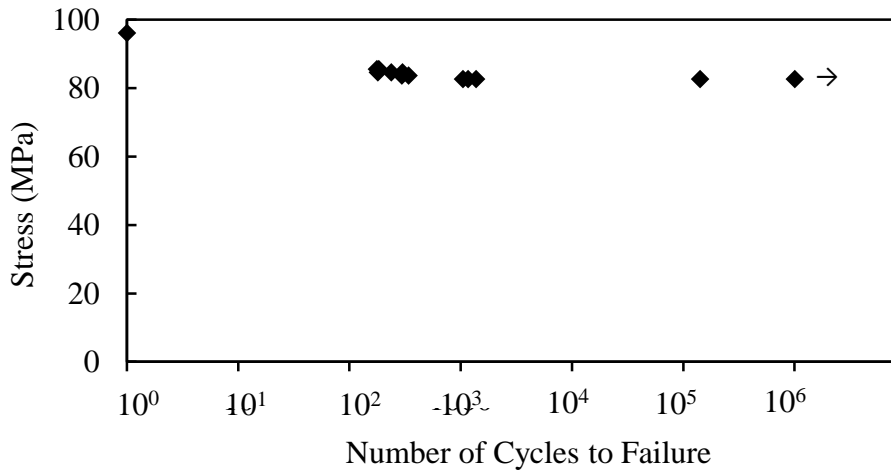


Figure 2.3. S-N curve of injection molded PEEK [30]

2.2. Use of PEEK as an Orthopaedic Implant

2.2.1. History and Current Use

The introduction of non-biological materials into the human body has taken place throughout human history [31]. From use of nacre by the Mayans and iron by early Europeans as dental implants, to use of linen by early Egyptians and metals in ancient Greece as sutures, humans have intuitively searched for implant solutions to address the loss of physiologic/anatomic function. However, prior to the 20th century, most implants had a low probability of success because of a poor understanding of biocompatibility and sterilization [31].

During the 20th century, studies on the biocompatibility of implant materials began in earnest. First generation orthopaedic implant materials were metallic as they had high strength, were widely available, and due to the lack of clear alternatives. Though many metals offered outstanding biocompatibility and osseointegration – and are still the material of choice for many applications today – they also have several drawbacks associated with them. The presence of metallic implants in MRI can cause substantial imaging artifacts including signal loss, geometric distortion, and bright pile-up artifacts [32]. Metallic implants can also prevent accurate evaluation of the region of interest near implants in CT scans due to beam hardening [33].

In addition to imaging artifacts, load-bearing metallic implants can also lead to a problem known as stress-shielding [34, 35]. Traditional orthopaedic alloys used in bone and joint reconstruction have a modulus 10 to 20 times greater than bone [36]. The mismatch between the moduli of the metal implant and the bone leads to a situation where the majority of the load is transferred through the implant rather than by the surrounding

bone. This phenomenon is widely recognized as the “stress-shielding effect” or “stress-protection”. Because bone is a living tissue with metabolic reaction, a decrease in tissue stress/strain regularly results in bone resorption. Thus, a proper amount of stress/strain is necessary for the growth of the fractured bone during its healing [37, 38]. Without the stimulus of mechanical stress to maintain its structure, the bone adjacent to the high modulus device becomes porotic and weakens which can result in implant loosening and clinical failure.

Though polymers such as rubber have also been in use for hundreds of years, it was not until the 20th century that significant changes took place in the polymer industry. Prior to World War II, natural substances such as latex, wool, and silk were available and the development of synthetics was not a needed. WWII, however, necessitated the development of new materials. During this time great advances were made in polymer science and many polymers such as nylon, acrylics, neoprene, and polyethylene began to take the place of natural materials. During the war, production of these new polymers were channeled into a host of national defense uses but after the war surgeons and scientists had an array of new implant material options. Though this time saw the use of many off-the-shelf materials to fabricate medical devices, it ushered in an era of development of materials designed specifically for biomaterial applications [31].

While many polymers were first explored for use in non-load-bearing applications such as silicone for non-clotting coatings, polyurethanes for heart valves, Teflon for vascular grafts, and polymethylmethacrylate for intraocular lenses, polymers offer many advantages over traditional metal alloys for orthopaedic use. Unlike most metals, polymers are radiolucent and therefore are compatible with standard imaging techniques. Polymers

also have a much lower modulus than metals that more closely matches bone, minimizing the effects of stress-shielding. Finally, polymers typically low cost materials and can easily be processed into complex shapes. Despite the many advantages polymers provide over metals, they often do not have the appropriate strength or fatigue resistance needed for many load-bearing orthopaedic devices.

During the 1980s, high performance thermoplastics, including PEEK, began to be explored in composites for use in trauma and hip stems [39, 40]. However, widespread commercial applications for PEEK in the human body would be first realized in the field of spine implants as a replacement for titanium fusion cages [1]. As mentioned, PEEK's high strength and toughness make it suitable for use as a load-bearing material while its modulus more closely matches the native bone. PEEK also does not prevent radiographic assessment of the bone growth, an especially important criterion for fusion surgeries. Today PEEK is the most common implant material used in interbody fusion devices and has also gained use in sports medicine, trauma, craniofacial, foot and ankle, and as a candidate in arthroplasty [1, 2].

Though numerous studies have documented the successful clinical performance of neat PEEK and PEEK composites [41-46], concern has been raised about the inertness of PEEK and its limited fixation with bone [1]. Rather than close apposition with bone, PEEK implants are often subject to the formation of a fibrous capsule around the implant [47, 48]. The lack of bone attachment at the implant surface can lead to a vicious cycle of implant micromotion and inflammation that eventually leads to the fibrous layer thickening, osteolysis (bone degradation and resorption), implant loosening, and an increased risk of revision [49-53]. By appropriately controlling the surface properties of the implant, an

improved bone-implant response can be achieved and the possibility of implant failure minimized.

2.2.2. Current Methods to Improve the Osseointegration of PEEK

Due to PEEK's aforementioned poor osseointegration and widespread use, it is of great scientific and clinical interest to develop techniques that will promote increased integration with the bone and surrounding tissue while maintaining the mechanical integrity of the implant. Current techniques include both surface and bulk modifications via chemical and physical treatments as well as composite preparation. Regardless of the modification technique, the goal of such treatments is to provide a more favorable interaction at the bone-implant interface as the implant surface is critical to implant osseointegration [54].

Topography & Surface Chemistry

It is well recognized that micrometer and nanometer sized surface features enhance the osseointegration of orthopaedic implants [55]. In fact, the surface topography of substrates is often more essential than their surface chemistry for protein adsorption and the subsequent adhesion and proliferation of cells [56, 57]. Studies have shown an excellent correlation between the average surface roughness of titanium implant surfaces and bone apposition [58], pushout failure load [59], and growth factor and cytokine release by osteoblasts [60]. Indeed, it has been concluded that high surface roughness is important to achieve a stable long-term osseointegration of implants [53]. PEEK has also shown a

differentiated *in vivo* response when comparing machined and injection molded samples [4].

Several techniques have been used to introduce a topologically varied surface on PEEK implants. Prolonged exposure of PEEK to oxygen plasma can lead to etching of the surface creating peaks and valleys [61], while chemical etching caused PEEK's surface to become irregular with higher roughness [13]. Exposure of PEEK to an atmospheric-pressure argon plasma jet with varying admixtures of molecular oxygen resulted in an increase in the O/C ratio and the surface roughness of PEEK [62]. In addition to the advantageous increase in roughness, etching and plasma treatments may lead to an increase in wettability, surface polarity, and surface oxygen concentration, factors which may increase the bone-implant interface stability. For example, plasma treatment of PEEK in N₂/O₂ environment decreased the surface contact angle from 85° to 25° and increased the oxygen concentration [63]. Surface treatment of PEEK with low-temp plasma also had a significant effect on proliferation of fibroblasts and showed osteoblastic differentiation comparable to tissue culture polystyrene [14]. Gas discharge plasmas have been used to create different nitrogen-based chemical functionalities, mainly amino groups, and resulted in faster cell adhesion and more cell spreading [64]. Plasma-immersion-ion-implantation treated PEEK demonstrated a more favorable surface for osteoblast adhesion, spreading, and proliferation in addition to early osteogenic differentiation [65]. In addition, surface modification can be made by mechanical means including machining and sandblasting.

Coatings

Coatings of PEEK not only allow for additional control of surface roughness, but also provide added chemical benefits for promoting bone integration. Several methods are

used for creating these coated polymer surfaces: thermal spray coatings coupled with sand blasting, electron-beam deposition, and ionic plasma deposition. Thermal spray deposition is the industry standard and is reliable for preserving fatigue strength and increasing osseointegration [53]. Electron-beam deposition is a low-temperature process that can provide a dense, uniform, and well crystallized coating without deteriorating the characteristics of the PEEK implant [11]. Ionic plasma deposition is a novel method used to create surface engineered metallic nanostructures and has shown increased osteoblast integration over current coating methods [12].

The two most common coatings used to promote the osseointegration of PEEK implants are hydroxyapatite (HA) and titanium coatings. HA coatings are an attractive option as it provides Ca^{2+} and PO_4^{3-} , two necessary components of osteoblast-mediated bone formation, and has been shown to convert fibrotic tissue to bone [53]. HA coated PEEK examined in the tibia, femur, and ilium of rabbits demonstrated that a HA coating significantly enhances the bone response to PEEK implants *in vitro* and *in vivo* [66, 67]. Titanium provides a good coating choice as it is often considered the material of choice in orthopaedic applications due to its favorable osseointegration [68]. Titanium strongly adheres to PEEK and greatly improves the wettability of the implants [11]. Titanium coated samples have demonstrated higher bone implant contact than uncoated PEEK controls in animal studies [69, 70] as well as improved cell adhesion, spreading, proliferation, and differentiation *in vitro* [11, 12]. Though HA and titanium coatings are most common in the literature, other coatings have been explored including diamond-like carbon coated PEEK in which changes in roughness and hydrophilicity as well as better cell response from osteoblast attachment, proliferation, and differentiation was observed [71].

Though coatings have shown promising biological responses, they can negatively impact the mechanical properties of the implants and are subject to delamination. In cyclic loading, it is possible for cracks in the coating to propagate into the substrate, subsequently lowering the fatigue strength [12]. In addition, the coatings are often brittle and have detached from PEEK during fatigue tests. Because the coating is lost in a short time, the fatigue life may resemble the uncoated samples [11] and debris particles may be harmfully introduced into the surrounding tissue. Delamination and loss of fatigue strength remain a concern for coated PEEK implants.

Composites

PEEK composites have been examined for their potential to improve the biofunctionality of PEEK implants. HA/PEEK composites are the most commonly studied composite system due to hydroxyapatite's advantageous properties. HA/PEEK composites have been shown to promote vascularization, mature bone growth, and osteoid formation in a porcine model [6] as well as apatite layers forming on or near HA spheres after 28 days of submersion in a solution of simulated body fluid [7, 72]. The addition of other calcium phosphates – such as β -tricalcium phosphate (β -TCP) and bioglass – to polymers to create composites with tailored functions has also been suggested as calcium phosphates are known to be biocompatible and bioactive [73-75]. However, addition of these fillers to PEEK causes a decrease in tensile strength, ductility, and fatigue life and an increase in modulus.

Carbon fiber (CF) is another common filler material in PEEK composites, though its use is often targeted at increasing the stiffness and load-bearing capacity of implants. Osteocalcin production on CF/PEEK samples showed no significant difference between

medical grade titanium or tissue culture polystyrene (TCPS) and alkaline phosphatase activity was similar to titanium but lower than TCPS [10], indicating that CF/PEEK composites are a suitable implant material. In a rabbit study, it was demonstrated that CF/PEEK implants provided good stability for fracture fixation plates and were well tolerated by the animals [47].

Porosity

Introducing porosity into implants is another solution to improve the osseointegration of implants. Several criteria for porous implants have been previously outlined: pores must be large enough to allow cell ingrowth and vascularization (~100–700 μm), pore interconnectivity needs to be sufficient to allow cells and nutrients to pass into and through material, and the porosity must not detrimentally decrease the structural integrity of the implant [15]. Materials and devices with porosity aid in providing a more natural biological and physical functioning, giving biomaterials the ability to allow tissue infiltration and integration. In addition to the closer replication to the host bone, porosity can enhance the fixation of devices, preventing migration or movement that causes abrasive damage to adjacent tissue. Furthermore, porosity of correct type may trigger or direct tissue repair and stimulate osteogenesis [17, 76]. Porous PEEK can also be modified through any of the previously mentioned methods such as coatings or plasma treatments to further increase the osseointegrative capacity.

Several manufacturing processes have been used to create porous PEEK including particulate leaching, rapid prototyping, and sintering. In one preliminary study, porous PEEK showed an increase in osteoconductivity in a sheep model as demonstrated by an increase in the implant-bone contact. The porous implants also increased the implant

fixation in pull-out tests [15]. However, there was a severe decrease in mechanical properties (tensile strength, strain at failure, impact strength, and fatigue strength) with increasing porosity that limits the potential for load-bearing applications.

2.3. The Mechanical Properties of Polymers

A tensile test is a simple and common test used to characterize the mechanical properties of polymeric materials. A typical stress-strain curve is shown below in **Figure 2.4** with the definition of terms in **Table 2.1**. Data generated from the stress-strain curve includes the yield strength, modulus, yield elongation, ultimate strength, toughness, and failure strain.

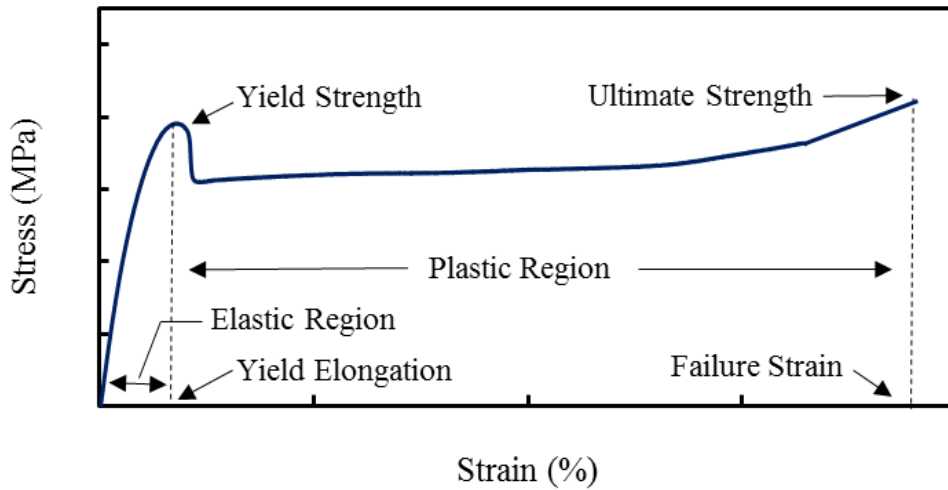


Figure 2.4. Typical stress-strain curve of a thermoplastic polymer

Table 2.1. Definition of terms on a stress-strain curve

Characteristic Points	Description
Elastic Region	The initial linear portion of the stress-strain curve before the yield point characterized by the deformation being recoverable (no permanent deformation)
Modulus of Elasticity	A measure of the stiffness of the polymer, it is the ratio of stress to strain within the elastic region of the stress-strain curve
Yield Point (strength)	The first point (load) at which the specimen yields with further deformation being permanent. At the yield point the sample begins to neck (cross-sectional area decreases)
Yield Elongation	The strain at the yield point and the amount of recoverable strain
Plastic Region	The portion of the curve after the yield point. This deformation in this region is permanent
Ultimate (tensile) Strength	The maximum stress the material can hold before failure
Failure Strain	The total elongation at fracture

Figure 2.5 shows the characteristic stress-strain behaviour for an amorphous polymer. It is characterized by a linear elastic region, a yielding followed by a drop in stress, a formation of a neck, a drawing of the neck, an increase in stress due to straightening of polymer chain, and finally fracture.

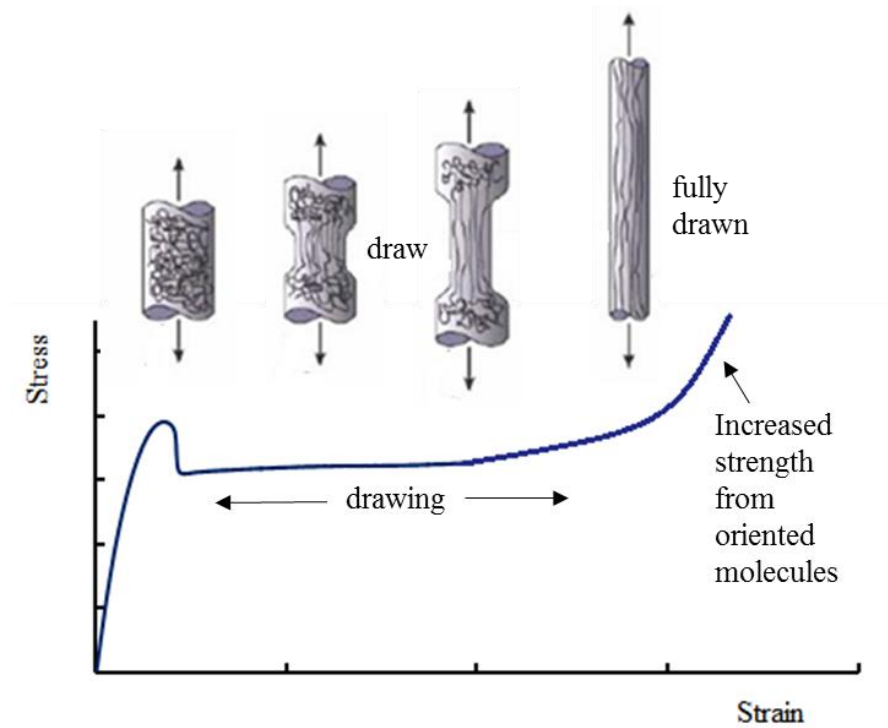


Figure 2.5. Stress-strain curve for amorphous plastic

The stress-strain behavior of semi-crystalline polymers only differs from amorphous polymers in that it lacks a drawing region. **Figure 2.6** shows the characteristic stress-strain curve for a semi-crystalline polymer. Semi-crystalline polymers are two phase materials consisting of a crystalline phase interspersed in an amorphous phase. Each region experiences different forms of deformation which can result in increased resistance to crack propagation [77-79]. During the necking or drawing stage, strain-induced crystallization can take place in the amorphous phase due to the orientation of chains in the direction of the applied load [80].

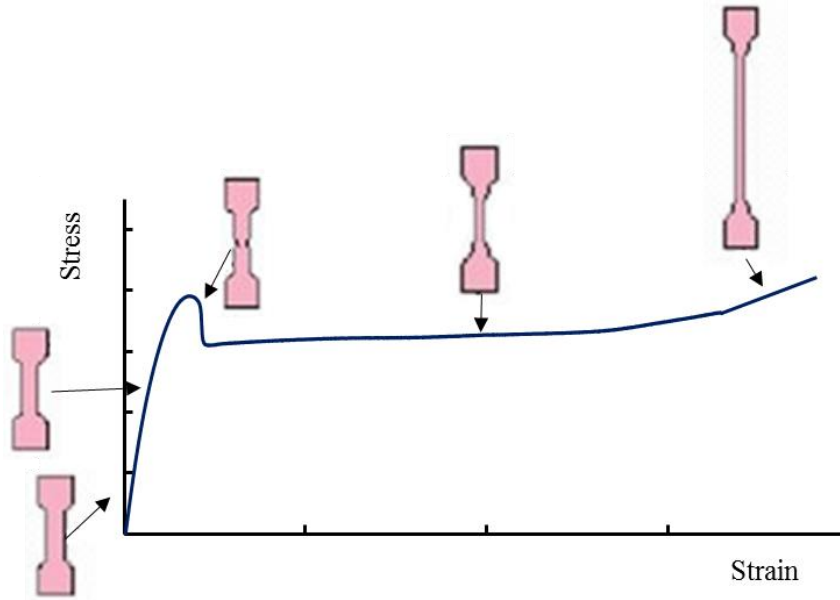


Figure 2.6. Stress-strain curve for a semi-crystalline polymer

There are two main deformation regions in a stress strain curve: elastic and plastic deformation. The elastic deformation of polymers is the result of two mechanisms. The primary mode of deformation is induced by the stretching or bending of the covalent bonds. Upon removal of the stress, the strain recovery is almost instantaneous. In polymers, elastic deformation also involves the rotation of bonds in addition to the stretching and unwinding of polymer chains in the direction of the applied load [81]. However, recovery from this deformation is time-dependent with the chains moving back to their unstressed state over seconds to months. This behavior results in the viscoelastic nature of polymers and the non-linearity in elastic behavior. Plastic deformation occurs as chains slide, stretch, rotate, and disentangle under load causing permanent deformation.

Many semicrystalline polymers have a spherulitic structure and deform in the following steps (**Figure 2.7**): (1) elongation of amorphous tie chains, (2) tilting of lamellar chain folds towards the tensile direction, (3) separation of crystalline block segments, and (4) orientation of segments and tie chains in the tensile direction.

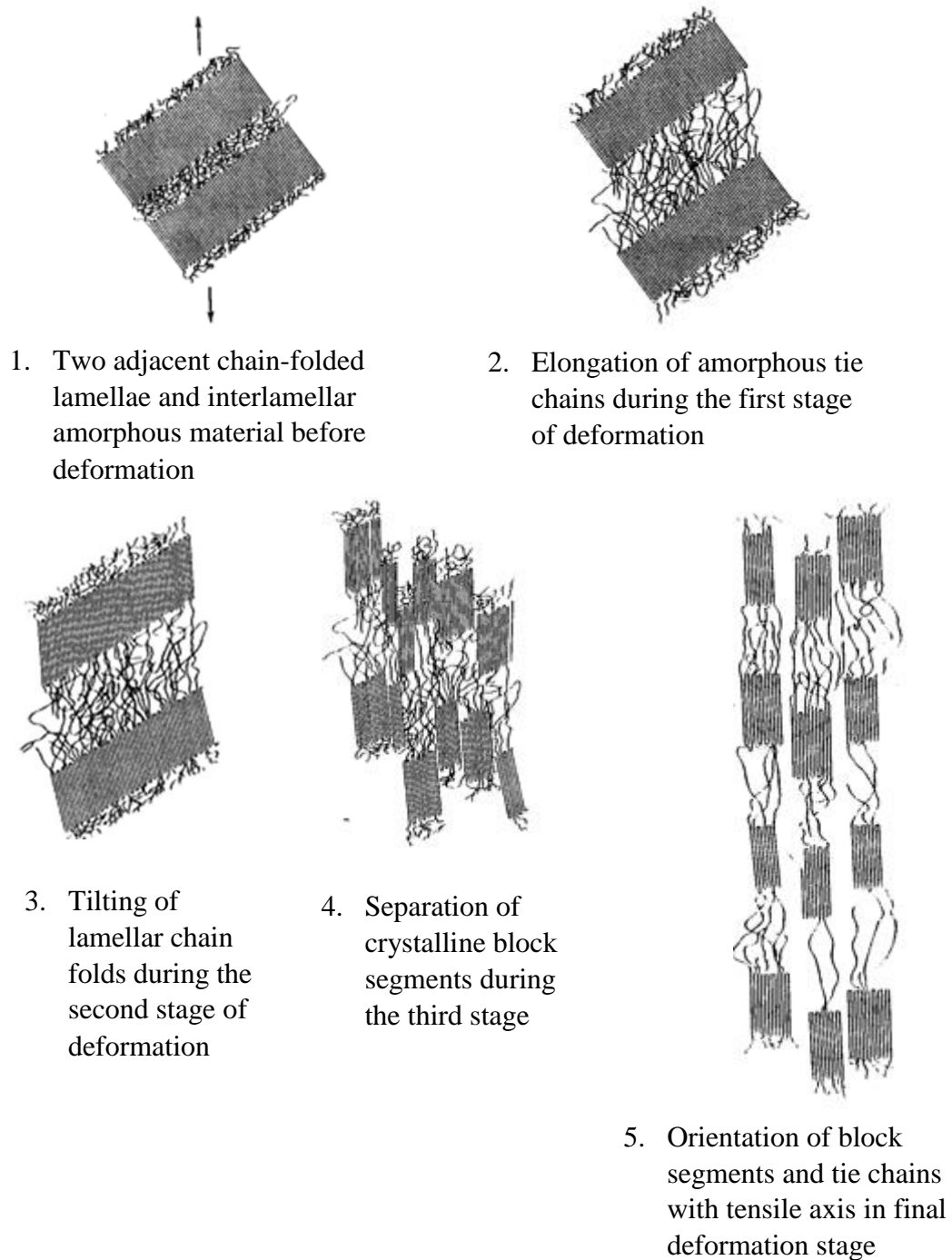


Figure 2.7. Deformation mechanism for semi-crystalline polymers

Fatigue is a common source of failure for polymers in many applications and is a concern *in vivo* where implants are subject to cyclic loading. Fatigue failure generally occurs via a two stage process [82]. The first stage, initiation, involves formation of

microcracks at inhomogeneities or defects in the material, usually at some surface stress concentration site [83]. This damage formation can occur at stress levels far below the tensile strength of the material. During the second stage, propagation, growth of the damage occurs via coalescence of microcracks and the propagation of the small cracks to form large cracks. For most polymers, the initiation time is orders of magnitude longer than the propagation time.

In general, fatigue occurs by either a mechanically dominated mechanism or a thermally dominated mechanism [82]. Polymers are extremely sensitive to the frequency of the cyclic loading due to their viscoelastic nature and are not very good conductors of heat [83]. As a result, at high frequencies or loads significant heating may occur due to the heat dissipation during testing. This hysteretic heating affects the physical and mechanical properties of the polymer and can result in thermal fatigue failure. This response is not considered to be an intrinsic response of the material to cyclic loading conditions. Failure due to thermal fatigue failure is usually ductile.

Mechanically dominated fatigue involves the nucleation of damage and its subsequent growth in the form of crazes, cavities, and microcracks until some critical crack size is reached at which catastrophic fracture occurs [82, 83]. This deformation occurs at relatively lower stresses and frequencies and is commonly referred to as high cycle fatigue. Mechanically dominated fatigue often results in brittle failure [84].

The fatigue life of a given polymer decreases with increasing applied stress due to greater damage accumulation per cycle at higher stress. Some polymers exhibit a relatively well-defined plateau in their stress-cycle (S-N) curve which is indicative of an endurance limit below which fatigue damage does not significantly accumulate and failure does not

occur. In contrast, other polymers demonstrate steadily decreasing allowable cyclic stress with an increasing number of loading cycles [82].

As mentioned, semicrystalline polymers are two phase materials consisting of a crystalline phase interspersed in an amorphous phase. Each region experiences different forms of deformation which can result in increased resistance to crack propagation [77-79], increasing the fatigue resistance of the polymer. Since damping is due to the amorphous or other disordered regions of the polymer, increasing crystallinity will also reduce damping and improve fatigue life [85]. Furthermore, increased crystallinity results in a slight increase in modulus that may contribute to improved fatigue performance.

Polymers have varying degrees of notch sensitivity. Some polymers, such as polycarbonate, are extremely notch sensitive while others, such as rubber-modified styrenes, show almost no notch sensitivity [86]. In general, the fatigue resistance of polymers is much more sensitive to surface defects than the tensile strength. The ductility is also sharply reduced by surface defects or porosity.

Many microstructural factors affect the mechanical properties of polymers. In general, anything that prevents the deformation mechanisms above will make the polymer stronger, stiffer, and less ductile [87]. Cross-linking restricts chain motion increasing the degree of covalent bonding between chains and by aligning chains resulting in more van der Waals inter-chain bonds. An increase in crystallinity increases secondary bonding as molecular chains are closely packed and parallel, increasing resistance to interchain motion. Increasing the molecular weight also causes more van der Waals attractions and as well as increased entanglements resulting in decreased chain mobility. Pre-deformation by

drawing, analogous to strain hardening in metals, increases strength by orienting the molecular chains.

CHAPTER 3

EXPERIMENTAL TECHNIQUES

3.1. Materials

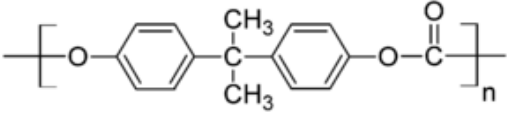
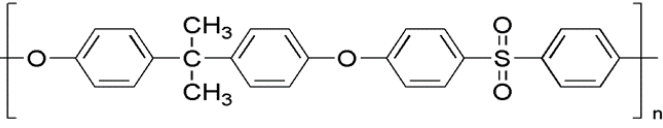
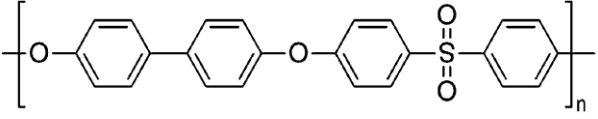
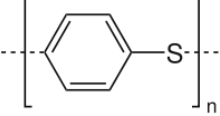
The focus of much of this thesis is on polymer polyetheretherketone (Zeniva® 500, Solvay Advanced Polymers, Alpharetta, GA) which was described in detail in **Chapter 2**. The other polymers tested in this study include polycarbonate (PC), polyethersulfone (PES), polyphenylsulfone (PPSU), polyphenylene sulfide (PPS), and a PEEK/PPSU blend, all of which were provided by Solvay Advanced Polymers. The chemical structures are given in **Table 3.1**. Sodium chloride used in the surface porous processing was purchased from Sigma (St. Louis, MO).

3.2. Sample Preparation

3.2.1. Surface Porous Processing

Surface porous samples were created using the following method: as-received injection molded samples were placed in contact with a packed array of salt crystals and heated under pressure (**Figure 3.1**). As the polymers reached their flow temperature, flow through the salt spacing occurred resulting in the formation of the pore network. The sample was then cooled in a controlled fashion to manage solidification and crystallization and maintain mechanical properties. Embedded salt crystals were then leached using an ultrasonic cleaner, leaving behind a thin porous surface layer. Precise control of local temperature, pressure and time are required to achieve desired pore layer characteristics.

Table 3.1. Structures of polymers used in this study

Name	Structure
polycarbonate (PC)	
polyethersulfone (PES)	
polyphenylsulfone (PPSU)	
polyphenylene sulfide (PPS)	

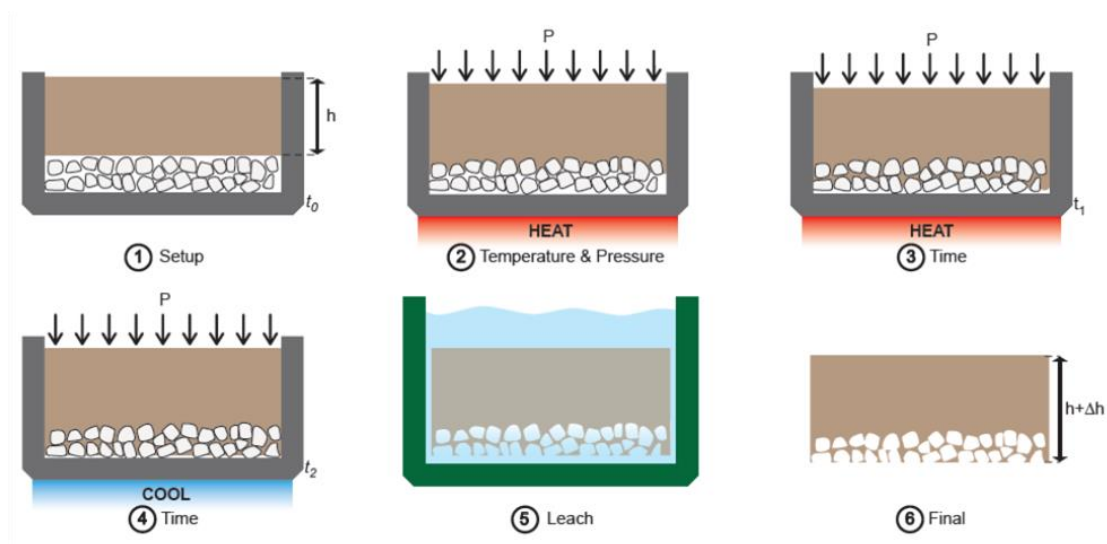


Figure 3.1. A schematic of the surface porous processing. (1) Polymer samples are placed on a bed of salt (t_0) and heated under pressure for the desired time (2 and 3, t_1). Once the polymer is extruded through the salt spacing, samples are cooled at a controlled rate (4, t_2) and then leached in deionized water (5). The final structure consists of a solid core with a thin porous surface layer (6). Introduction of surface porosity results in expansion of the total construct, indicated by the change in height, Δh .

Two methods of heating the polymers samples were used. In the first, samples were placed in an oven resulting in uniform heating across the parts and allowing large samples to be processed (i.e. Type 1 dogbones or plates for abrasion testing). A set weight was placed on the samples resulting in constant force; there was no control over flow displacement. The temperature profiles of the oven and the mold are shown in **Figure 3.2**. As shown, the samples were above melt for ~20 minutes before being removed from the oven.

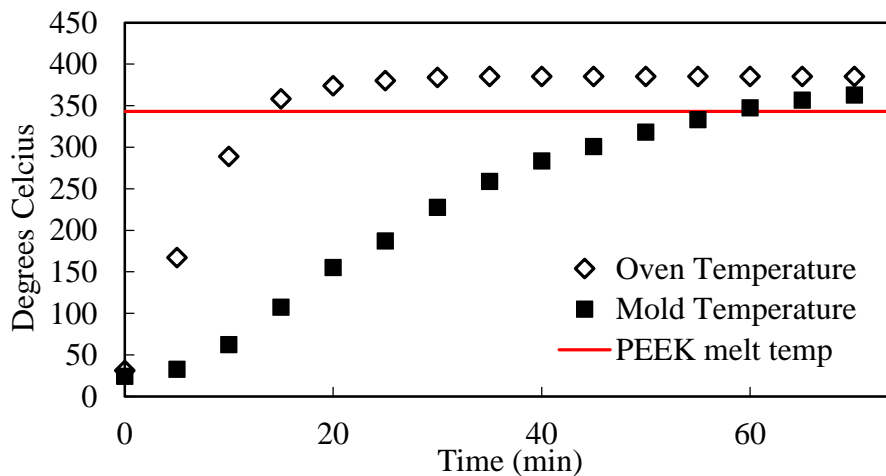


Figure 3.2. Temperature profiles of the oven and mold for a representative processing sample.

The second method of fabrication used a custom hot plate (Wenesco) and an Instron. Samples were placed in the center of the hot plate and the crosshead was used to push the PEEK through the salt crystals. This provided additional control over the flow displacement, allowing for tailorable layer thickness, and allowed tracking of the force and displacement over time (**Figure 3.3**).

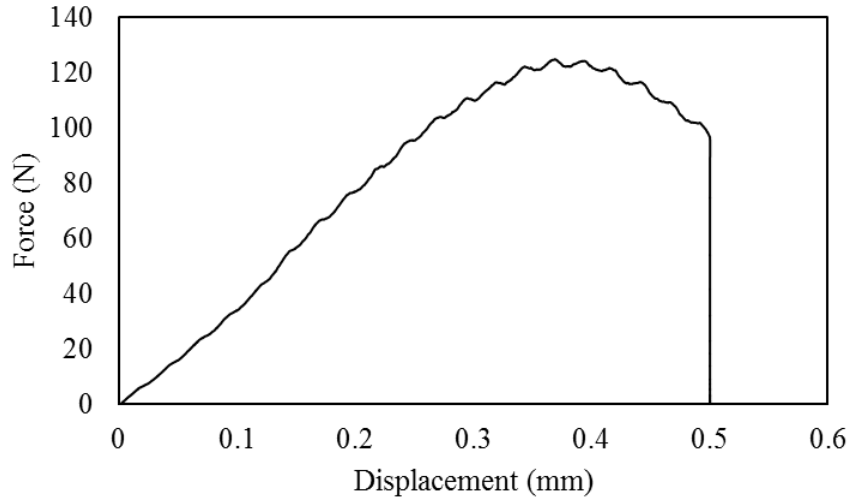


Figure 3.3. Representative force as a function of displacement for a sample processed on the hotplate.

While the two different processing methods produce surface porous samples with similar pore morphologies, the hot plate and oven method are distinctly different. Due to a small heating area, processing on the hot plate is limited to samples with surface areas below approximately 30mm x 30mm. In addition, the heating is localized rather than global. This results in only one surface of the sample reaching the flow temperature. The 2D temperature field across the height of the sample was modeled (Abaqus FEA Software, Dassault Systemes) and the results are shown in **Figure 3.4**. As the data demonstrate, the temperature quickly decreases away from the part of the sample in contact with the salt crystals.

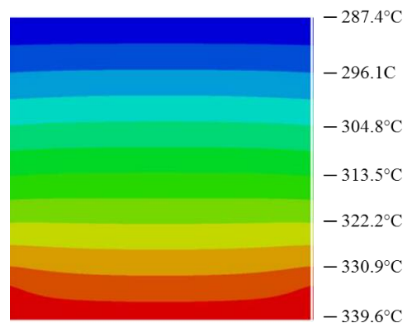


Figure 3.4. The modeled 2D temperature field across the height of the sample.

3.2.2. Bulk Porous Processing

Powder sintered bulk porous samples (PEEK-BP) were created using a compression molding technique [8]. Briefly, sodium chloride and PEEK powder (KetaSpire® KT-820FP, Solvay Advanced Polymers) were thoroughly mixed at a ratio to achieve equivalent pore size and porosity as PEEK-SP. Powder mixtures were sintered under 260 MPa compression for 60 minutes at 363°C within a 10 mm diameter cylindrical mold (Heated Manual Press, Model 4386, Carver, Inc.). Sodium chloride was leached in water and sodium chloride removal was confirmed via microcomputed tomography (μ CT).

3.2.3. Surface Roughened Specimens

Surface roughened samples were prepared by sanding the surface using 50 grit multi-purpose sandpaper. Samples were sanded \sim 0.1mm on each side using an electric sander and then hand sanded to provide a uniform finish and lay. The abrasive grooves were oriented in two directions: longitudinally (parallel to the direction of the applied load) and transversely (perpendicular to the direction of the applied load).

3.3. Characterization

3.3.1. Microarchitecture Characterization

Micro-computed Tomography Analysis

Surface porous samples were cut to size and the porous layers were scanned using μ CT (μ CT 50; Scanco Medical) at 10 μ m voxel resolution with the scanner set at a voltage of 55 kVp and a current of 200 μ A. Surface porous layers were manually contoured tightly to the pores to minimize inclusion of non-porous volume. A global threshold was applied to segment the polymer from pore space and kept consistent throughout all evaluations.

Pore layer morphometrics were evaluated using direct distance transformation methods [88]. Briefly, strut spacing was calculated using a maximal spheres method adapted from a trabecular spacing index. Porosity was determined by $1 - BV/TV$, where BV represented polymer volume and TV represented the total volume of the porous layer. Average pore layer thickness was determined using a trabecular thickness index algorithm on the filled TV of each porous layer. Pore layer interconnectivity was determined by inverting segmented pore and solid spaces and dividing the largest connected pore space volume by the total pore volume [89]. Scanning electron microscopy (SEM, Hitachi S-3700N VP-SEM) was utilized to observe the surface topography of samples. Pore size was measured from SEM images as the length of the pore diagonal (n=50).

Surface Roughness Characterization

Surface roughness measurements were made using a confocal microscope (Olympus LEXT 3D Material Confocal Microscope) (n=5). A fixed laser wavelength of 405 nm at varying objectives of 10, 20, and 50 times was used. Images of the surface topography were also captured using the LEXT microscope in both 2D and 3D representations. Surface porous samples were evaluated using micro-computed tomography (μ CT 50; Scanco 82 Medical) at 10 μ m voxel resolution with the scanner set at a voltage of 55 kVp and a current of 83 200 μ A (n = 8).

3.3.2. Thermal and Chemical Characterization

Molecular Weight Determination

To detect changes in molecular weight due to PEEK-SP processing, gel permeation chromatography (GPC) was performed by Solvay Advanced Polymers on 100 mg samples

of the isolated surface porous layer, solid core from a surface porous sample, and injection molded PEEK.

Polymer Crystallinity Measurements

To determine the crystallinity of the surface porous PEEK with various processing conditions, two different measurements were used. Differential scanning calorimetry (DSC, TA Instruments Q100) was used to calculate the percent crystallinity of samples by comparing the enthalpy of fusion of the samples to the enthalpy of fusion of the fully crystalline PEEK using the following equation where $\Delta H_{f100\%} = 130 \text{ J/g}$ [90]:

$$X_C = \frac{\Delta H_f - \Delta H_C}{\Delta H_{f100\%}}$$

To confirm the crystallinity measurements made using DSC, Fourier transform infrared spectroscopy (FTIR) was used. A Thermo Scientific Nicolet iS50 FT-IR with smart iTR attenuated total reflectance (ATR) attachment with diamond crystal was used to characterize the crystallinity. Spectra was taken from 16 scans from 400 to 4000 cm^{-1} at a resolution of 1 cm^{-1} . Crystallinity was calculated by taking the ratio of the peak heights at 1305 cm^{-1} to 1280 cm^{-1} , previously correlated by Chalmers [91].

3.3.3. Mechanical Characterization

Monotonic and Fatigue Tensile Testing

Tensile tests were performed according to ASTM D638 at room temperature using a MTS Satec 20 kip (89 kN) servo-controlled, hydraulically-actuated test frame (n=5 PEEK-SP, n=5 PEEK, n=4 PMMA). The crosshead speed was 50 mm/min. Force-displacement data as measured by the cross-head and validated by video (Canon HG10, Lake Success, NY) and image processing software (ImageJ, NIH, Bethesda, MD) was used

to calculate ultimate stress, failure strain, and elastic modulus as well as generate the stress-strain curves. The reported results are engineering stress-strains.

Fatigue tests were run at increasingly lower stresses below the ultimate stress of the samples to generate S-N curves and determine the endurance limits of the respective samples. Fatigue tests were run on the same Satec test frame in axial stress control at a frequency of 1 Hz with a sinusoidal load and an R-value of 0.05. Tests were run until failure or runout. Runout was defined as greater than 1,000,000 cycles unless noted otherwise. No temperature rise was observed during the experiments.

For monotonic and fatigue results, two representations of stress for PEEK-SP were calculated: the first using load-bearing area, A_{LB} , and the second using total area, A_T (**Figure 3.5**). Load-bearing area was taken as the cross sectional area of the as-received dog bone before porous processing. Total area was taken as the cross sectional area of the dog bone after porous processing. Use of total area produces stress values that assume void area contributes to load-bearing, and results will consequently depend on pore layer thickness and volume fraction of porosity. Conversely, load-bearing area includes only the cross-sectional area of polymer material, including solid polymer and porous strut regions, ignoring void area in the porous layer.

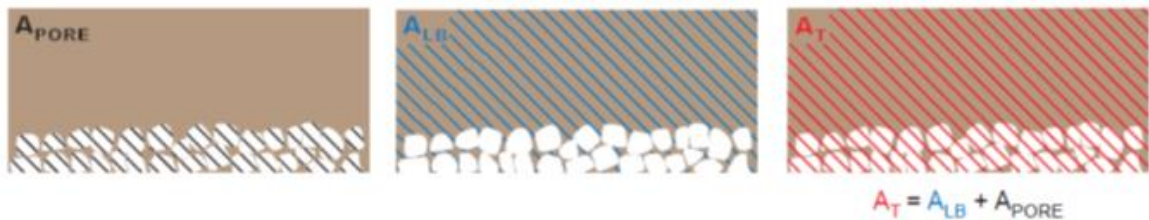


Figure 3.5. Schematic of the PEEK-SP cross-sectional areas used in stress calculations. The processing increases cross-sectional areas due to the creation of pores. However, the load-bearing area, A_{LB} , is representative of the initial area of PEEK material, assuming volume conservation. The total area, A_T , is the sum of the load-bearing area and the area of the pore network, A_{PORE} .

Compressive Testing

Cylindrical samples of approximately 16mm diameter x 16mm height were processed with a surface porous layer prepared as described. Three different pore sizes (SP-250, 350, 450) and two different pore layer thicknesses (~1mm, 2.5mm) were tested. The total sample height remained constant at 16mm. In other words, the thickness of the solid plus the thickness of the pore layer equaled approximately 16mm. The diameter and height of each sample was measured using digital calipers immediately prior to testing and all samples were scanned using μ CT to determine the percent porosity and the layer thickness. The tests were performed using an Instron machine with a 5 kN load cell at room temperature. The samples were compressed past yield of the solid component using a displacement controlled test at a rate of 1.3 mm/min according to ASTM D695-10.

To understand the mechanical properties of the pore layer, the stress-strain response of the surface porous PEEK and solid PEEK were decoupled. To do so, the stress-strain response of solid PEEK cylinders (16mm x 16mm) was measured ($n = 3$). We then made the following two assumptions: (1) the force throughout the samples is uniform (i.e. the force in the porous layer is the same as that in the solid) and (2) at a given force, the *strain* in the solid region is the same in the surface porous samples as in the solid sample alone. Based on these assumptions, we subtracted out the strain (and subsequently the displacement using the pore thickness data from μ CT) of the solid region from the SP samples leaving only the displacement-force data for the surface porous layer. The elastic modulus was then calculated for each material as the slope of the initial linear portion of each stress-strain curve ($n = 3$) and the yield using a toe correction and 2% offset.

μCT compression

To evaluate the pore morphometry as a function of stress and strain, the Scanco Medical Compression/Tension Device was used together with the Scanco Medical μCT 50. Samples were placed under a small preload (2 N, 0% strain condition) to prevent rotation during scanning and then were scanned as described previously. The compression device was then used to compress the sample to 5% strain. The samples were then rescanned and compressed to another 5% strain of the original height. This process was continued in 10% strain increments until the sample was compressed to 70% of the original height. Pore layer morphometrics were determined as described previously. Displacement control was used throughout the tests to control the strain and slight stress relaxation occurred during the duration of the scans.

Shear Testing

Due to limitations in size and geometry of processed samples, a custom test setup was used. Briefly, an 18.65mm aluminum square prism was pushed through an 18.90mm hole square tube. The wall thickness of the tube was 2.5mm. A 5mm diameter hole was drilled 5mm deep through the outer wall of the tube and into the driver (2.5mm depth in each). The driver was fixed in the upper grips of the Instron. Samples were placed in the hole and then the crosshead was lowered at 1.3mm/min pushing the driver down the tube and shearing the sample. Force, time, and displacement were recorded and were used to calculate the stress and strain.

Aligned Interfacial Shear

Interfacial shear testing was adapted from ASTM F1044-05 using 3M™ Scotch-weld™ 2214 Non-Metallic Filled as adhesive and a 30 kN load cell (Instron). A thin layer

of adhesive was applied evenly to the surfaces of shear samples and like faces were pressed together, clamped, and placed in a vacuum oven to cure at 121°C for 1 hour. The shear test fixtures were clamped in Instron jaws and adjusted to enable horizontal alignment of the shear sample. The plane of the adhesive was coincident with the axis of loading. Cured samples were placed into custom fixtures ensuring a tight clearance fit. A schematic of this setup is shown in **Figure 3.6**. The fixtures were pulled apart at 2.54 mm/min until the interfacial surfaces of the samples were completely sheared. The shear stress was calculated based on the measured failure load and cross-sectional area. Shear test groups included smooth PEEK (n=4), PEEK-SP (n=8) and PEEK-BP (n=5).

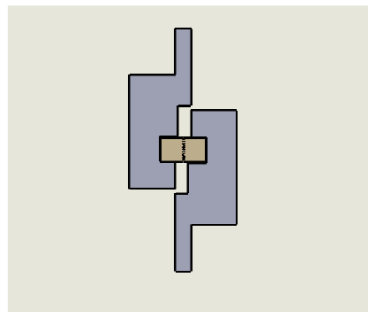


Figure 3.6. Schematic of the interfacial shear testing setup.

Abrasion Testing

The abrasion resistance of PEEK-SP was characterized according to ASTM-F1978. In short, samples 10cm² x 4mm thick with a 6.4mm hole were placed on a Taber Rotary Abraser Model 5135 (Taber Industries, North Tonawanda, NY) with H22 Calibrade wheels and a load of 250g. The samples were abraded for 2, 5, 10, and 100 cycles with the vacuum on. Between each abrasion cycle the samples were cleaned, dried, and weighed. Samples were cleaned in an ultrasonic cleaner for at least 20 minutes, dried in a vacuum oven at 100°C for 1 hour and then cooled at room temperature for 10 minutes. The samples were

then weighed 3 times. The clean, dry, and weigh cycle was repeated until the change in weight was within 0.01g and the mass loss is the measure of abrasive wear to the specimen.

3.3.4. In-vivo Characterization

Surgery

An established rat femoral segmental defect model was utilized to preliminarily assess the osseointegration potential of PEEK-SP compared to smooth PEEK surfaces [92]. This model was chosen based on its previous use in characterizing bone ingrowth in porous polymeric and metallic implants [93-96]. All surgical procedures were approved by the Institutional Animal Care and Use Committee at the Georgia Institute of Technology (IACUC protocol #A11028). Briefly, bilateral 8 mm femoral defects were made in the central diaphyses of three 13-week old female Sasco Sprague-Dawley rats (Charles River), totaling six defects. Femurs were stabilized prior to defect creation using a modular plating system consisting of a polysulfone plate and two stainless steel risers. PEEK implants with one surface porous and one smooth end face were press-fit into each defect before incision closure (n=6). The orientations of surface porous faces were alternated between contralateral limbs. After surgery animals were allowed to recover and ambulate freely. Animals were injected with slow release buprenorphine at the time of surgery to relieve any pain. One animal was euthanized at 6 weeks and the remaining two were euthanized at 12 weeks.

Ex vivo μ CT Imaging

Following euthanization, μ CT scans were performed to assess bone ingrowth into each face of the implant. Femurs were scanned at 55 kVp and 145 μ A with a 15 μ m voxel

size (Viva-CT, Scanco Medical). Three-dimensional reconstructions were created from two-dimensional slices thresholded to include mineral densities >50% of native cortical bone.

Histology

Femoral explants were fixed in formalin and stored in 70% ethanol until processing. Samples were processed through ascending grades of ethanol followed by xylene before embedding in methyl methacrylate. After embedding, rough sections were cut (Isomet[®] 1000 Precision Saw, Buehler) and then ground to 30 μm (EXAKT 400 CS). Sections were stained using a Goldner's Trichrome protocol to distinguish osteoid (red) from mineralized bone (green).

3.3.5. In-vitro Characterization

Proliferation of human femoral osteoblasts (hOB, ScienCell) and human vertebral mesenchymal stem cells (hMSC, ScienCell) was evaluated on smooth nonporous PEEK, PEEK-SP-250, PEEK-SP-350, PEEK-SP-450, Ti6Al4V, and tissue culture polystyrene (TCPS) (n = 6 per culture condition) by measuring DNA incorporation of 5-ethynyl-2'-deoxyuridine (EdU) (Click-iT[®]-EdU, ThermoFisher). hOB and hMSC were seeded at 10,000 cells/cm² in growth media (ScienCell, Carlsbad, CA) and proliferation measured at 48 hours per the manufacturer's instructions. Osteogenic differentiation was evaluated on the same six surfaces utilizing clonal mouse pre-osteoblast cells (MC3T3-E1, ATCC) due to their homogeneity, availability and differentiation profile that is more similar to human osteoblasts than other *in vitro* models [97]. MC3T3 cells were seeded at 20,000 cells/cm² in growth media composed of α -MEM (Life Technologies) supplemented with 16.7% FBS (Atlanta Biologicals, Lawrenceville) and 1% Penicillin-Streptomycin-L-glutamine (PSL,

Life Technologies). Cells were cultured under dynamic conditions using a rocker plate. After 3 days cells reached confluence and half of all samples were switched to osteogenic media comprising growth media supplemented with 6 mM β -glycerophosphate, 1 nM dexamethasone, 50 ng/ml thyroxine, 50 μ g/ml ascorbic acid 2-phosphate, and 1 nM $1\alpha,25$ -Dihydroxyvitamin D3 (Sigma). The remaining half of samples were maintained in growth media. Samples were cultured for 14 days after confluence, changing media every 3-4 days. At 14 days samples undergoing assays for alkaline phosphatase (ALP) activity and DNA content were washed with PBS ($-\text{Ca}^{2+}/-\text{Mg}^{2+}$), ultrasonically lysed in Triton X-100 (0.05%) in PBS and subjected to one freeze-thaw cycle prior to further analysis. Samples assayed for calcium were washed with PBS ($-\text{Ca}^{2+}/-\text{Mg}^{2+}$) and vortexed overnight at 4°C in 1 N acetic acid to solubilize calcium. ALP activity, an early osteogenic differentiation marker, was determined by colorimetric intensity of cell lysates exposed to p-Nitrophenyl phosphate (pNPP, Sigma) and was normalized to same-well DNA content determined by a Picogreen dsDNA assay (Life Technologies). Calcium deposition, a marker indicative of mineralization, in parallel cultures was determined by a colorimetric Arsenazo III reagent assay (Diagnostic Chemicals Ltd.). To determine the extent of non-cell-mediated mineral deposition, the assay was also performed on acellular control samples and on samples seeded with a non-mineralizing cell line (Human Embryonic Kidney (HEK)). HEK cells were seeded to reach confluency at the same 3 day time point as MC3T3 cultures. Both acellular and HEK controls were cultured under osteogenic conditions. Vascular Endothelial Growth Factor (VEGF) production by MC3T3-E1 cells was measured from culture media at day 14 after confluence using an ELISA and normalized to same-well DNA content (R&D Systems).

CHAPTER 4

THE CREATION OF A HIGH-STRENGTH SURFACE POROUS LAYER FOR IMPROVED OSSEOINTEGRATION

4.1. Introduction

The ultimate goal of most medical implants is to restore impaired biological function and achieve functional integration with the body. Several porous polymers and other tissue engineered scaffolds have made advances in this regard for many soft tissue applications where mechanical loading is minimal [98]. However, similar solutions in high load-bearing orthopaedic environments remain elusive due to performance tradeoffs in clinically adopted biomaterials. Metallic implants provide high strength but are associated with medical imaging artifacts and unwanted bone resorption due to their high modulus and corresponding stress shielding [99]. Current porous polymer scaffolds can facilitate bony ingrowth but lack the strength necessary for high load-bearing environments experienced in clinical soft tissue reconstructions, spinal fusions, and arthrodesis applications [8, 100]. Bioresorbable polymers and composites facilitate osseointegration and implant resorption, but are clinically limited to soft tissue reconstructions and have cited incidences of prolonged inflammation, migration, incomplete degradation, and implant breakage [101].

As a relatively new implant material, polyether-ether-ketone (PEEK) has gained widespread acceptance as a high-strength polymer used primarily in spinal fusions and soft tissue reconstructions, with favorable imaging compatibility and stiffness that closely matches bone [1, 102]. However, PEEK suffers a key property tradeoff in poor osseointegration. Its aromatic backbone and semi-crystalline nature provide high strength

and biocompatibility, yet its hydrophobic and chemically inert surface limits local bone attachment [36, 103].

Basic research approaches to enhance PEEK osseointegration have focused both on surface modification and bulk porosity. Surface modifications such as plasma or chemical etching [13, 14, 63], addition of bioactive coatings [11, 104], and PEEK composites have performed well *in vitro* and *in vivo* [105], yet their clinical success may be limited due to their potential instability and delamination in physiological or surgical environments [16, 61]. Introducing bulk porosity throughout PEEK implants via powder sintering (or compression molding) aims to increase implant fixation by encouraging the migration and proliferation of various cell types to enhance vascular and bone tissue ingrowth [8, 106]. Indeed, porous PEEK implants have exhibited increased osseointegration [105]; however, they also suffered up to 86% reduction in strength due to the high overall fraction of porosity and the relatively weak local bonds created during powder sintering [8, 15, 107].

Limiting porosity to PEEK's surface could promote osseointegration and maintain bulk mechanical properties [15]. Furthermore, a surface porosity approach is supported by the finding that a completely porous structure may not be required for functional integration [15, 108]. A porous surface layer could retain implant strength, provide an adequate conduit for bone ingrowth, and avoid tissue necrosis common at the center of large fully porous implants in cases of limited vascular and nutrient supply [109, 110].

This chapter investigates a novel method to create a functionally graded PEEK material with a balance between surface porosity for osseointegration and a solid core for mechanical load-bearing. Porous and solid regions are seamlessly connected, resulting in outstanding mechanical properties compared to powder sintering or coatings [8]. Samples

are created using a technique in which PEEK is extruded through sodium chloride crystals to create a surface porosity. The resulting structure and properties of the surface porous PEEK are discussed as well as preliminary *in vivo* results to provide initial insight into its potential to osseointegrate.

4.2. Materials and Methods

4.2.1. Materials

Surface-porous PEEK (PEEK-SP) samples were created by extruding medical-grade PEEK through the open spacing of sodium chloride crystals and powder sintered bulk porous samples (PEEK-BP) were created using a compression molding oven technique as described in **Chapter 3**. To control for pore size, sodium chloride was sieved into a range of 200–312 μm using #50 and #70 US mesh sieves. Injection-molded PEEK samples (PEEK) were used as smooth controls. All tensile specimens were ASTM D638 Type I dog-bone samples. Shear samples were cut from PEEK bars to have a cross-sectional shear area of 16 mm x 16 mm for PEEK and PEEK-SP or 10 mm diameter for PEEK-BP. *In vivo* implants were 5 mm diameter cylinders machined to a length of 8 mm from PEEK bars. One face was made surface porous while the other face was machined smooth as a control. A hole was bored through the center to replace the native medullary cavity. Characterization of the pore microstructure and crystallinity was performed as outlined in **Chapter 3**.

4.2.2. Methods

Tensile tests, fatigue tests, interfacial shear tests, and *in vivo* examination were carried out according to the methods outlined in **Chapter 3**.

4.2.3. Statistical Analysis

Comparisons between the strength and modulus of PEEK-SP and solid PEEK were performed with a Student's t-test. The results of the interfacial shear test were analyzed using a one-way ANOVA and Tukey post hoc analysis (95% confidence interval). All data is expressed as average \pm standard deviation.

4.3. Results

4.3.1. Pore Layer Characterization

Pore morphology reliably correlated to sodium chloride crystal size (200-312 μm) and cubic nature with a pore size of 280 ± 32 μm (**Figure 4.1**). The pore layer was $67.3\pm 3.1\%$ porous and highly interconnected ($99.9\pm 0.1\%$) with an average strut spacing of 186.8 ± 55.5 μm as determined by μCT . Interconnectivity values are potentially skewed slightly higher than actual values due to spatial resolution imaging limitations that may have prevented detection of thin walls between pores. However, pore interconnectivity was expected to be high due to water's high degree of pore accessibility during leaching, as evidenced by the absence of residual sodium chloride on μCT . The average thickness of the pore layer was 399.6 ± 63.3 μm .

Table 4.1 shows the molecular weight of the polymer from the surface porous region, a solid region from a surface porous sample, and injection molded PEEK. The results demonstrate that the surface porous processing does not change the molecular weight of the samples.

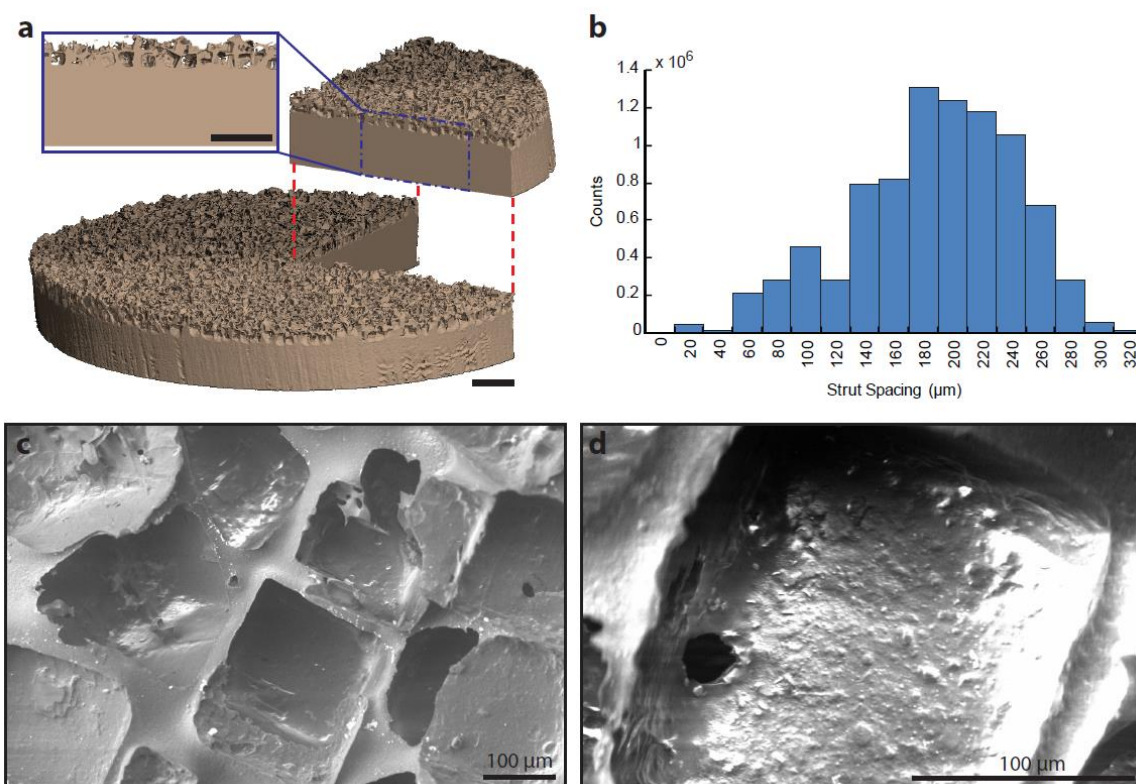


Figure 4.1. Microstructural characterization of PEEK-SP: (a) μ CT reconstruction of PEEK-SP structure showing representative pore layer cross-section. Note the cubic pore morphology due to cubic sodium chloride crystals. Scale bar is 1 mm. (b) Strut spacing histogram as characterized by micro-CT. (c,d) SEM micrographs of the PEEK-SP pore network. Images confirm cubic pore morphology and pore interconnectivity detected by μ CT.

Table 4.1. Molecular weight distribution.

	M_n (g/mol)	M_w (g/mol)	PDI ^d
Porous^a	44 753	100 032	2.24
Solid^b	45 717	99 449	2.18
As-received^c	46 208	98 846	2.14

^a Porous region of PEEK-SP

^b Solid region of PEEK-SP

^c Injection molded PEEK without surface porous treatment

^d Polydispersity index, $PDI = M_w/M_n$

4.3.2. Tensile Monotonic Testing

The creation of a surface porosity did not significantly decrease the strength of samples compared to injection molded controls when using A_{LB} ($p=0.52$). The ultimate tensile strength (σ_{UTS}) and elastic modulus of PEEK-SP samples were 96.11 ± 2.61 MPa and 3.36 ± 0.30 GPa compared to 97.7 ± 1.0 MPa and 3.34 ± 0.14 GPa for unprocessed solid PEEK controls, respectively, using A_{LB} (**Figure 4.2**). However, failure strains were decreased from 20.24 ± 2.43 to 7.79 ± 2.25 . When the total area was used in stress calculations, PEEK-SP retained 73.9% of the strength and 73.4% of the elastic modulus of solid PEEK, corresponding to a tensile strength of 71.06 ± 2.17 MPa and modulus of 2.45 ± 0.31 GPa for a porous layer that comprises approximately 20% of the sample cross sectional area.

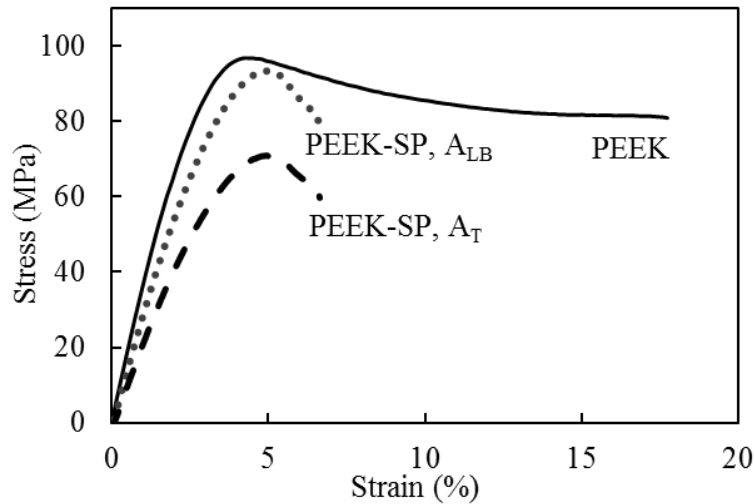


Figure 4.2. Representative stress-strain curves of solid PEEK and PEEK-SP calculated using both A_{LB} and A_T .

4.3.3. Tensile Fatigue Testing

PEEK-SP samples demonstrated high fatigue resistance regardless of which area was used in stress calculations ($\sigma_N = 60.0$ MPa for A_{LB} and $\sigma_N = 45.3$ MPa for A_T) (**Figure**

4.3). Further, the fatigue strength of PEEK-SP (A_{LB}) was 73% of the σ_{UTS} of smooth, injection-molded PEEK. Both PEEK and PEEK-SP experienced higher fatigue strength at similar cycle number than PMMA.

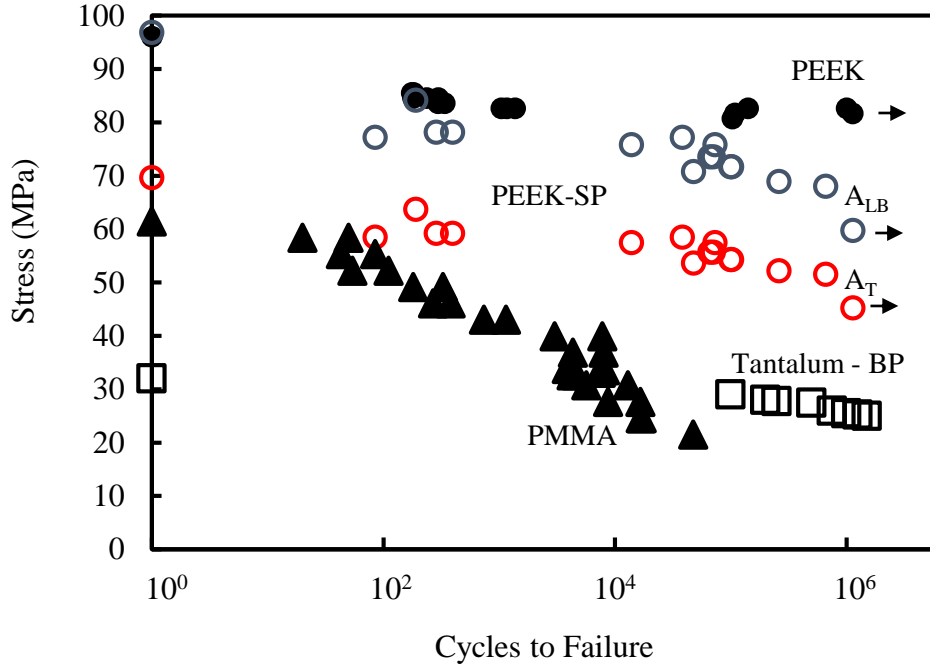


Figure 4.3. S-N curve comparing the fatigue behavior of PEEK-SP using the load-bearing, A_{LB} , and the total area, A_T , to solid PEEK, PMMA, and bulk porous tantalum tested by another group [111]. Arrows denote tests that were halted after reaching 10^6 cycles (solid PEEK, PEEK-SP), which is defined as the runout stress.

4.3.4. Aligned Interfacial Shear

The average shear strength of smooth PEEK, PEEK-SP, and PEEK-BP was 7.52 ± 3.64 , 23.96 ± 2.26 , and 6.81 ± 0.81 MPa, respectively (**Figure 4.4**). Different shear failure modes were apparent for each group. Smooth PEEK failed at the glue layer interface, PEEK-SP failed within the porous network and within the solid region on the edges of some samples, and PEEK-BP failed in the empty bulk porous region behind the glue layer.

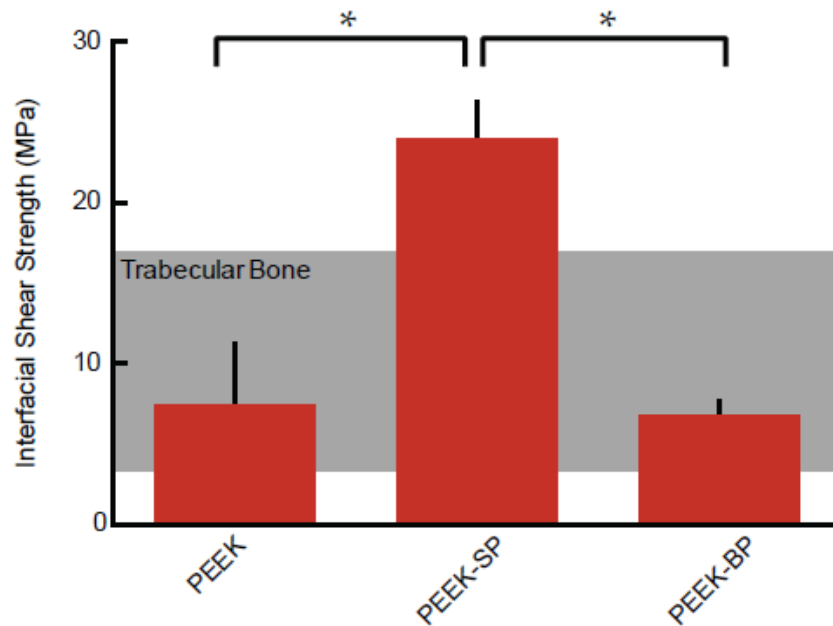


Figure 4.4. Interfacial shear strength of PEEK-SP compared to smooth PEEK and sintered PEEK-BP with the shear strength of trabecular bone shown in the shaded region [112]. Asterisks (*) indicate $p < 0.05$.

4.3.5. Implant Osseointegration

Three-dimensional μ CT reconstructions of PEEK explants at 6 and 12 weeks suggested bone formation within the PEEK-SP network (**Figure 4.5**). Bone ingrowth possessed cubic morphology similar to that of the pores, suggesting most available pore space was occupied by newly-formed bone. Cubic bone ingrowth regions were apparent at 4/6 porous interfaces and 0/6 smooth interfaces. Bone growth through the central cannula and along the outer surface of implants was present in 5/6 samples and originated from both proximal and distal ends (data not shown). Quantitative evaluation of bone ingrowth was prevented due to thresholding difficulties between PEEK and surrounding soft tissue.

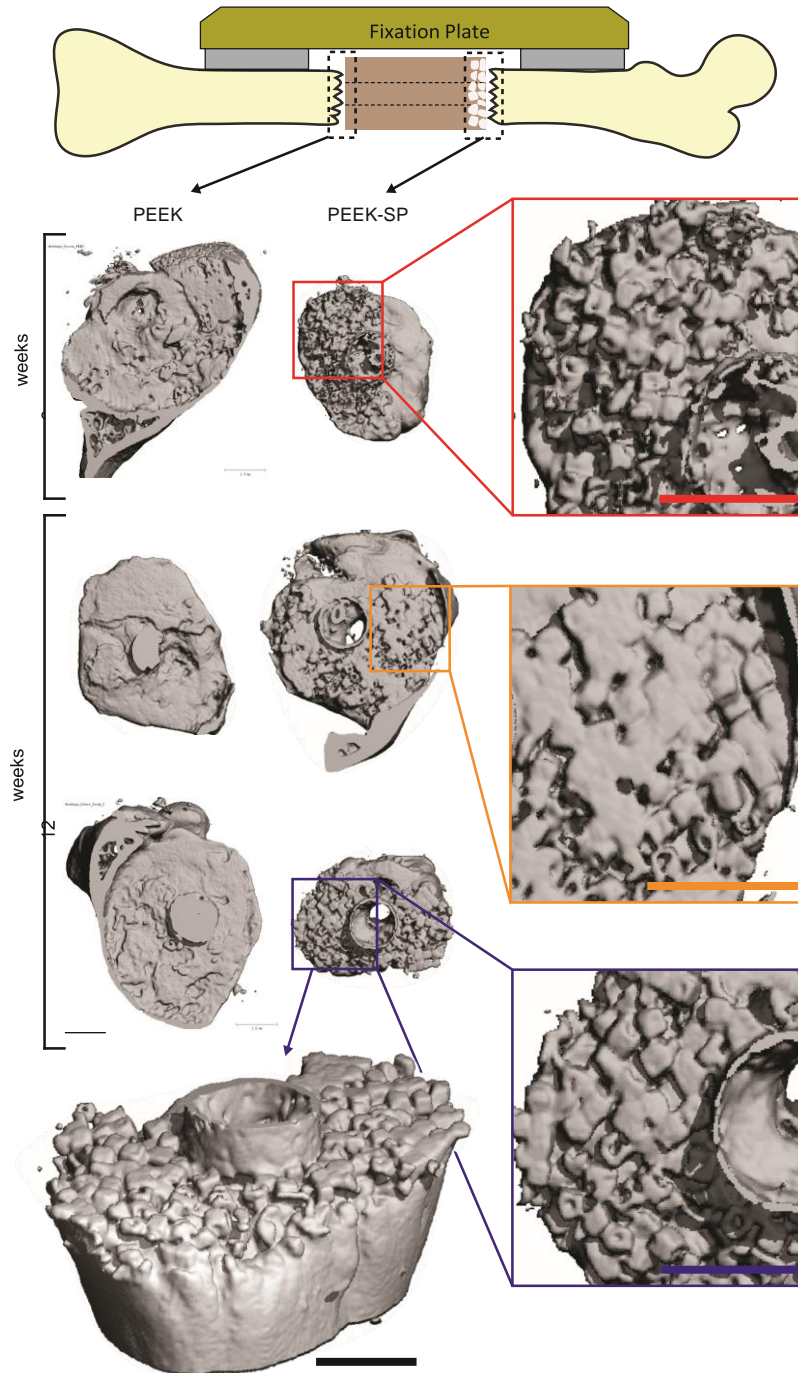


Figure 4.5. μ CT reconstructions of bone growth into PEEK-SP and adjacent to smooth PEEK surfaces (dashed boxes) at 6 and 12 weeks show the extent of bone ingrowth. Images are oriented with the lateral side on top. Insets show magnified views of ingrown bone. PEEK implants are not depicted due to thresholding difficulties of μ CT reconstructions. An angled view is presented to visualize the extent of bone intrusion into the porous surface layer. Note the cubic morphology of bone in the surface porous PEEK samples, suggesting complete growth into the cubic pores. Scale bars on μ CT images are 1 mm.

Histological evidence confirmed that the mineral seen within pores on μ CT reconstructions was cellularized bone (**Figure 4.6**). At both six and twelve weeks, substantial bone formation was evident within the pore layer, with bone formation seeming to increase between the two time points. Ingrown bone was closely apposed to the pore walls and exhibited a substantial reduction in fibrous tissue formation compared to the smooth PEEK faces.

Qualitative agreement between μ CT and histology was also confirmed by comparing bone ingrowth morphology at approximately the same cross sections using each technique. Mineral attenuation maps from μ CT represented histological findings well and provided further validation for using μ CT to detect bone ingrowth into the PEEK-SP pore layer (**Figure 4.6**).

4.4. Discussion

This study sought to create a surface porosity on PEEK to promote osseointegration while maintaining the structural integrity necessary for high load-bearing orthopaedic implants. The advantages of a surface porous polymeric implant have been previously discussed in the literature [15, 113, 114]. However, no surface porous PEEK structure has been shown to provide an adequate pore network for bone ingrowth while preserving the high strength of PEEK.

Characterization of our PEEK-SP surface layer revealed pore size, porosity and interconnectivity values that have been reported to allow for cell migration, nutrient transport, and vascularization that contribute to successful bone-implant integration [15, 17]. We also show that PEEK-SP preserved a high degree of PEEK's mechanical

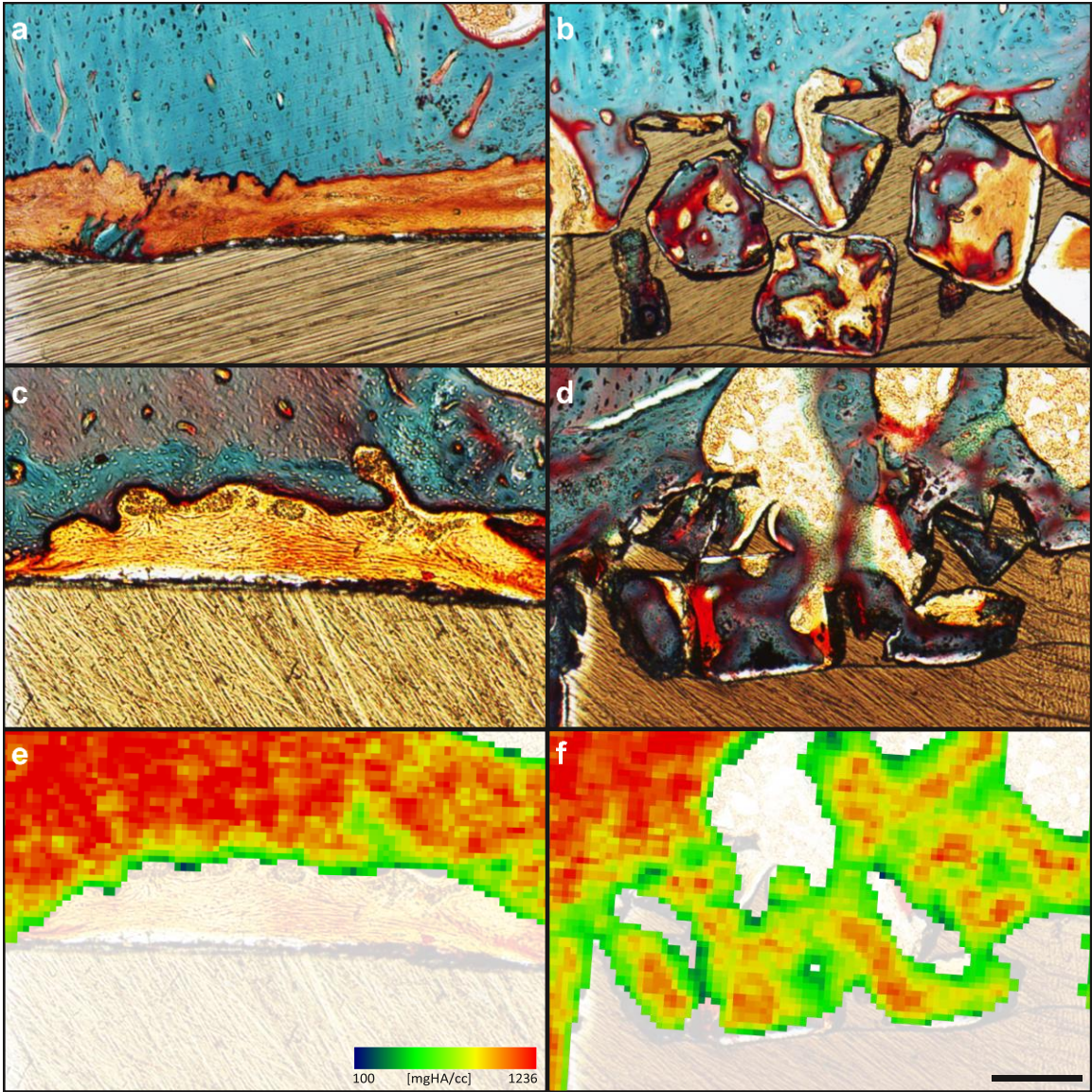


Figure 4.6. Bone ingrowth of PEEK-SP and smooth PEEK surfaces: (a,c) Representative histological images of fibrous tissue formation on smooth PEEK faces at six and twelve weeks, respectively. (b,d) Representative histological images of bone ingrowth within PEEK-SP faces at six and twelve weeks, respectively. Osteoid stained deep red; mineralized bone stained green; fibrous tissue stained light orange; and PEEK material is seen in brown. (e,f) Representative mineral attenuation maps from μ CT at approximately the same cross sections as (c,d). Blue represents lower mineral density and red indicates high mineral density. Scale bar is 200 μ m.

properties, retaining over 70% of the strength and modulus of solid PEEK when total cross-sectional area A_T is used in the stress calculation. Comparatively, typical bulk porous (BP) polymers reported in the literature retain only 15-36% strength and 11-39% modulus of the unprocessed polymer, depending on porous volume fraction (**Figure 4.7**) [8, 17, 107, 115-119].

Although the measured strength of PEEK-SP is decreased when using the total cross-sectional area A_T , the creation of a surface porosity does not significantly decrease the strength when calculated with the load-bearing area A_{LB} (**Figure 4.2**). The results indicate that the stress concentration effect of pores does not negatively impact material strength. The results also indicate that PEEK-SP retains its specific strength (strength/density), meaning the introduction of porosity using this processing method only spreads the material out rather than inherently weakening it. In addition, PEEK-SP possesses mechanical properties within the range of trabecular and cortical bone (**Figure 4.7**), a characteristic that has been suggested to improve *in vivo* functionality [17]. Mechanical properties can be tuned further by adjusting implant design parameters, such as decreasing layer thickness

Given the decrease in ductility in PEEK-SP and the inherent cyclic loading experienced by orthopaedic implants, it was important to evaluate the effect of the processing on the fatigue properties of PEEK. As shown in **Figure 4.3**, the inherent fatigue resistance of solid PEEK was highly maintained after creation of a porous surface layer. The data also demonstrate that the fatigue resistance of PEEK-SP outperformed other clinically used orthopaedic biomaterials. PMMA, a polymer used as bone cement, did not trend towards an endurance limit and possessed much lower fatigue strength than PEEK-

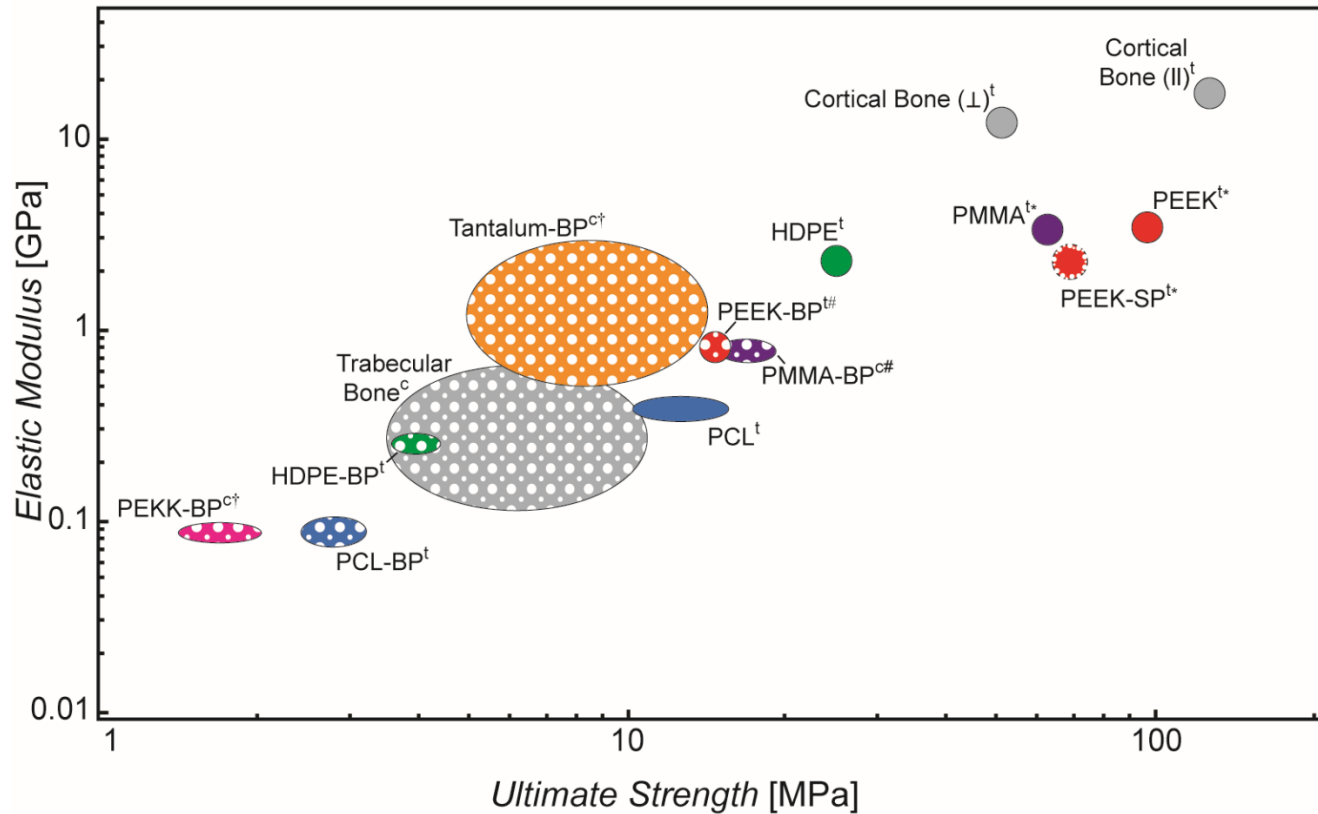


Figure 4.7. Ashby plot of elastic moduli and ultimate strengths for several orthopaedic biomaterials and bone that have been reported in the literature [8, 17, 107, 115-119]. Solid-filled ellipses represent fully dense materials and porous-filled ellipses represent porous materials. While cortical bone does possess low porosity, it is grouped with the fully dense materials for this comparison. Each material, with the exception of porous tantalum and polyether-ketone-ketone (PEKK), has both solid and porous properties included to illustrate the reduction in properties due to porosity. PEEK-SP is indicated by a porous layer outlining the solid-filled circle. Superscript ‘t’ refers to materials tested in tension and ‘c’ indicates compression. Daggers (†) indicate yield strengths where ultimate strength was not reported. Pound signs (#) indicate bending modulus when elastic modulus was not reported. Asterisks (*) indicate values tested by our group. Ellipse central location and size represents reported mean and plus or minus one standard deviation, respectively, where available.

SP in the high cycle regime. Similarly, porous tantalum, a bulk porous metallic implant material used clinically to facilitate osseointegration, has fatigue performance almost 43% lower than surface porous PEEK at similar cycle number [111].

Because large shear stresses are experienced near bone-implant interfaces *in vivo* that can lead to micro-motion and implant loosening [120], it was essential to probe the inherent interfacial shear strength of the porous surface layer. The significant increase in interfacial shear strength of PEEK-SP compared with solid (smooth) PEEK suggests that PEEK-SP will possess the advantage of a mechanical interlock and higher bonding strength between the implant biomaterial and the surrounding natural bone once ingrowth occurs, providing greater mechanical stability at this critical interface [121]. Furthermore, PEEK-SP provides this advantage over many current techniques explored in the literature. Physical surface treatments such as plasma modification have shown increased bioactivity of PEEK implants but may not provide sufficient space for bony ingrowth and implant-bone fixation [14, 104]. In addition, PEEK implant coatings such as titanium and hydroxyapatite have demonstrated improved cellular response, [11, 122] but can be subject to delamination and decreased fatigue life [53]. Finally, sulfonation has been used to chemically modify the surface of PEEK and introduce a nanoporous surface network to improve osseointegration [114]. However, with single-micron pores that are well below the typical range for bone formation, sulfonated surface porous PEEK may not allow for the bony ingrowth that contributes to a strong mechanical interlock between the implant and bone.

The process of creating a surface porosity on PEEK implants introduces a random, topographically varied surface that may contribute to enhanced osseointegration. Such a disordered topography has been shown to improve the osteogenic response at nano- to micron-size scales [49, 58, 123, 124]. At a larger scale, porosity has also shown increased osteogenesis compared to solid or topographically smooth surfaces [17]. Together, the literature suggests that the random, topographically varied PEEK-SP surface may enhance the cellular response, leading to more stable fixation than PEEK that is smoother at the cellular level.

Though PEEK-SP and PEEK-BP both offer the potential for bone ingrowth into the porous network, the significantly lower shear strength of PEEK-BP may limit its clinical use in rigorous loading environments. The three-fold higher shear strength of PEEK-SP could be attributed to the porous surface layer being extruded from the bulk material instead of being created with the additive or sintering techniques currently used to create PEEK-BP. Extrusion of PEEK-SP from the bulk material seamlessly integrates solid and porous regions at the molecular level and maintains the high molecular weight necessary for high strength (**Table 4.1**). Notably, the surface porous layer has higher interfacial shear strength than trabecular bone [112] (**Figure 4.4**), which implies that failure will originate from bone itself and not the solid-porous interface even when high quality bone has fully integrated.

Preliminary *in vivo* results provide further evidence of PEEK-SP's capacity to promote bony ingrowth needed for strong implant fixation (**Figures 4.5, 4.6**). Substantial bone formation within the pore layer was confirmed via μ CT and histology at six and twelve weeks post-surgery. These initial *in vivo* results compare favorably with previously

reported porous networks with similar architectures to PEEK-SP. For example, a porous PEEK-HA composite has been shown to facilitate bone ingrowth with close apposition to the pore walls, similar to PEEK-SP [6]. However, even the nonporous form of current PEEK-HA composites can lack the strength, ductility and fatigue resistance of PEEK-SP.

A direct comparison of PEEK-SP to porous titanium can be found in a study that used a nearly identical segmental defect model in the rat [93]. This study reports a time course of bone ingrowth close to that of PEEK-SP and also describes similar histological findings. Both studies found substantial bone formation in the central cannula and around the outside of the implants, illustrating an attempt by bone to bridge the defect. Both studies also found close bone apposition to the pore walls (or struts) with the presence of some fibrous tissue in regions where bone was absent.

Though some fibrous tissue formation was apparent within the PEEK-SP pore network, the degree to which it formed was reduced compared to the characteristic fibrous encapsulation of smooth PEEK seen in **Figure 4.6** and in previous studies [125, 126]. Many regions of PEEK-SP possessed pores that were completely filled with cellularized bone and no fibrous layer was observed between the bone and implant. Such reduced fibrous encapsulation combined with potentially faster bone ingrowth could increase implant stability and limit micromotion that can lead to increased inflammation and eventual implant loosening and failure [49, 127, 128].

The clinical potential of PEEK-SP is further illustrated with the clearance of this technology on a suture anchor implant and spinal interbody fusion device through the Food and Drug Administration (FDA) in the United States (marketed as Scoria™). Despite these promising preliminary findings, further work is necessary to fundamentally understand

what causes bone formation within the PEEK-SP pore layer and the quantitative mechanics behind the osseointegration of PEEK-SP [129].

4.5. Conclusion

A process for selectively introducing surface porosity on PEEK that retains a substantial fraction of the solid polymer's mechanical properties has been investigated. This method provides many advantages over sintered bulk porous polymers that rely on superficial bonding between polymer particles, which severely compromises mechanical properties. The creation of a surface porosity produced samples with high tensile strength, fatigue resistance and interfacial shear strength while simultaneously providing available porosity for bone ingrowth. Preliminary *in vivo* results provided evidence of bone ingrowth into the pore network, which could lead to enhanced implant stabilization. Though the cubic morphology of ingrown bone produced by this technique provides convincing preliminary evidence of improved osseointegration, the functionality of bone ingrowth remains to be determined in future studies.

CHAPTER 5

EFFECTS OF PORE SIZE ON THE MECHANICAL PROPERTIES AND CELLULAR RESPONSE OF SURFACE POROUS PEEK

5.1. Introduction

Polyether-ether-ketone (PEEK) is a polymer widely used in orthopaedic and spinal applications such as soft tissue repair and spinal fusion devices due to its high strength, fatigue resistance, radiolucency, and favorable biocompatibility in osseous environments [1, 36, 130-132]. However, due in part to PEEK's relatively inert and hydrophobic surface, recent evidence has demonstrated that smooth PEEK can exhibit poor osseointegration [1, 70] and fibrous capsule formation around the implant [47, 48]. Lack of bone-implant contact can induce micromotion and inflammation that leads to fibrous layer thickening, osteolysis, and implant loosening [49-53]. Previous studies [6, 11, 13, 14, 63, 104] have shown that surface modifications such as plasma treatments, coatings, and composites can improve PEEK implant integration, yet many suffer practical limitations such as delamination, instability, and mechanical property trade-offs.

The addition of porosity is a common modification to improve implant osseointegration by facilitating bone ingrowth and vascularization [133]. The importance of porosity for bone regeneration has been reviewed [17], and methods to create porous PEEK have been reported [107, 131, 132, 134-136]. However, it's still unclear which aspects of the pore architecture (such as, pore size, porosity, and pore layer thickness) control the mechanical and biological properties of porous PEEK implants.

Previously, **Chapter 4** described a surface porous PEEK (PEEK-SP) structure with high tensile strength, fatigue resistance, interfacial shear strength, and improved osseointegration compared to smooth PEEK [134]. Though the pore size investigated (200-312 μm) was within the commonly accepted range for porous orthopaedic implants [17], additional work is needed to investigate whether the pore microstructure could be reliably controlled to yield other pore sizes and the subsequent effect of pore size on both the mechanical properties and biological responses to PEEK-SP.

The ability to spatially control pore size will also be explored to create biomimetic implants. Biologically inspired design is becoming an increasingly important and useful principle in the design and fabrication of engineered materials as it can be used to improve the functionality and outcomes of implants and tissue engineering scaffolds [137]. Specifically, the study of functionally graded materials has received much attention recently [138-140]. Functionally graded materials are characterized by gradual changes in composition, crystallinity, and/or structure from one interface or region to another [141]. In particular, a structure change across a material provides unique functionality and performance for biomedical applications as both the mechanical behavior and interactions with cells living in the surrounding tissue can be tailored and optimized.

For example, the structure of bone changes from a dense, stiff external structure (the cortical bone) to a porous internal one (the cancellous bone), demonstrating that functional gradation has been utilized by biological adaptation [138]. Implants designed with functionally graded porosity and/or stiffness can be used to mimic the graded pore structure similar to the bimodal structure of cortical and cancellous bone to simulate natural bone tissue morphology [142-144]. It has been recommended that scaffolds and implants

incorporate anisotropic pore architecture to accommodate the different types of cells and ECM distribution at the interface [145]. Studies have suggested that the pore size and substrate surface influence cell morphology and phenotypic expression while porosity influences cell proliferation. It has been shown that pore sizes between 70-120 μm promote chondrocyte ingrowth [146], and between 40-150 μm fibroblast binding [147]. Pores between 100-500 μm are appropriate for osteoconduction and bone regeneration with increased vascular invasion to provide sufficient oxygen and nutrient delivery [17, 31, 148]. The optimal pore size and distribution of pore sizes depends on porosity, material used, and specific cells and tissues [17, 149].

Furthermore, the overall volume of porosity and its spatial distribution throughout the implant should be considered due to the inverse relationship between porosity and strength of porous structures [150]. For example, limiting porosity to just a thin surface layer could facilitate adequate ingrowth for stable implant fixation while preserving the solid core for load bearing.

Therefore, this chapter seeks to answer the following three questions: (1) Can PEEK-SP microstructure be reliably controlled? (2) What is the effect of pore size on the mechanical properties of PEEK-SP? (3) Do surface porosity and pore size influence the cellular response to PEEK?

5.2. Materials and Methods

5.2.1. Materials

PEEK-SP was created by extruding PEEK through the open spacing of sodium chloride crystals under heat and pressure as described in **Chapter 3**. To control for pore size, sodium chloride was sieved into ranges of 200-312 μm , 312-425 μm , and 425-508 μm

using #70, #50, #40, and #35 U.S. mesh sieves. Samples processed using each size range are referenced as PEEK-SP-250, PEEK-SP-350, and PEEK-SP-450, respectively. Characterization of the pore microstructure was performed as outlined in **Chapter 3**. Injection molded PEEK samples (PEEK-IM) were used as nonporous controls for mechanical testing. For cell studies, smooth nonporous PEEK samples were manufactured with a machined surface finish. Medical grade Ti6Al4V ELI was purchased from Vulcanium (Northbrook, IL) and the surface was fine grit blasted (GB-13 blast media) and anodized according to AMS 2488D Type II by Danco (Arcadia, CA). Nonporous, machined smooth PEEK, PEEK-SP pore walls and Ti6Al4V surfaces possessed a surface roughness (S_a) of $0.59 \pm 0.12 \mu\text{m}$, $0.48 \pm 0.10 \mu\text{m}$ and $0.55 \pm 0.02 \mu\text{m}$, respectively, determined by laser confocal microscopy using a 50x/0.5 mm objective, 50 nm step size and $\lambda_c = 20 \mu\text{m}$ (LEXT OLS4000). S_a values were not statistically different between groups ($p = 0.28$, 1-way ANOVA).

5.2.2. Methods

All samples used in mechanical testing were processed using the oven method as described in **Chapter 3**. In addition, the bimodal pore distribution sample, the hydroxyapatite/PEEK composite samples, and the *in vitro* were made using the oven. The samples demonstrating the ability to manufacture tunable pore layer thicknesses and the graded pore size sample were produced using the hot plate method.

Tensile tests, fatigue tests, interfacial shear tests, and *in vitro* examination were carried out according to the methods outlined in **Chapter 3**.

5.2.3. Statistical Analysis

Results of mechanical tests were analyzed using a one-way ANOVA and Tukey post-hoc analysis (95% confidence interval). In vitro assays were analyzed using a one-way ANOVA for EdU assays and a two-way ANOVA for all other assays. Bonferroni post-tests were used to compare all in vitro groups. All data are expressed as mean \pm standard deviation (S.D.).

5.3. Results

5.3.1. Pore Layer Characterization

Using μ CT analysis, we found that pore morphology could be reliably controlled by varying the sodium chloride crystal size with the pores conforming to the porogen's cubic shape (**Figure 5.1, 5.2**). The data demonstrate that salt crystal size can be used to reliably control the pore size of PEEK-SP (SP-250 = $284 \pm 35 \mu\text{m}$, SP-350 = $341 \pm 49 \mu\text{m}$, SP-450 = $416 \pm 54 \mu\text{m}$) ($p < 0.001$). Porosity was slightly affected with SP-250 having marginally higher porosity ($68 \pm 3 \%$) compared to SP-350 ($61 \pm 3 \%$) and SP-450 ($62 \pm 4 \%$) ($p < 0.001$). All three groups had high levels ($> 99\%$) of pore interconnectivity (**Table 5.1**). As expected, strut morphology parameters (spacing and thickness) were strongly influenced by crystal size, but were again highly consistent within the three groups, suggesting a high level of manufacturing reproducibility and control.

The process also allowed for control in creating functionally graded porous architectures. **Figure 5.3** shows a PEEK-SP structure with graded porosity where the pore size ranges from $\sim 500\mu\text{m}$ at the solid-pore layer interface to $\sim 200\mu\text{m}$ at the face of the implant and **Figure 5.4** shows the pore size as a function of pore layer thickness. **Figure 5.5** demonstrates the ability to create a bimodal pore size by using two different ranges of

salt crystal sizes and **Figure 5.6** shows μ CT reconstructions of various pore layer thicknesses. Finally, **Figure 5.7** shows a proof-of-concept PEEK-SP HA composite.

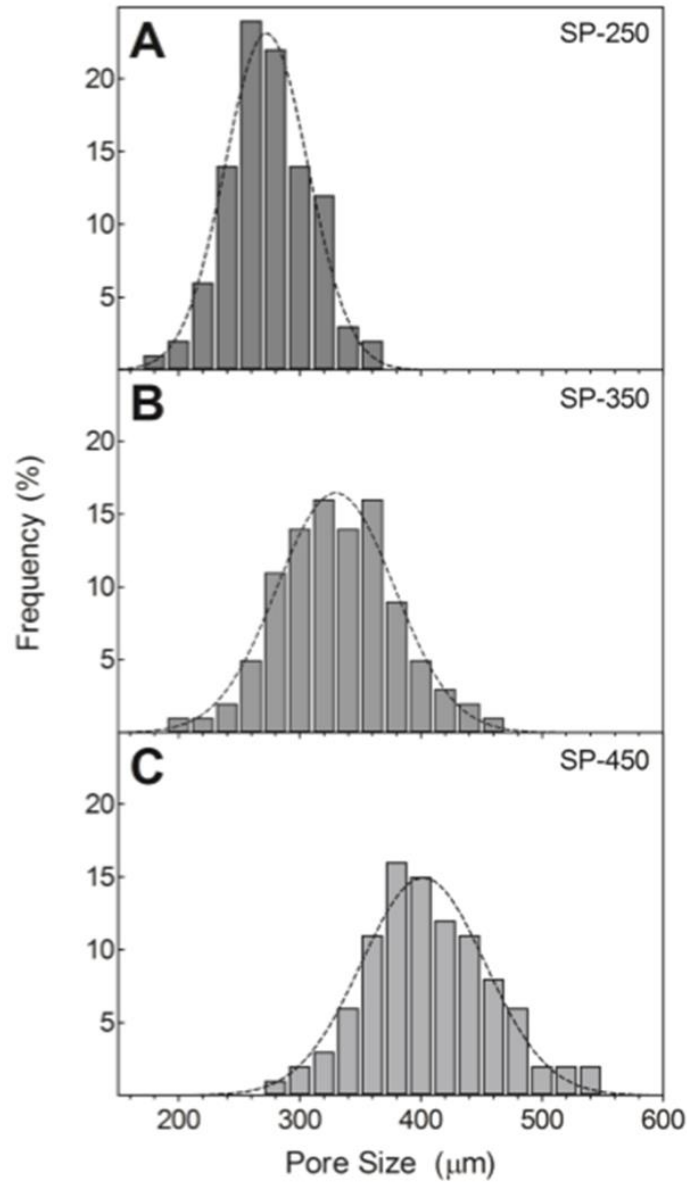


Figure 5.1. Pore size histograms as characterized by μ CT for (A) PEEK-SP-250, (B) -SP-350 and (C) -SP-450. Dotted lines represent Gaussian fits of each data set.

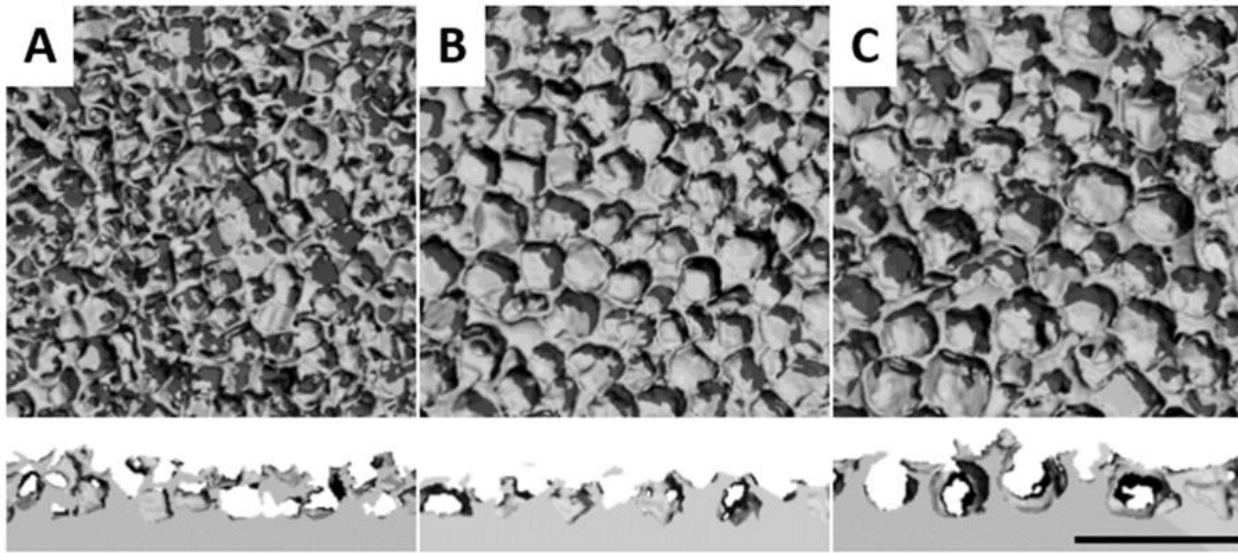


Figure 5.2. Representative μ CT reconstructions of the surface and cross section of PEEK-SP. PEEK-SP-250 is shown on the left, PEEK-SP-350 in the middle, and PEEK-SP-450 on the right. Scale bar is 1mm.

Table 5.1. Pore size, strut spacing, strut thickness, porosity, interconnectivity, and thickness values of the surface porous layer of PEEK-SP of various pore sizes. * $p < 0.01$ vs SP-250, ^ $p < 0.05$ versus SP-350 (1-way ANOVA, Tukey). Mean \pm S.D.

	Pore Size	Strut Spacing	Strut Thickness	Porosity	Interconnectivity	Layer Thickness
	(μm)	(μm)	(μm)	(%)	(%)	(μm)
PEEK-SP-250	284 \pm 35	169 \pm 3	73 \pm 8	69 \pm 3	99.9 \pm 0.04	391 \pm 79
PEEK-SP-350	341 \pm 49 *	208 \pm 5 *	104 \pm 9 *	61 \pm 3 *	99.8 \pm 0.17	303 \pm 29 *
PEEK-SP-450	416 \pm 54 * ^	248 \pm 1 * ^	119 \pm 14 * ^	62 \pm 4 *	99.8 \pm 0.25	342 \pm 38

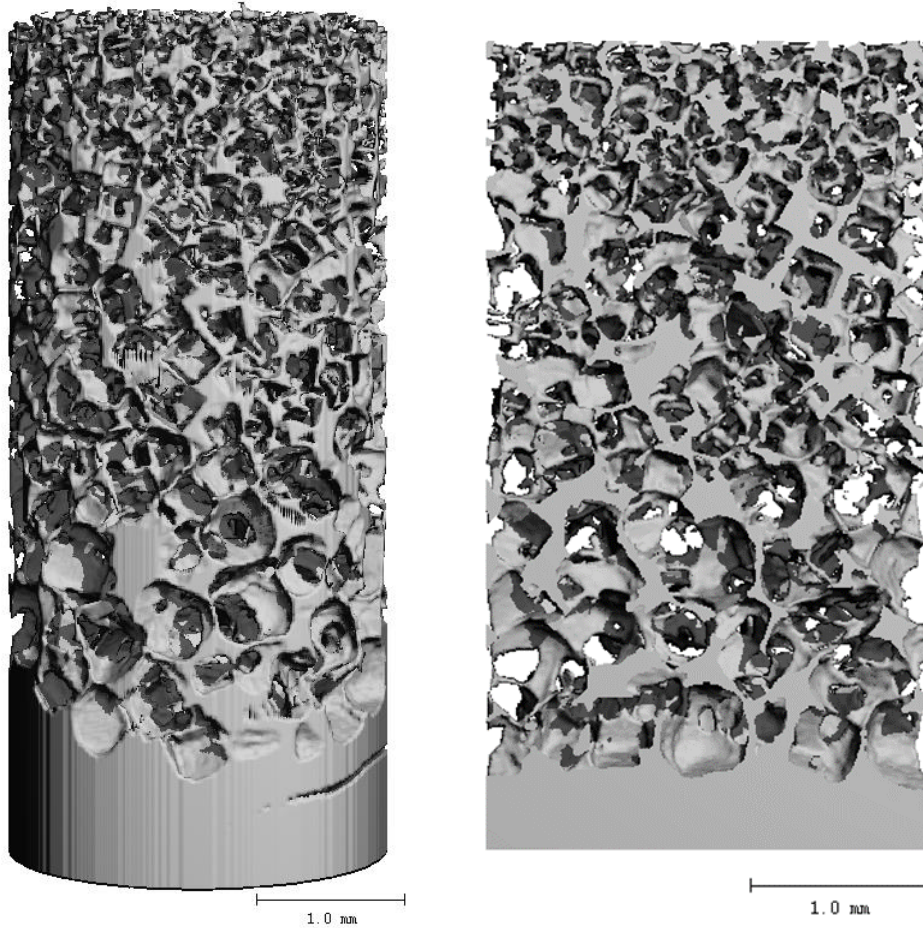


Figure 5.3. Functionally graded porosity with the pore size decreasing from $\sim 500\mu\text{m}$ to $\sim 200\mu\text{m}$ over the 5mm pore layer thickness.

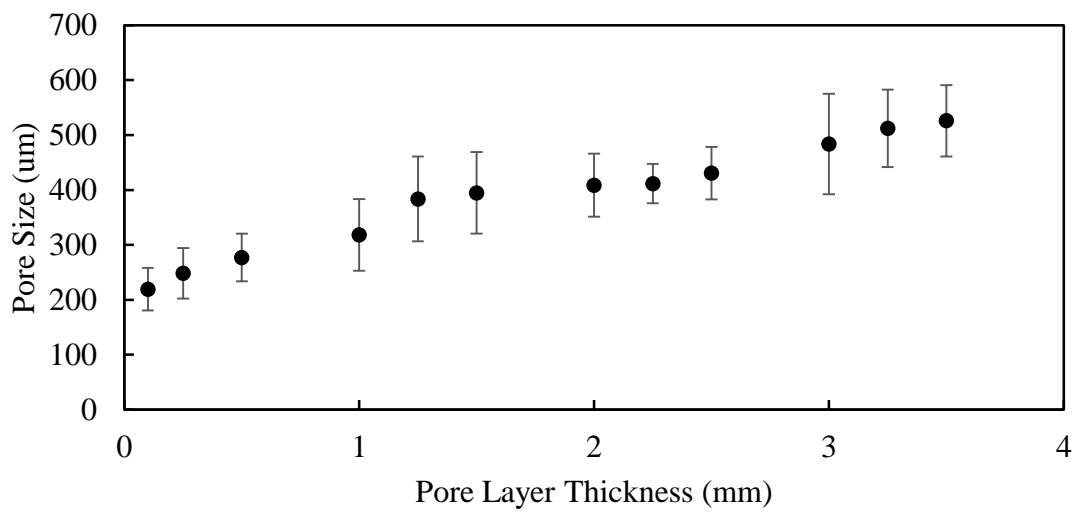


Figure 5.4. Pore size as a function of layer thickness in the functionally graded sample.

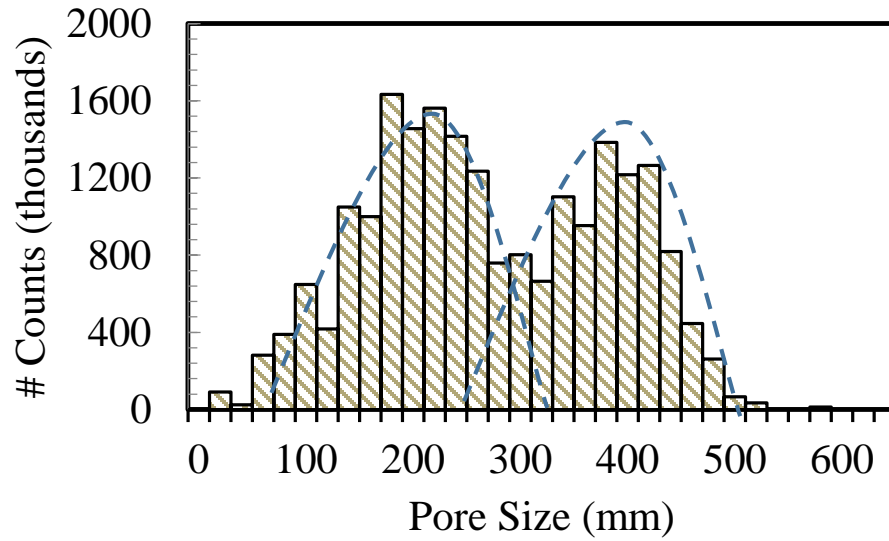


Figure 5.5. Bimodal pore size distribution for sample processed with two different salt crystal sizes.

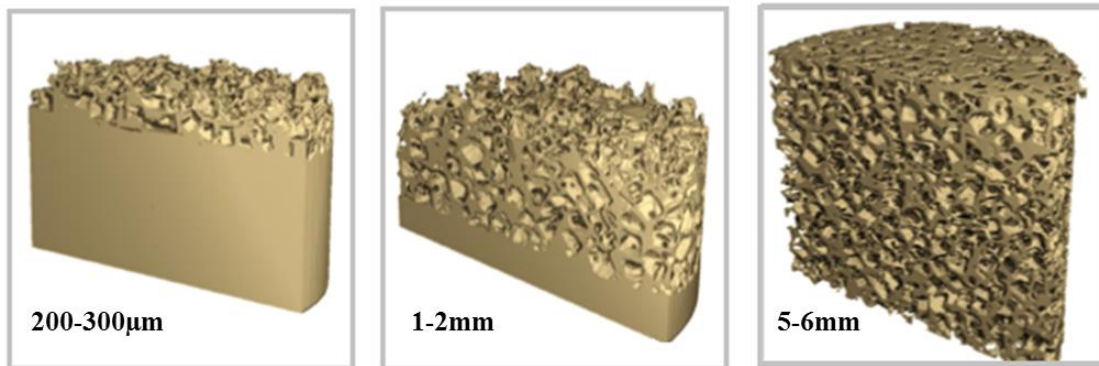


Figure 5.6. μ CT reconstructions of PEEK-SP showing variations in pore layer thickness.

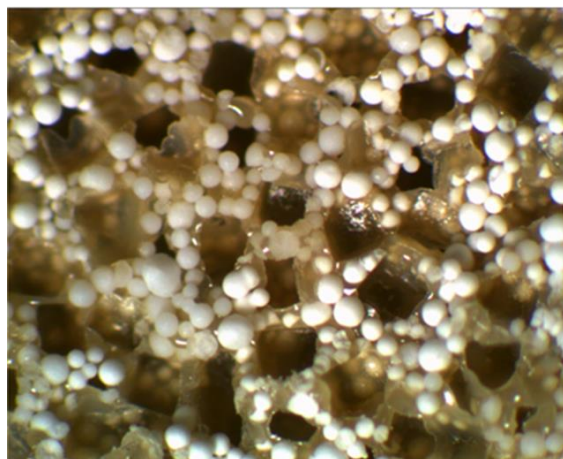


Figure 5.7. Optical microscope image showing a PEEK-SP HA composite.

5.3.2. Mechanical Properties

Representative tensile stress-strain curves of PEEK-IM and PEEK-SP are shown in **Figure 5.8** and average values are summarized in **Table 5.2**. Compared to PEEK-IM, PEEK-SP had no significant effect on tensile strength when normalized to A_{LB} for PEEK SP-250 and PEEK SP-450 but there was a small decrease for the PEEK-SP-350 group ($p < 0.05$). All pore sizes showed a decrease in ductility as indicated by a significant decrease in failure strain ($p < 0.01$). No difference was found in the modulus between PEEK-SP samples and PEEK-IM when using A_{LB} . Fatigue tests showed that surface porosity decreased the fatigue strength of PEEK, with the difference more pronounced at higher cycles (**Figure 5.9**). Furthermore, PEEK-SP-450 appears to have a lower fatigue strength than the 250 samples. The fatigue life at one million cycles was 81.7 MPa for PEEK-IM, 60.0 MPa (A_{LB}) and 45.3 MPa (A_T) for PEEK-SP-250, and 53.4 MPa (A_{LB}) and 38.0 MPa (A_T) for PEEK-SP-450. The average interfacial shear strength of PEEK-IM, PEEK-SP-250, PEEK-SP-350, and PEEK-SP-450 was 7.52 ± 3.64 , 23.96 ± 2.26 , 21.41 ± 4.32 , and 22.41 ± 3.64 , respectively (**Figure 5.10**). Different shear failure modes were apparent for smooth PEEK and PEEK-SP. Smooth PEEK failed at the glue layer interface and the PEEK-SP samples failed within the porous network and within the solid region on the edges of some samples. No significant difference was found between PEEK-SP samples of different pore sizes, but all PEEK-SP samples had significantly higher shear strength than the high strength adhesive alone on smooth PEEK (**Figure 5.10**, $p < 0.001$).

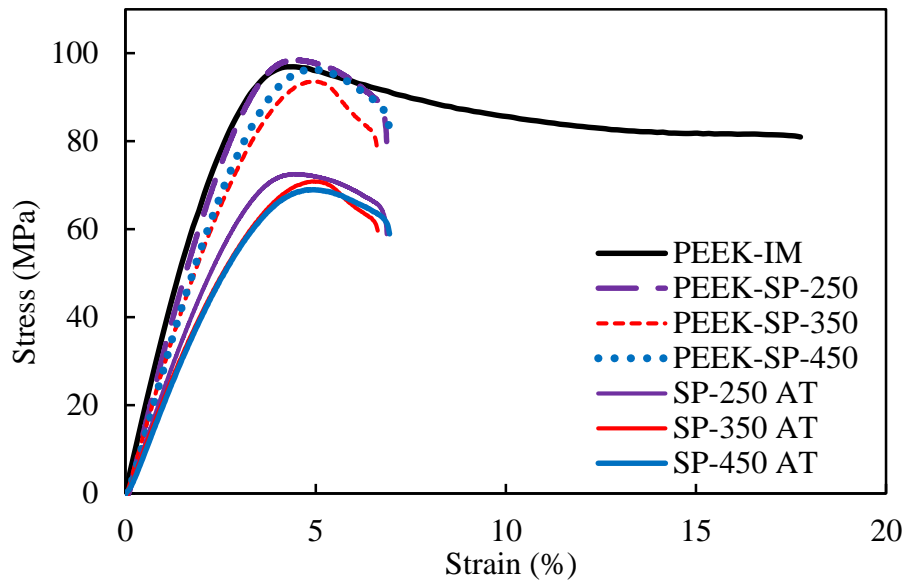


Figure 5.8. Representative stress-strain curves of PEEK-IM and PEEK-SP.

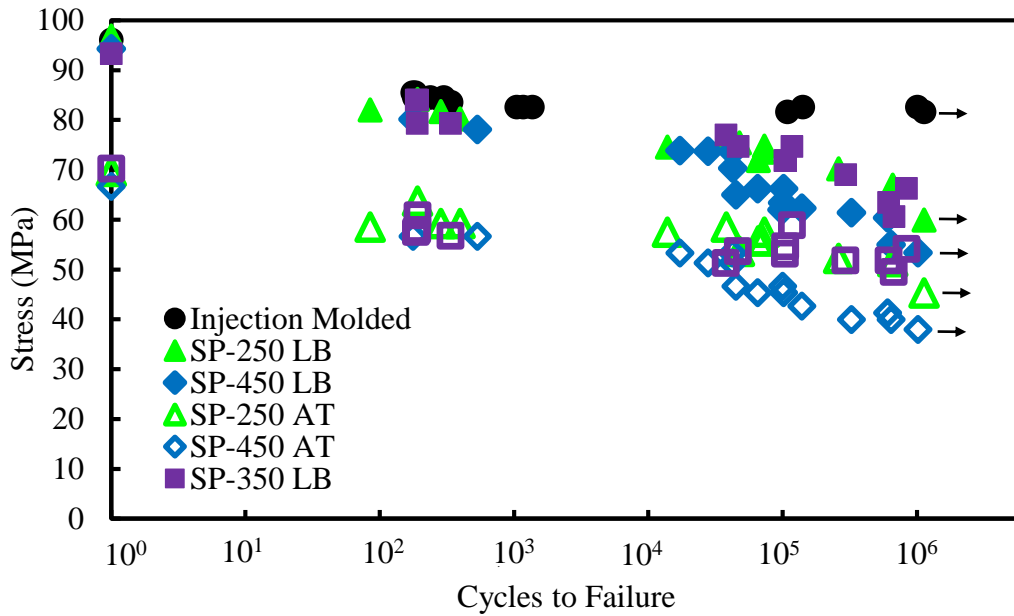


Figure 5.9. S–N curves comparing the fatigue behavior of PEEK-IM and PEEK-SP of different pore sizes. Arrows denote tests that were halted after reaching 10^6 cycles which was defined as the runout stress.

Table 5.2. Measured load-bearing tensile strength, total area tensile strength, failure strain, load-bearing tensile modulus, and total area tensile modulus of PEEK-IM and PEEK-SP. The load-bearing area, A_{LB} , includes only the cross-sectional area of the polymer materials, ignoring void area. The total area, A_T , assumes void area contributes to load bearing area and is thus the measured sample dimensions. * $p < 0.01$ versus IM, ^ $p < 0.05$ versus SP-250 (1-way ANOVA, Tukey). Mean \pm S.E.

	Tensile Strength, A_{LB} (MPa)	Tensile Strength, A_T (MPa)	Failure Strain (%)	Modulus, A_{LB} (GPa)	Modulus, A_T (GPa)
PEEK-IM	97.7 \pm 0.4	97.7 \pm 0.4	20.2 \pm 1.1	3.3 \pm 0.1	3.3 \pm 0.1
PEEK-SP-250	96.1 \pm 1.1	71.1 \pm 0.9 *	7.8 \pm 0.9 *	3.4 \pm 0.1	2.5 \pm 0.1 *
PEEK-SP-350	93.4 \pm 0.7 *	70.3 \pm 1.5 *	7.0 \pm 0.4 *	3.3 \pm 0.1	2.5 \pm 0.1 *
PEEK-SP-450	94.5 \pm 0.6	67.0 \pm 0.7 * ^	8.1 \pm 0.7 *	3.2 \pm 0.1	2.3 \pm 0.1 *

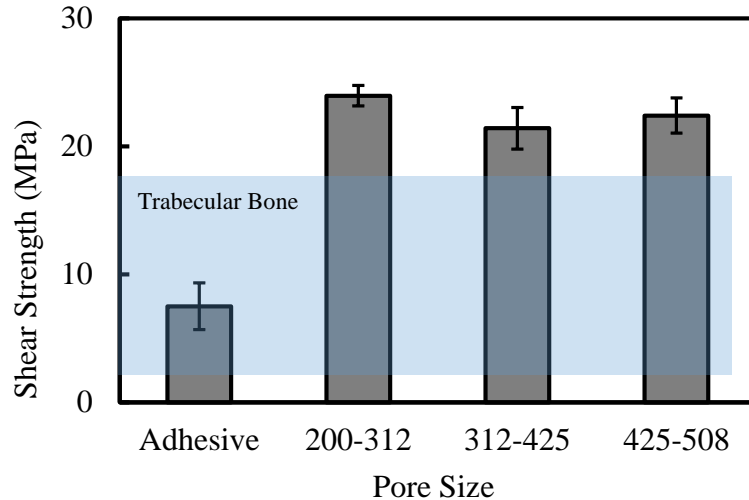


Figure 5.10. Interfacial shear strength of PEEK-SP compared to the strength of the PEEK-IM contacting adhesive, with the shear strength of trabecular bone shown in the shaded region [112, 151]. $\forall p < 0.001$ versus all SP groups (1-way ANOVA, Tukey). Mean \pm S.E.

5.3.3. *In Vitro* Proliferation and Osteogenic Differentiation

Over all, cells cultured on PEEK-SP surfaces (regardless of pore size) exhibited a more differentiated phenotype than those cultured on PEEK-IM. All PEEK-SP groups had greater EdU DNA incorporation, which is indicative of increased cell proliferation, than smooth nonporous PEEK, Ti6Al4V, and TCPS surfaces for both hOBs and hMSCs cultures ($p < 0.001$, except smooth vs. SP-250 (hOB), $p = 0.010$ and smooth vs. SP-350 (hMSC), $p = 0.005$) (**Figure 5.11**). However, there were no differences found in EdU incorporation between pore sizes ($p > 0.999$, except SP-250 vs. SP-350 (hOB), $p = 0.259$). Likewise, all PEEK-SP groups had similar calcium levels ($p > 0.999$) that were much greater than smooth PEEK ($p < 0.001$), Ti6Al4V ($p < 0.001$) and TCPS ($p < 0.001$) in osteogenic conditions (**Figure 5.12A**). As expected, an overall reduction in calcium was seen on acellular controls and was further reduced in HEK groups, approaching levels detected in MC3T3 groups under growth (non-osteogenic) media conditions. No differences in

calcium were found between groups for MC3T3 cultures in growth media or HEK cultures ($p > 0.999$). Under osteogenic conditions, smooth PEEK supported fewer cells than Ti6Al4V ($p < 0.05$) and TCPS ($p = 0.011$) (**Figure 5.12B**). In growth media, TCPS and Ti6Al4V surfaces supported more cells than all PEEK and PEEK-SP surfaces ($p < 0.001$, except Ti6Al4V vs. SP-450, $p = 0.0013$). ALP activity of MC3T3 cells in osteogenic conditions at Day 14 was greater on TCPS compared to all other surfaces ($p < 0.001$, except smooth PEEK, $p = 0.002$) and was greater for smooth PEEK and Ti6Al4V compared to all PEEK-SP groups (smooth vs. SP-250, $p < 0.001$; smooth vs. SP-350, $p = 0.008$; smooth vs. SP-450, $p = 0.002$; Ti6Al4V vs. SP-250, $p = 0.14$; Ti6Al4V vs. SP-350, $p = 0.002$) (**Figure 5.12C**). No differences in ALP activity were found under growth conditions. VEGF secretion of MC3T3 cells in growth media was greater on SP-250 compared to Ti6Al4V and TCPS, and greater on SP-350 compared to TCPS ($p < 0.05$). Likewise, VEGF secretion in osteogenic media was greater on all PEEK-SP groups compared to all smooth groups except SP-450 versus Ti6Al4V ($p < 0.01$ versus smooth PEEK and TCPS, $p < 0.05$ versus Ti6Al4V) (**Figure 5.13**).

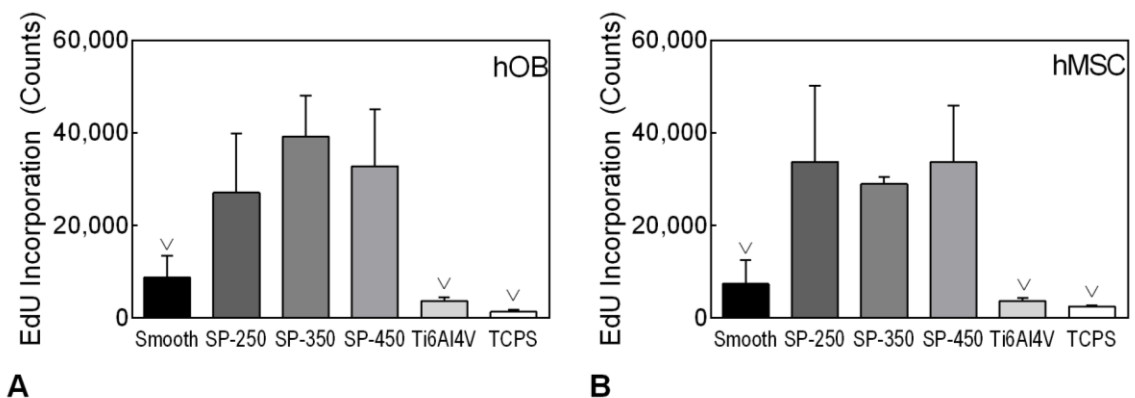


Figure 5.11. (A) hOB and (B) hMSC proliferation measured by DNA incorporation of EdU 48 hours after seeding on smooth PEEK, PEEK-SP of various pore sizes, Ti6Al4V and TCPS. $\nabla p < 0.01$ versus all SP groups (1-way ANOVA, Tukey). Mean \pm S.D.

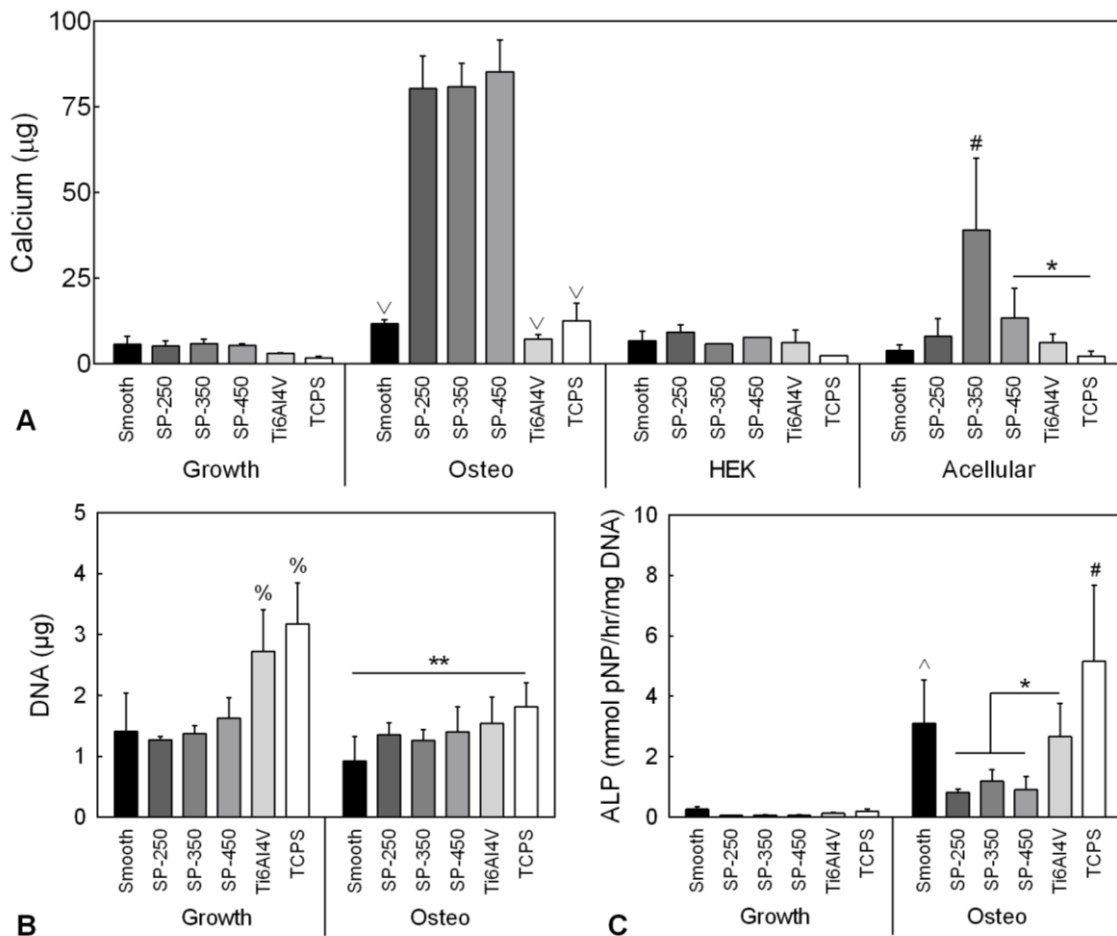


Figure 5.12. (A) MC3T3 mediated calcium deposition on PEEK-SP groups compared to smooth PEEK, Ti6Al4V and TCPS in growth media and osteogenic media. HEK cell and acellular cultures were used to determine the extent of noncell mediated mineralization. Osteo: \vee $p < 0.001$ versus all SP groups; Acellular: # $p < 0.001$ versus all groups, * $p < 0.05$ (2-way ANOVA, Tukey). (B) DNA content of parallel cultures on the same groups as in (A). Growth: % $p < 0.001$ versus all PEEK groups; Osteo: ** $p < 0.01$ (2-way ANOVA, Tukey) (C) ALP activity of same-well cultures as (B). Osteo: ^ $p < 0.05$ versus all SP groups, # $p < 0.01$ versus all groups, * $p < 0.05$. (2-way ANOVA, Tukey). Mean \pm S.D.

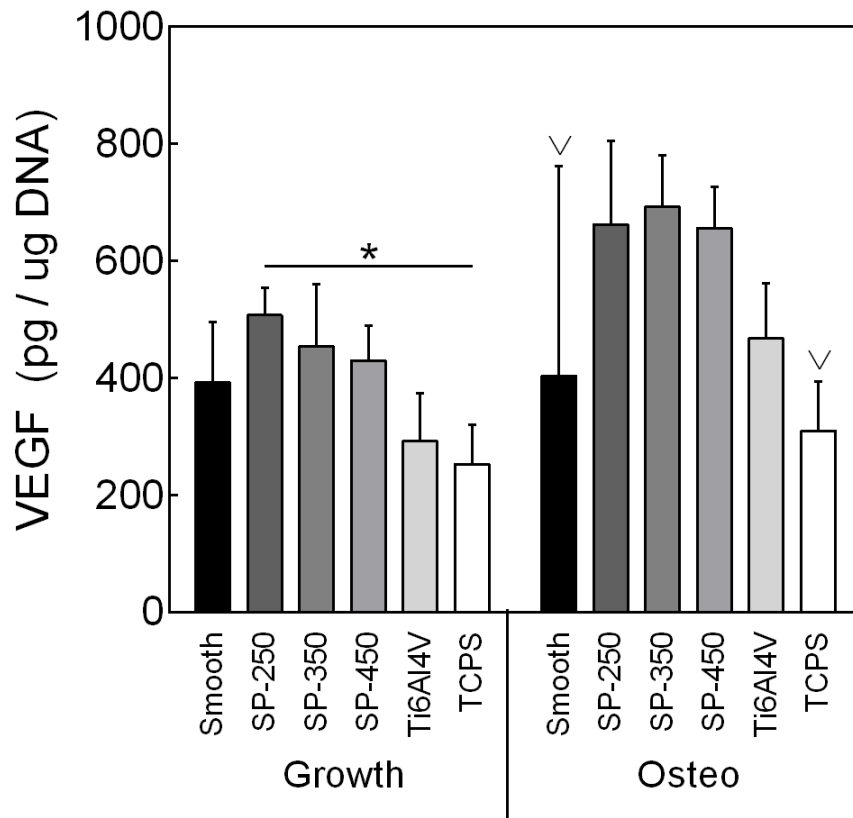


Figure 5.13. VEGF secretion from MC3T3-E1 cells on PEEK-SP groups compared to machined smooth PEEK, Ti6Al4V and TCPS in growth media and osteogenic media. ∇ $p < 0.05$ versus all SP groups, * $p < 0.05$ (2-way ANOVA, Tukey). Mean \pm S.D.

5.4. Discussion

Interest in improving PEEK's osseointegration has accelerated in recent years after numerous reports have described its inability in smooth form to facilitate bone apposition [1, 47, 48, 70, 152]. Reasons why this interest persists (as opposed to abandoning PEEK altogether) are often attributed to the other qualities of PEEK that make it favorable in orthopaedic and spinal applications, mainly its radiolucency, MRI compatibility, high strength, and fatigue resistance. In addition, PEEK's elastic modulus is between that of cortical and trabecular human bone [17, 112] which may result in a lower risk of stress

shielding and subsidence in applications such as spinal fusion when compared to other implant materials of the same geometry. It was previously shown that a surface porous PEEK implant facilitated osseointegration while preserving enough of PEEK's mechanical properties to be considered as a material for load-bearing orthopaedic implants [134]. Here we further investigated the PEEK-SP pore structure to compare the mechanical and biological performance of PEEK-SP with varied pore sizes.

Our study has a few limitations. First, percent porosity was not systematically studied and the range of pore sizes tested is rather small and only represents a two-fold difference from the smallest to largest pores. However, the range of pore sizes that we tested are expected to cover the range that is clinically-relevant [17]. Second, many applications can place implants under complex static or cyclic loading environments, such as compression, torsion and, bending (or combinations thereof), that were not tested here. Surface flaws will have the most detrimental effect on the bulk properties in tension, thus, we believe that the data presented here represent a worst case scenario; compression and abrasion testing are studied in **Chapter 7**. Additionally, all mechanical tests were performed in air at room temperature but are not likely to deviate from those performed in a more physiologic environment. Third, we have not exclusively singled out pore size as a factor since other parameters also change with pore size (such as layer thickness) (**Table 1**).

We were able to reliably control pore size by selecting the size of salt crystal used as porogen. Reports investigating optimum pore sizes for various tissues generally recommend a pore size of 200-500 μm for bone [72, 153]. Smaller pores may prevent cell infiltration or lead to insufficient vascularization and nutrient transport in vivo [17, 148].

Therefore, salt crystal sizes used in this study (200-508 μm) were chosen to promote bone ingrowth and create a pore structure favorable for osseointegration. Microstructural characterization also showed that strut morphology parameters (spacing and thickness) were strongly influenced by crystal size, but were again highly consistent within the three groups, suggesting a high level of manufacturing reproducibility and control.

Spatial control over pore size and creation of bimodal pore distributions was also demonstrated (**Figure 5.3-5.5**). Implants designed with gradients in porosity and pore sizes can allow on one side of the implant high vascularization and direct osteogenesis, while promoting osteochondral ossification on the other [141]. This approach allows reproduction of multiple tissues and tissue interfaces on the same implant.

We have also demonstrated a tunable pore layer thickness by pressing the PEEK further through the porous media. To do so required higher pressures as predicted by Darcy's Law for flow through a porous media which states that the pressure is proportional to the distance over which the pressure drop occurs [154]. A tunable layer thickness allows for an optimum balance of mechanical properties and porosity for bone ingrowth. Furthermore, variations in layer thickness allows for a wide range of implant designs for various applications.

Mechanical characterization showed that pore size has relatively little influence on the mechanical properties of PEEK-SP within the evaluated size range; no differences were found between PEEK-SP of the three different pore sizes. The data demonstrate that although the load-bearing capacity for all pore sizes decreases when using A_T , this is mostly a geometrical effect because their strength approaches that of PEEK-IM when calculated using A_{LB} . However, this will still influence the structural application of the material and

is an important consideration in implant design. Tensile tests also revealed that failure strains were decreased to below 50% of PEEK-IM, consistent with previous studies that showed that polymers experience a decrease in failure strain in the presence of notches while the effect on strength is typically marginal [155, 156]. There was no change in modulus with the addition of surface porosity when using A_{LB} . Due to the cyclic loading experienced by orthopaedic implants and the often detrimental decrease in the fatigue resistance of polymers with surface flaws [83, 157, 158], it was important to evaluate the fatigue resistance of PEEK-SP. All pore sizes demonstrated a high fatigue resistance at one million cycles when using A_{LB} despite a decrease in endurance limit from injection molded PEEK. It also appears that, qualitatively, PEEK-SP-450 had a slightly lower fatigue strength than PEEK-SP-250, in agreement with the finding that larger pores initiate more and larger fatigue cracks than small pores and therefore might have a greater effect on the fatigue life [159, 160]. Interfacial shear testing was also performed on PEEK-SP samples to investigate the mechanical integrity between the porous layer and solid core. No difference was found between PEEK-SP samples of different pore sizes. However, all PEEK-SP samples had higher interfacial shear strength than smooth PEEK, suggesting that any bone ingrowth will result in a mechanical interlock providing increased load-bearing area and higher bonding strength than smooth PEEK implants. Altogether, the mechanical properties of surface porous PEEK support its potential to bear physiologic loads with minimal risk of failure. For a clinical loading comparison, lumbar intervertebral discs experience loads of approximately 1000 - 3000 N depending on activity level, which is partially transferred to interbody implants after spinal fusion [161-163]. A simple stress calculation predicts that a PEEK-SP implant under such loading would require 25-80 mm²

of surface area to remain in the elastic regime and below the fatigue strength at one million cycles (38 MPa). Most common spinal fusion implants exceed this size, lending support for PEEK-SP.

In vitro data support the ability of PEEK-SP to facilitate bone cell proliferation and differentiation, following the sequence of events described in detail by Lian and Stein [164]. At early time points, cells exhibited increased proliferation on PEEK-SP compared to smooth PEEK, Ti6Al4V and TCPS. During this proliferative phase, cells are thought to produce the extracellular matrix proteins required for matrix mineralization [164]. Therefore, the reduced cell proliferation on smooth PEEK, Ti6Al4V, and TCPS (**Figure 5.11**) may have caused matrix production and mineralization to occur at later time points in comparison to PEEK-SP (**Figure 5.12A**). This point is further evidenced by the higher ALP activity of cells on smooth PEEK, Ti6Al4V, and TCPS at Day 14 (**Figure 5.12C**), suggesting that the cells and matrix were still preparing for mineralization. This is in contrast to cultures on PEEK-SP that were extensively mineralized by Day 14 and exhibited lower ALP activity levels, which can occur in heavily mineralized cultures and mature bone (**Figure 5.12C**) [164, 165]. This increased mineralization seen in PEEK-SP cultures was clearly cell-mediated and not due to the increased surface area of the porous layer. This is inferred by the lower calcium content of the acellular groups and nonmineralizing HEK cell groups, the cell layer forming a physical barrier to nonspecific mineral deposition onto the surface. Additionally, cells grown on TCPS exhibited similar temporal trends in ALP activity and mineralization as in a previous report [166], suggesting that PEEK-SP accelerated osteoblast differentiation rather than smooth PEEK and Ti6Al4V causing delayed differentiation. This increased osteogenesis and mineral

deposition is consistent with our previous study that showed bone ingrowth and direct bone apposition to PEEK-SP at 6 weeks compared to fibrous layer encapsulation on smooth PEEK implants [134].

One potential explanation for the initially increased cell proliferation on PEEK-SP is that the increased surface area effectively decreased the seeding density of cells, which could have facilitated greater cell proliferation at early time points [167, 168]. However, this increase in surface area and early proliferation did not translate to greater cell numbers at later time points (**Figure 5.12B**), even in growth media where there are fewer cues to cease proliferation. Although culturing under dynamic conditions likely enhanced nutrient transport within the pore layer compared to static culture [169], it is possible that cells on the surface of the porous layer caused more hypoxic conditions for the cells residing within the deeper pores, approaching 500 μm from the surface. Although our previous data suggest that this potential mass diffusion limitation is not a pronounced limitation *in vivo*, where blood vessels are able to perfuse the pore network and allow bone to penetrate the full depth of the pore layer [134], hypoxia is known to influence osteoblast differentiation and endochondral ossification [170, 171]. This hypothesis is supported by the increased VEGF production of MC3T3 cells on PEEK-SP groups (**Figure 5.13**), which is known to increase when MSCs and osteoblasts undergo hypoxic conditions [170, 172].

This study highlighted the ability of PEEK-SP to maintain high tensile and fatigue strength while presenting a surface that results in improved cellular response. Future studies will investigate the effect of pore size and pore layer depth on functional osseointegration *in vivo* within a preclinical animal model. In addition, further testing is needed to optimize the porosity to account for the tradeoff in bone ingrowth and

compressive strength. To predict clinical performance in a spinal fusion application, implants possessing a PEEK-SP surface will undergo biomechanical testing to evaluate insertion force into the intervertebral disc space and the degree of subsidence into the endplates.

5.5. Conclusions

In this study, we demonstrated that surface porous PEEK can be created with a tunable porous architecture. The results show that the introduction of a porous surface layer has the potential to provide an improved clinical outcome for polymeric implants while maintaining the necessary load-bearing capacity. Unlike other methods to improve the osseointegration of PEEK implants such as fully porous PEEK scaffolds [15], PEEK-SP retains the bulk mechanical properties necessary for orthopaedic applications while potentially accelerating bone cell proliferation and differentiation compared to smooth PEEK and Ti6Al4V. Therefore, PEEK-SP may offer improved stability and performance over current implants at the critical bone-implant interface. Recently this technology was FDA 510(k) cleared on the COHERE™ Cervical Interbody Fusion Device (Vertera Spine, Atlanta, GA), highlighting the clinical relevance of this study.

CHAPTER 6

IMPACT OF SURFACE POROSITY AND TOPOGRAPHY ON THE MECHANICAL BEHAVIOR OF HIGH STRENGTH BIOMEDICAL POLYMERS

6.1. Introduction

The use of polymers in biomedical applications has been rapidly increasing as the strength of biocompatible polymers has increased. From instrumentation to temporary and permanent implants, polymers have replaced metallic parts in select applications due to their favorable characteristics such as tailorable properties, easy and low-cost fabrication, resistance to environmental attack, and high-resolution magnetic resonance imaging (MRI) compatibility [173, 174]. However, implantable polymeric devices often suffer a key tradeoff in the form of poor osseointegration due to their inert and often hydrophobic surfaces. Osseointegration is critical for long-term success of implants as it is considered a prerequisite for implant loading and stability [175, 176]. Therefore, many studies have evaluated different methods to increase the osseointegration of polymers [177].

One method commonly accepted to improve the osseointegration of implants is to introduce a topologically varied surface, as high roughness is important in improving early cell behavior and achieving a stable long-term osseointegration of implants [49, 53] and studies have demonstrated the ability of implant surfaces with rough topographies to stimulate osteogenesis [60, 178]. In fact, the surface topography of substrates is often more essential than their surface chemistry for protein adsorption and the subsequent adhesion and proliferation of cells [56, 57]. A variety of methods are used to introduce topographical features including sand-blasting, acid etching, machining, heat treatments, anodic

oxidation, and combinations of these treatments [179]. Numerous studies have demonstrated enhanced bone-to-implant contact and push-out strength with an increase in surface roughness [49, 58] as well as an improved osteoconductive response at the cellular level [60, 180]. The effects of surface roughness on the *in vitro* response of osteoblasts and human mesenchymal stem cells (hMSCs) have been summarized in **Table 6.1** [178, 181-187].

Porous and porous-coated metallic implants have also been shown to promote osseointegration. Porosity promotes bone tissue formation by allowing migration and proliferation of osteoblasts and mesenchymal cells, as well as vascularization [188]. Surface porous cobalt-chrome implants placed in the mandibles of canines demonstrated increased bone growth and showed more extensive bone formation within the surface pores with time compared to threaded implants [52].

Table 6.1. The effects of surface roughness on the *in vitro* response of osteoblasts and human mesenchymal stem cells (hMSCs). The roughness (Ra) of rough samples in these studies ranged from 2-7 μ m and the smooth comparisons from 0.2-0.6 μ m.

Effects of Increasing Surface Roughness on Osteoblasts and hMSCs	<ul style="list-style-type: none"> ↓ cell numbers due to lower proliferation ↑ differentiation markers (e.g. alkaline phosphatase and osteocalcin) ↑ secretion of bone morphogenetic proteins, transforming growth factor-β1 and 2, and Wnts ↑ production osteoprotegerin ↑ secretion of angiogenic factors (e.g. vascular endothelial growth factor and fibroblast growth factor 2) ↑ levels of anti-inflammatory cytokines ↓ levels of pro-inflammatory cytokines
--	---

In addition, a porous surface can provide greater mechanical stability at the bone-implant interface by increasing the interlocking between the implant biomaterial and the surrounding natural bone [189]. Titanium alloy implants treated with sintered porous coating showed enhanced shear strength when implanted in sheep tibiae while further coating with hydroxyapatite beads did not result in significant improvement [190]. In a study using a rat ectopic model using solid and porous particles of hydroxyapatite for BMP-2 delivery, no new bone formed on the solid particles, while in the porous scaffolds direct osteogenesis occurred [188]. In other studies, porosity has been shown to stimulate osteogenesis and create a mechanical interlock at the bone-implant interface that leads to greater implant stability [17, 76].

Though the literature suggests that increased surface roughness or introduction of porosity is important in achieving stable long-term osseointegration of implants, these topographical modifications will reduce the monotonic and cyclic strength needed for load-bearing orthopaedic implants. In polymers, monotonic fracture typically originates from local stress concentrations at flaws, scratches, or notches similar to those on rough and porous surfaces [191]. Surface topography is even more critical for fatigue performance, as fatigue fracture generally starts at the surface and propagates inward with increasing cycle number [192]. The presence of notches or scratches on a specimen can greatly reduce fatigue life, especially for notch-sensitive materials [193]. The negative effect of surface flaws on fatigue performance has been studied extensively in metals [194, 195] and ceramics [196] and has also been shown to drastically reduce fatigue life in polymers [192]. Porosity can also decrease mechanical properties by reducing the effective load-bearing cross-sectional area and introducing stress concentration sites for strain localization and

damage, decreasing both strength and ductility [197, 198]. Therefore, a tradeoff exists between increasing the osseointegration capacity of implants via surface roughness and porosity and the corresponding mechanical integrity to bear physiologic loads [199, 200].

While the literature demonstrates an improvement in the osseointegration of implant materials by increasing topographical variations, minimal work has been done to determine the effects of roughness and porosity on the load-bearing capacity of high strength polymers. In this chapter we show that surface roughness and surface porosity both negatively impact the mechanical properties of high-strength polymers with the extent of the effect dependent on polymer chemistry and structure. Correlations are drawn between basic material properties to help understand the impact of the porosity and surface roughness on monotonic and cyclic properties. Abrasive sanding was used to create grooves in both the longitudinal and transverse directions on samples and the results demonstrated that the transverse grooves have a greater effect on the mechanical behavior of the materials. Additionally, surface porosity was created on samples as described in previous chapters [134]. In general, the effect of surface porosity was more severe than surface roughness. In addition, the failure strain was more sensitive to surface defects than the strength of the polymers tested. While all polymers experienced a decrease in mechanical properties in response to various surface topographies, crystalline polymers were found to exhibit the least significant change due to the availability of a more effective local dissipation mechanism. Though not all the polymeric biomaterials studied here are used as permanent implants in humans, the study will provide an understanding of the effect of surface modifications for the design of new high strength implants. Finally, due

to its widespread use as a common orthopaedic implant material and superior properties, we chose to further examine PEEK to better understand the observed results.

6.2. Materials and Methods

6.2.1. Materials

Polycarbonate (PC), polyetheretherketone (PEEK), polyethersulfone (PES), polyphenylsulfone (PPSU), polyphenylene sulfide (PPS), and a PEEK/PPSU blend were provided as ASTM D638 Type I dog-bone samples by Solvay Advanced Polymers (Alpharetta, GA). Fracture toughness values were provided by the manufacturer.

Surface roughened samples were prepared by sanding the surface using 50 grit multi-purpose sandpaper as described in **Chapter 3**. To determine whether the effect of surface roughness was due to the cumulative effects of surface defects, additional PEEK samples were prepared according to the same sanding protocol but with the sanding limited to a 12.7mm x 12.7mm area in the center of the gauge section. Surface porous polymer samples were created using the melt extrusion and porogen leaching process described in **Chapter 3**. To control for pore size, sodium chloride was sieved using #50 and #40 U.S. mesh sieves resulting in salt crystals 312-425 μm in diameter. Surface porous samples will be referred to as “polymer name”-SP. To determine whether the effect of surface porosity was due to the cumulative effects of surface defects, additional PEEK samples were prepared according to the same protocol but with the processing modified to yield porosity on just one side (samples referred to as PEEK-SP-1-sided).

To examine the effect of thermal processing on surface porous samples, PEEK samples with lower crystallinity were prepared by rapid cooling from the melt (PEEK-SP-

Q). These samples were quenched in water immediately after the surface porous processing, in contrast to the room temperature cooling in the other surface porous samples. Annealed samples were first quenched and then annealed at either 180°C or 300 °C for 1 hour (PEEK-SP-QA180 and PEEK-SP-QA300, respectively). Characterization of the pore microstructure and crystallinity was performed as outlined in **Chapter 3**.

6.2.2. Methods

Tensile and fatigue tests were run according to the methods described in **Chapter 3**.

6.2.3. Statistical Analysis

Statistically significant differences were determined using a one-way ANOVA and Tukey post hoc analysis (95% confidence interval).

6.3. Results

6.3.1. Stress-strain behavior of injection molded, as-received polymer samples

Average values of the uniaxial mechanical behavior of the five different polymers are summarized in **Table 6.2**. As the data shows, the polymers used in this study represent a wide range of mechanical properties. The majority of the polymers failed after large plastic deformation and the ultimate stress (strength) was due to ductile yielding. However, PPS experienced brittle failure with no yield point observed and therefore the maximum stress was due to abrupt failure. It is important to note that these failure modes are dependent on molecular weight and are therefore specific to the polymers tested in this study. Though the PPS used here does not yield, higher molecular weight grades of PPS may show yielding.

Table 6.2. Tensile strength, failure strain, elastic modulus, and toughness values of the polymers used in this study (n=5). Values represent the average \pm one standard deviation.

Sample	Ultimate Tensile Strength (MPa)	Failure Strain (%)	Modulus (GPa)	Toughness (MPa)
PEEK	97.7 \pm 1.0	20.2 \pm 2.4	3.34 \pm 0.14	32.5 \pm 3.6
PEEK/PPSU	88.7 \pm 2.7	83.1 \pm 5.1	3.01 \pm 0.08	51.4 \pm 14
PPSU	76.9 \pm 2.7	71.2 \pm 8.1	2.14 \pm 0.08	45.6 \pm 6.4
PC	64.2 \pm 1.8	94.1 \pm 20	2.26 \pm 0.09	54.2 \pm 15
PES	88.7 \pm 4.5	75.4 \pm 27	2.61 \pm 0.09	47.0 \pm 17
PPS	88.7 \pm 3.9	3.71 \pm 0.64	3.59 \pm 0.03	2.1 \pm 0.62

6.3.2. Surface characterization

The surface roughness of the polymers with various surface conditions is shown in **Table 6.3**. Roughened samples had a surface roughness significantly higher than the injection molded samples ($p < 0.00001$). Representative images of the various PEEK surfaces are shown in **Figure 6.1**. Strut size, strut spacing, porosity, and layer thickness as determined by μ CT analysis for the surface porous samples is summarized in **Table 6.4** and a representative cross-section is shown in **Figure 6.2**. **Table 6.4** also compares the pore morphometry to various human bones [88].

Table 6.3. Surface roughness values (R_a in μ m) of the surface roughened polymers tested compared to injection molded samples (n=5). Values represent the average \pm one standard deviation.

	Injection Molded	Longitudinal	Transverse
PEEK	0.0636 \pm 0.014	2.63 \pm 0.22	2.17 \pm 0.26
PEEK/PPSU	0.0658 \pm 0.013	1.68 \pm 0.15	2.51 \pm 0.35
PPSU	0.0230 \pm 0.0010	2.20 \pm 0.19	1.54 \pm 0.41
PC	0.0318 \pm 0.0020	2.06 \pm 0.16	1.84 \pm 0.37
PES	0.0390 \pm 0.040	1.91 \pm 0.22	1.61 \pm 0.13
PPS	0.0456 \pm 0.0050	2.19 \pm 0.28	2.26 \pm 0.19

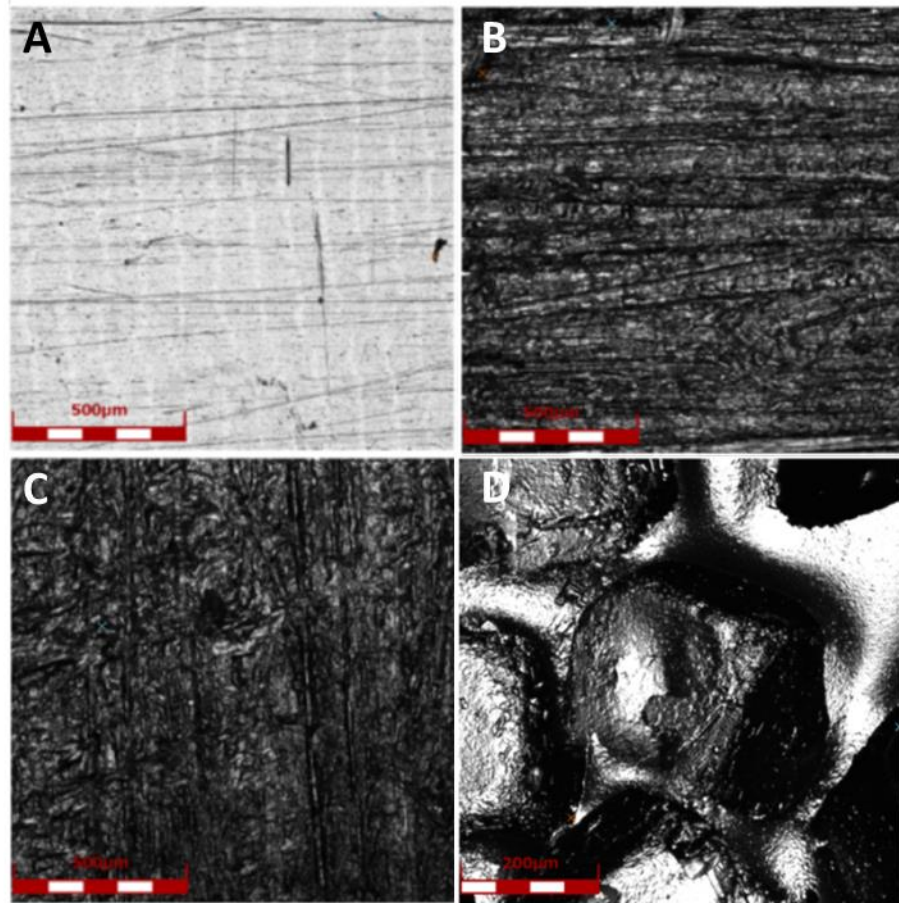


Figure 6.1. Representative images of the surface of PEEK taken via the LEXT microscope: (A) injection molded, (B) longitudinally roughened, (C) transversely roughened, and (D) surface porous.

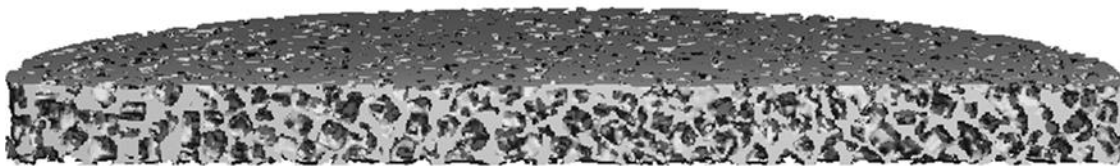


Figure 6.2. Representative μ CT reconstructions of the surface and cross section of PEEK-SP.

Table 6.4. Strut spacing, strut thickness, percent porosity, and pore layer thickness of the surface porous polymers used in this study. Values represent the average \pm one standard deviation.

Sample	Strut Spacing (μm)	Strut Thickness (μm)	Porosity (%)	Pore Layer Thickness (μm)
PEEK	208 \pm 4.9	104 \pm 8.4	61.2 \pm 2.6	396 \pm 62
PEEK/PPSU	273 \pm 5.9	121 \pm 34	70.4 \pm 3.4	444 \pm 98
PPSU	259 \pm 19	152 \pm 18	60.9 \pm 3.7	379 \pm 85
PC	250 \pm 20	130 \pm 23	66.7 \pm 5.9	688 \pm 110
PES	222 \pm 18	130 \pm 4.7	61.4 \pm 4.0	805 \pm 100
PPS	263 \pm 16	120 \pm 11	69.5 \pm 6.2	435 \pm 96
Iliac Crest	747 \pm 150	151 \pm 27	84.4 \pm 5.5	—
Lumbar Vertebrae	854 \pm 143	139 \pm 28	91.3 \pm 3.3	—
Femoral Head	638 \pm 114	194 \pm 33	73.9 \pm 7.8	—
Calcaneal Core	679 \pm 107	129 \pm 18	88.0 \pm 3.5	—

6.3.3. Stress-strain behavior of surface roughened and surface-porous polymers

Representative uniaxial mechanical behavior of the polymers with various surface conditions is shown in **Figure 6.3** and average values of the mechanical behavior are summarized in **Table 6.5**. Overall, depending on the polymer chemistry and structure, samples with a rough surface had significantly lower strength and failure strain. In general, transversely roughened samples had a significantly lower failure strain than longitudinally roughened samples but no significant change in strength. The introduction of porosity led to a further decrease in strength and failure strain. To summarize, all topographical changes led to a significant decrease in strength and failure strain with the magnitude of the decrease being greatest for samples with a surface porosity and least for longitudinally roughened samples. To compare the effects of surface topography on the different polymers, the change in toughness with topography is shown in **Figure 6.4**. While all polymers experienced a drastic decrease in toughness, PPS was the least sensitive while PES was the most.

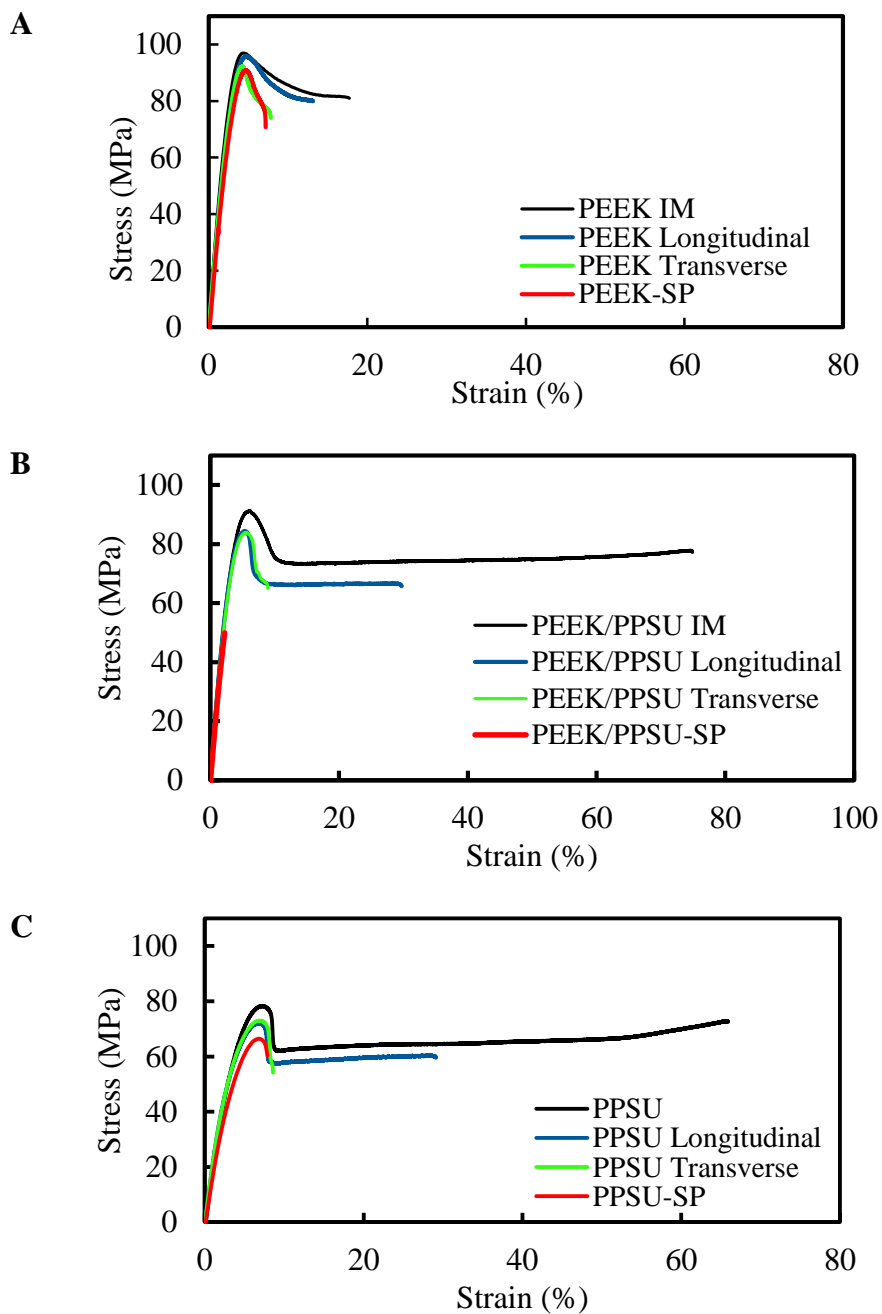


Figure 6.3 Representative stress-strain curves of the polymers with different surface conditions: (a) PEEK, (b) PEEK/PPSU, (c) PPSU, (d) PC, (e) PES, (f) PPS.

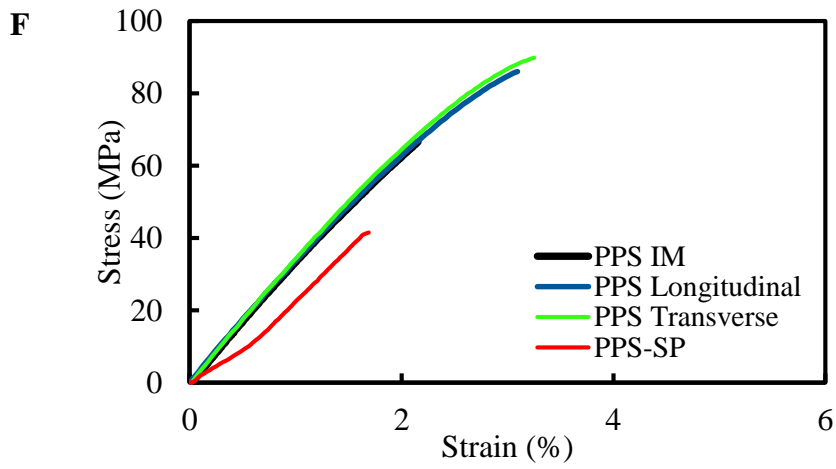
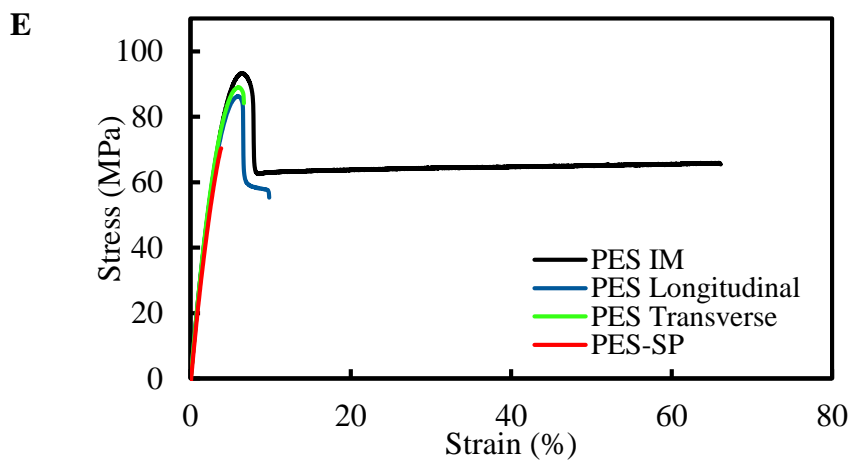
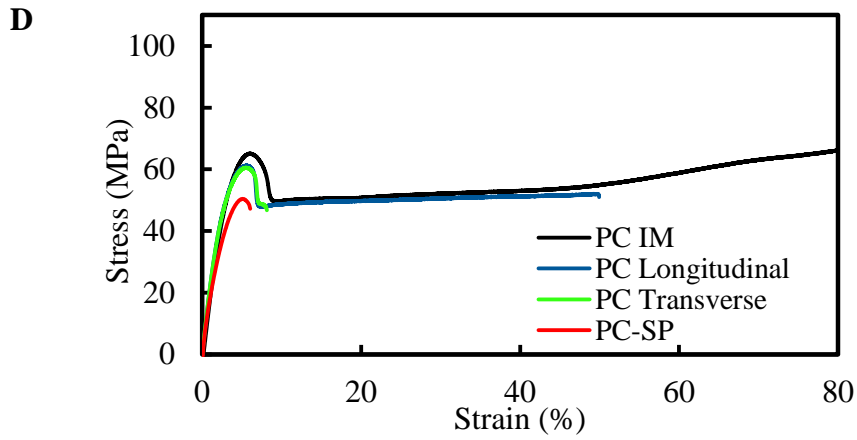


Figure 6.3. Continued

Table 6.5. Measured strength, failure strain, modulus, and toughness of the polymers with different surface conditions (n=5). Values represent the average \pm one standard deviation. (* designates statistical difference between modified samples and injection molded samples, # between longitudinal and transverse samples, and ^ between transverse and surface porous with $p < 0.05$).

	Max Stress (MPa)	Failure Strain (%)	Modulus (GPa)	Toughness (MPa)
PEEK				
IM	97.7 \pm 0.99	20.2 \pm 2.4	3.34 \pm 0.14	32.5 \pm 3.6
Axial	93.6 \pm 2.25*	13.6 \pm 2.8*	3.27 \pm 0.20	17.9 \pm 5.4* [#]
Transverse	91.2 \pm 1.1*	8.83 \pm 0.98*	3.33 \pm 0.04	5.92 \pm .73* [#]
SP	96.1 \pm 2.6 [^]	7.79 \pm 2.3*	3.36 \pm 0.30	4.64 \pm .63*
PEEK/PPSU				
IM	88.7 \pm 2.7	83.1 \pm 5.1	3.01 \pm 0.08	51.4 \pm 14
Axial	84.5 \pm 1.7*	28.3 \pm 9.7* [#]	2.84 \pm 0.12*	20.3 \pm 6.5* [#]
Transverse	83.2 \pm 0.67* [^]	8.58 \pm 1.2* ^{#^}	2.78 \pm 0.09*	5.79 \pm 1.0* ^{#^}
SP	41.4 \pm 8.5* [^]	2.82 \pm 0.84* [^]	2.85 \pm 0.29*	0.966 \pm 0.50* [^]
PPSU				
IM	76.9 \pm 2.7	71.2 \pm 8.1	2.14 \pm 0.08	45.6 \pm 6.4
Axial	72.0 \pm 0.40*	34.3 \pm 8.1* [#]	2.15 \pm 0.06	19.7 \pm 4.8* [#]
Transverse	71.8 \pm 0.87* [^]	8.78 \pm 0.82* [#]	2.15 \pm 0.02 [^]	4.59 \pm 0.45* ^{#^}
SP	66.0 \pm 4.9* [^]	7.53 \pm 1.2*	1.78 \pm 0.26* [^]	3.43 \pm 0.80* [^]
PC				
IM	64.2 \pm 1.8	94.1 \pm 20.1	2.26 \pm 0.09	54.2 \pm 15
Axial	61.4 \pm 0.20*	42.6 \pm 13* [#]	2.26 \pm 0.02	21.1 \pm 6.8* [#]
Transverse	61.5 \pm 1.5* [^]	8.9 \pm 1.5* ^{#^}	2.26 \pm 0.04	4.11 \pm 0.71* ^{#^}
SP	53.8 \pm 4.1* [^]	5.82 \pm 0.53* [^]	2.15 \pm 0.22	2.15 \pm 0.31* [^]
PES				
IM	88.7 \pm 4.5	75.4 \pm 27	2.61 \pm 0.09	47.0 \pm 17
Axial	87.3 \pm 1.6	10.2 \pm 2.0* [#]	2.68 \pm 0.05	5.73 \pm 2.1*
Transverse	89.3 \pm 1.3t	6.68 \pm 0.17* ^{#^}	2.68 \pm 0.05 ^t	4.09 \pm 0.14* ^t
SP	51.8 \pm 14.4* [^]	3.44 \pm 0.98* [^]	1.91 \pm 0.46* [^]	0.868 \pm 0.48* [^]
PPS				
IM	88.7 \pm 3.8	3.71 \pm 0.64	3.59 \pm 0.03	2.09 \pm 0.62
Axial	86.0 \pm 4.0	3.69 \pm 1.3	3.48 \pm 0.07	1.99 \pm 1.10
Transverse	88.3 \pm 3.1 [^]	3.53 \pm 0.53 [^]	3.50 \pm 0.05	1.97 \pm 0.65 [^]
SP	53.2 \pm 20* [^]	1.83 \pm 0.77* [^]	3.30 \pm 0.22	0.557 \pm 0.46* [^]

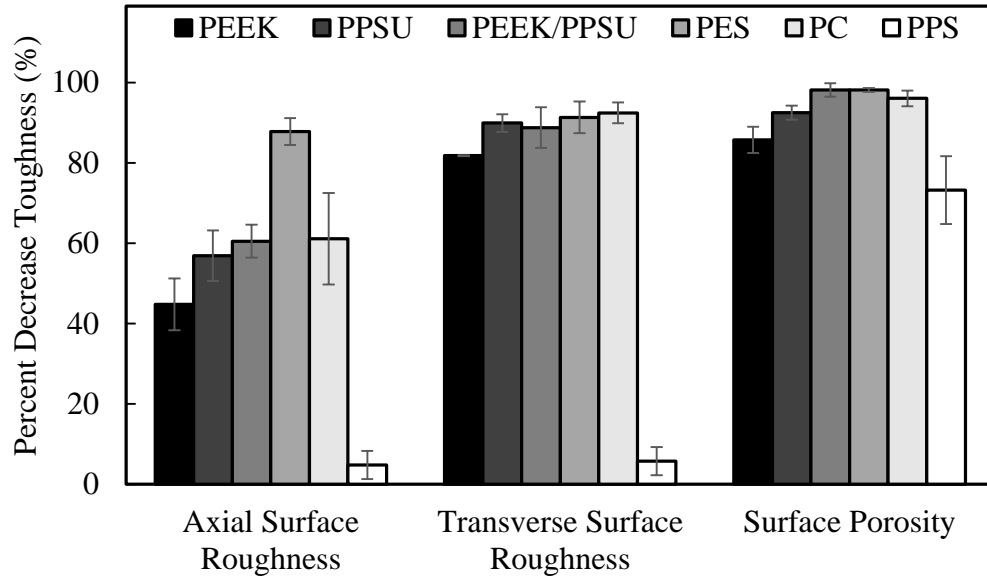


Figure 6.4. The change in toughness with various surface topographies relative to injection molded samples.

6.3.4. Fatigue of tested polymers

Tensile fatigue tests were run on all surface conditions for PEEK, injection molded and surface porous conditions for PPSU, PEEK/PPSU, and PC, and on injection molded PES and PPS (**Figure 6.5**). As expected, the surface roughness and surface porosity decreases the fatigue strength of PEEK in the high cycle regime. Similar to the tensile data, the transverse grooves had a greater effect than longitudinal samples and the effect of surface porosity was greater than either roughened samples. The stress at which runout occurred (1,000,000 cycles) was 76.9 MPa for longitudinally roughened, 75.0 MPa for transversely roughened, and 60.0 MPa (72.7% of injection molded PEEK) for PEEK-SP compared to 82.6 MPa for injection molded PEEK. The runout stress at 100,000 cycles was 9.90 MPa for PPSU-SP (15.7% of injection molded PPSU) and 10.8 for PC-SP (25.5% of injection molded PC).

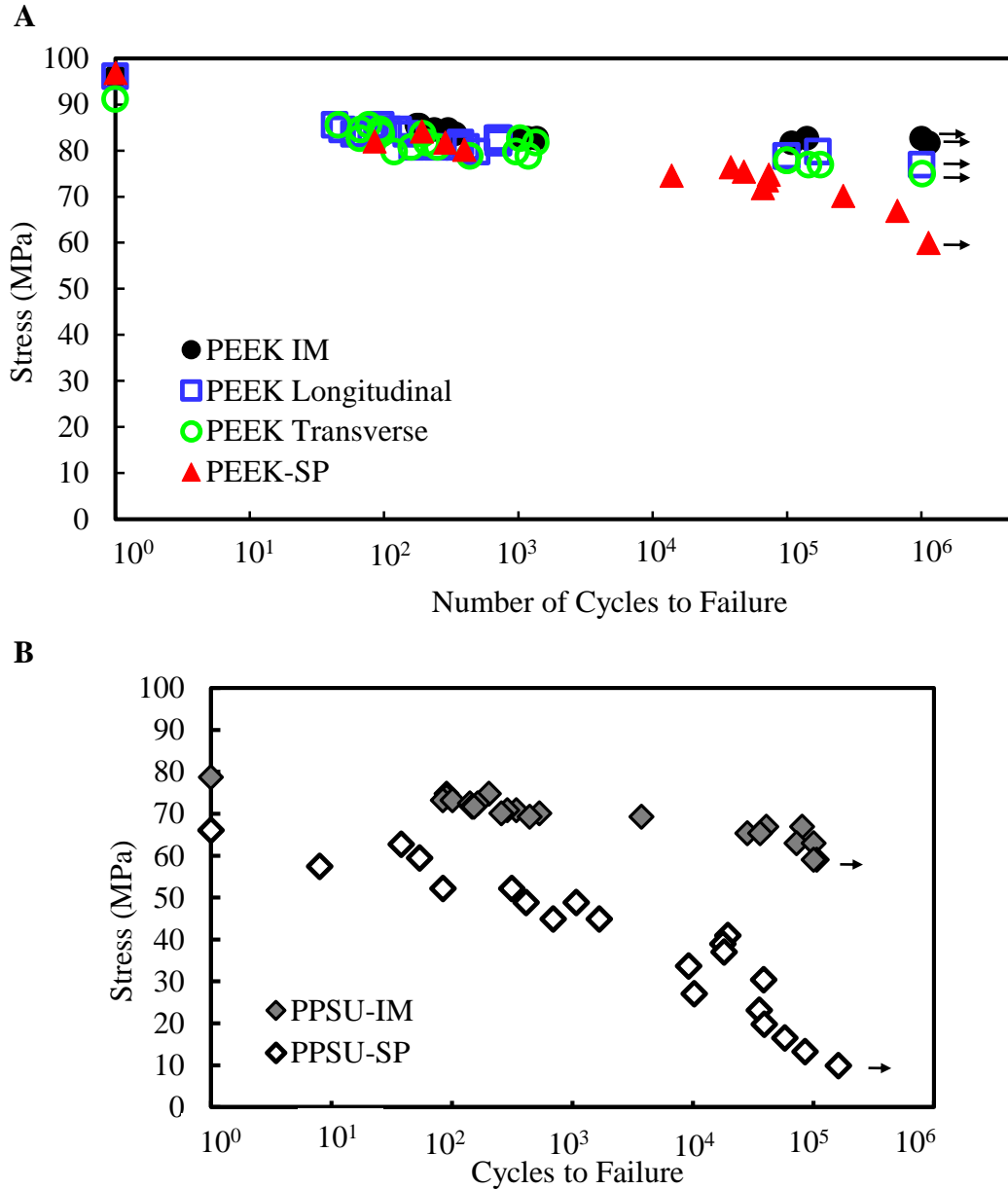


Figure 6.5. S–N curves comparing the fatigue behavior with various surface conditions: (a) PEEK, (b) PPSU, (c) PEEK/PPSU, (d) PC, (e) PES, (f) PPS. Arrows denote tests that were halted after reaching 10^6 cycles for PEEK samples and 10^5 cycles for the other polymers, which is defined as the runout stress.

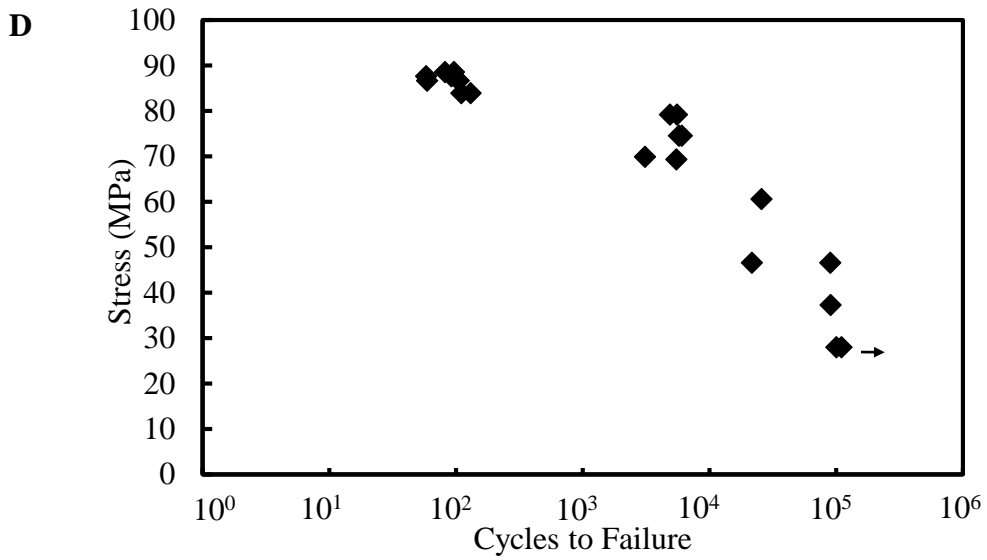
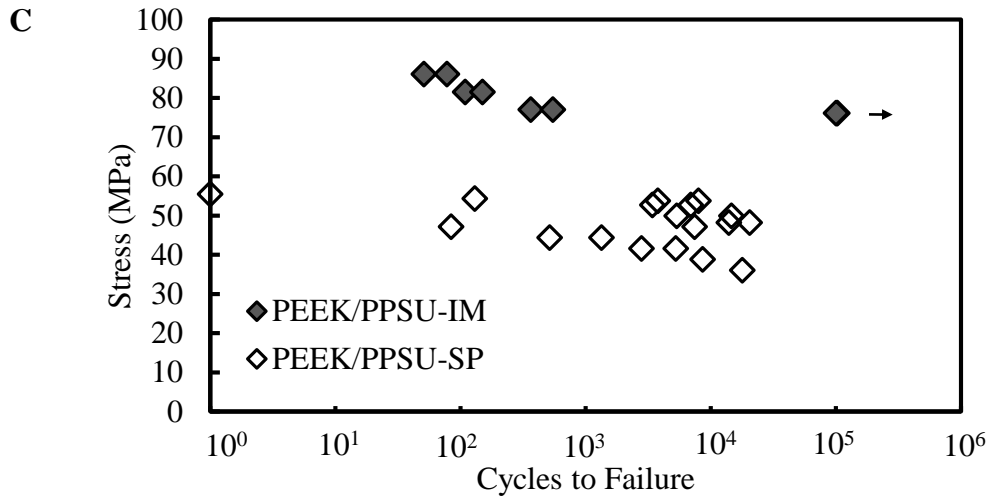


Figure 6.5. Continued

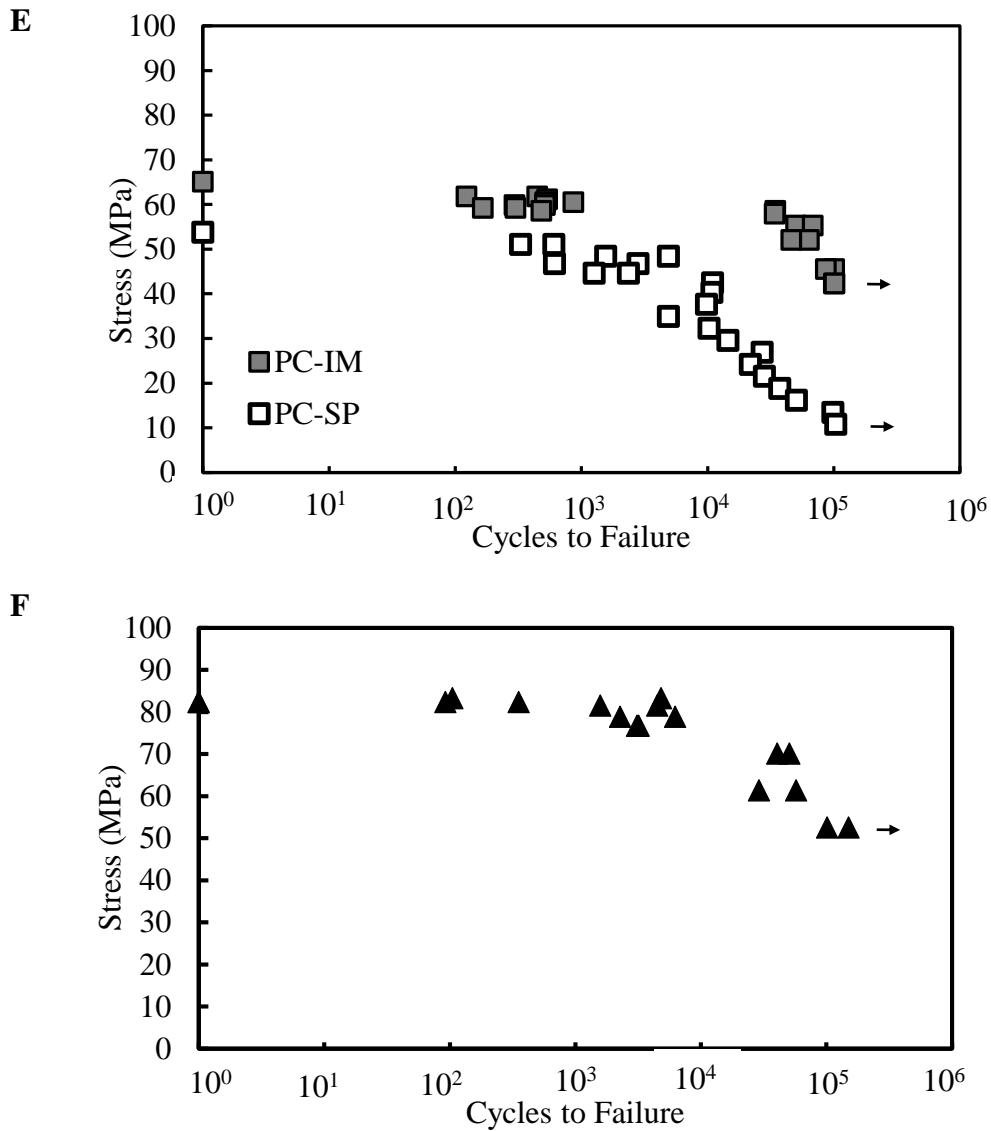


Figure 6.5. Continued

6.3.5. Crystallinity measurements of quenched and annealed PEEK

DSC and FTIR were used to determine the crystallinity of the PEEK samples after various thermal processing conditions. **Table 6.6** shows that the crystallinities from DSC and FTIR are in relative agreement with each other in terms of the ordering of the materials by crystallinity. The data demonstrate that the melt extrusion and salt-leaching process results in significantly higher crystallinity than injection molded PEEK ($p < 0.01$). In

addition, quenching did significantly lower the crystallinity of the PEEK ($p < 0.01$) while annealing at 300°C increased the crystallinity compared to annealing at 180 °C as expected ($p < 0.05$). Annealing at 300°C resulted in crystallinities near the as-processed surface porous samples.

Table 6.6. Percent crystallinity of PEEK with various thermal processing histories as measured by FTIR and DSC. Values represent the average \pm one standard deviation. * designates statistical difference between groups and IM ($p < 0.01$) and ^ significance between SP-QA180 and SP-QA300 ($p < 0.05$).

	FTIR	DSC
IM	22.1 \pm 3.3	23.6 \pm 0.14
SP	29.3 \pm 0.61*	27.2 \pm 0.35*
SP-Quenched	15.7 \pm 1.6*	20.0 \pm 0.92*
SP-QA180	23.7 \pm 2.9^	26.2 \pm 1.1^
SP-QA300	28.3 \pm 2.1^	32.7 \pm 1.3^

6.3.6. Stress-strain of quenched and annealed PEEK

Quenching significantly lowered the yield strength of PEEK-SP from 93.38 ± 1.49 MPa to 82.29 ± 1.42 MPa and modulus from 3.28 ± 0.21 GPa to 2.80 ± 0.04 GPa but did not significantly increase the failure strain. Quenching followed by annealing increased the yield strength significantly from quenched samples (180°C anneal: 94.92 ± 3.16 MPa, 300°C anneal: 98.22 ± 1.15 MPa) with no significant loss in ductility (**Figure 6.6**). The data is summarized in **Table 6.7**.

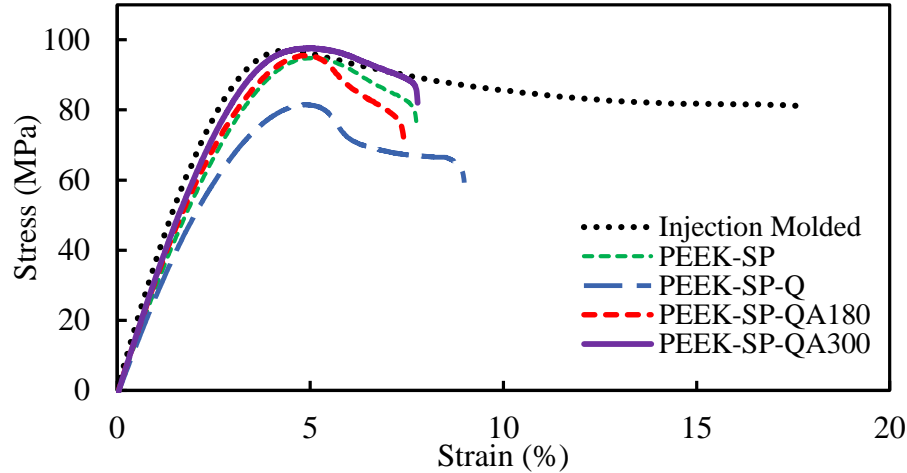


Figure 6.6. Representative stress-strain curves of PEEK with various thermal processing histories.

Table 6.7. Measured strength, failure strain, and modulus of the polymers with different thermal processing histories (n=5). Values represent the average \pm one standard deviation. (* designates statistical difference between surface porous samples and injection molded samples and # between the quenched/annealed samples and the as-processed PEEK-SP with $p < 0.05$).

Sample	Load-Bearing Stress		Modulus (ALB)
	(MPa)	Strain (%)	
PEEK-IM	97.7 ± 0.99	20.2 ± 2.4	3.34 ± 0.14
PEEK-SP	$93.4 \pm 1.5^*$	$6.97 \pm 0.86^*$	3.28 ± 0.21
PEEK-SP-Q	$82.3 \pm 1.4^{* \#}$	$8.42 \pm 1.4^*$	$2.80 \pm 0.04^{* \#}$
PEEK-SP-QA180	94.9 ± 3.2	$7.14 \pm 0.75^*$	3.18 ± 0.18
PEEK-SP-QA300	$98.2 \pm 1.2^{\#}$	$7.42 \pm 1.1^*$	3.44 ± 0.06

6.3.7. Stress-strain of cumulative or local stress concentration testing

The mechanical properties of PEEK with 4 different surface topographies – transversely roughened, small area transversely roughened, PEEK-SP, and PEEK-SP-1-sided – are summarized in **Table 6.8**. No significant differences were found between the small area transversely roughened samples and the transversely roughened samples. Likewise, no significant differences were found between the PEEK-SP-1-sided and PEEK-SP samples. It was also noted that all small area transversely roughened samples broke in

Table 6.8. Measured strength, failure strain, and modulus of samples tested to understand whether topographical effects were cumulative. Values represent the average \pm one standard deviation.

Results	Tensile Strength (MPa)	Failure Strain (%)	Modulus (GPa)
Transversely Roughened	91.2 \pm 1.1	8.83 \pm 0.98	3.33 \pm 0.04
Small Area Transverse Sanding	93.9 \pm 0.48	8.54 \pm 0.56	3.51 \pm 0.04
PEEK-SP	93.4 \pm 1.5	6.97 \pm 0.86	3.28 \pm 0.21
PEEK-SP-1-sided	94.0 \pm 3.6	7.10 \pm 0.38	3.37 \pm 0.28

the region of roughness. These results indicate that the effect of surface defects are not cumulative over the entire sample but are instead a local effect.

6.4. Discussion

Due to widespread clinical application during the past few decades, the impact of surface topography and porosity on metals has been very well studied from mechanical and biological points of view [49, 190, 201, 202]. Microroughness has been shown to promote expression of integrin subunits regulating osteoblast differentiation [203], angiogenic growth factors [186, 204] and bone morphogenetic proteins [184]. In addition, microtextured surfaces can lead cells to produce factors that modulate bone resorption [178, 187]. This cell-mediated improvement in the environment can lead to increased implant stability, evidenced by the excellent correlation between the average surface roughness of implant surfaces and pushout failure load [59].

Porosity can further promote osseointegration by serving as a scaffold for bone regeneration. Porous and porous coated implants have demonstrated increased bone

formation [188] and higher interfacial shear strengths [190]. In polymers, tissue engineering efforts and cell culture studies have provided sound understanding of the effects of porosity and surface modification on biological properties of polymers [15, 177]. However, the impact of surface topography, and particularly surface porosity, on the strength and fatigue of high strength polymers has not been thoroughly examined and only recently have surface porous polymers found their way into clinical application. The goal of this chapter was to characterize the effect of surface topography and particularly surface porosity on the mechanical properties of polymers with varying chemistries and structures.

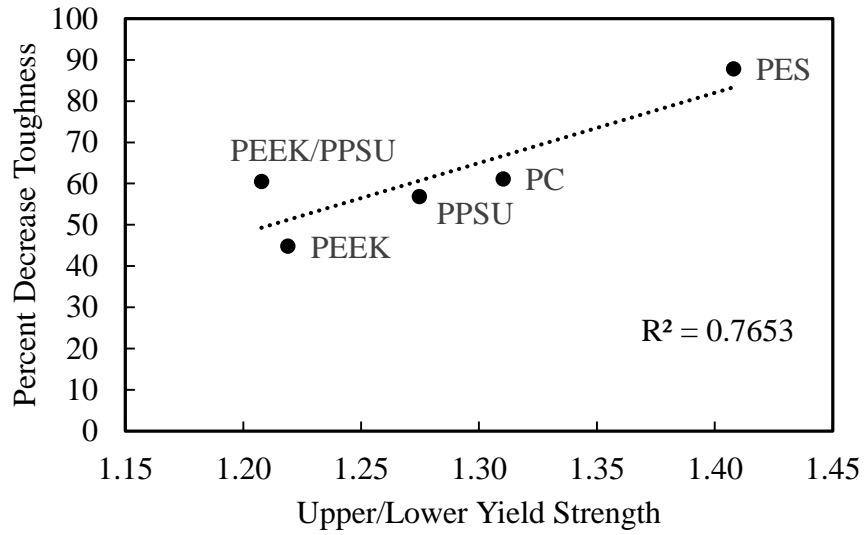
In order to first determine how sensitive the polymers were to surface finish in general, without the impact of pores, rough polymeric samples were created via sanding with the abrasive grooves oriented in either longitudinal or transverse directions. Mechanical characterization revealed that, in general, rough samples had a lower strength and failure strain than their injection molded counterparts. However, the moduli of roughened samples were not significantly different from injection molded samples, in agreement with previous findings that Young's modulus is insensitive to surface defects that constitute a low volume fraction of the overall cross section [205-207]. The data also demonstrated that the transversely roughened samples had a greater decrease in mechanical properties than the longitudinally roughened samples (average decrease in toughness of $73.9 \pm 21\%$ between transverse and longitudinal samples). This finding is expected, as transverse flaws will cause higher stress concentrations in tension and is well known in metals [194].

Using a melt extrusion and salt-leaching process, surface porous samples with a controlled pore structure were created. As demonstrated by the data, surface porosity

decreased both the strength and ductility of all polymers tested (**Figure 6.3**) as pores are stress concentrators that serve as nucleation sites for the creation of microfractures [208]. Overall, the effect of surface porosity on the mechanical properties of polymers is more severe than the effect of roughness even when the load bearing area is used to account for the impact of missing material volume.

While it is clear that surface topography has a significant impact on the mechanical properties of polymers, the modified surfaces did not impact the different polymers to the same extent. It is well known that different polymers have varying degrees of notch-sensitivity. For example, polycarbonate's impact strength essentially drops to zero as the sharpness of the notch increases; however, other polymers such as rubber-modified styrenes show almost no notch sensitivity [86]. The shape of the stress-strain curve is an important predictor of a polymer's notch sensitivity and several important trends have been identified [155, 209]. As the ratio of the upper yield strength (maximum value of the stress corresponding to the yield point) to the lower yield strength (minimum value of the stress just after the yield point) decreases, the notch sensitivity tends to decrease. The notch sensitivity of a polymer also tends to increase with increasing elongation to break of the unnotched polymer. Our data is consistent with both of these observations (**Figure 6.7**). The literature does not provide a thorough explanation of why the observed trends occur. However, the data indicates that in polymers with a high ratio of upper to lower yield strength, the gross movement of polymer chains that occurs at the upper yield is relatively easy past the yield point as indicated by the lower yield strength. Therefore, in polymers with a high upper yield point but low lower yield, it may be hard to initiate plastic deformation, but once active, deformation continues with less required energy. The

A



B

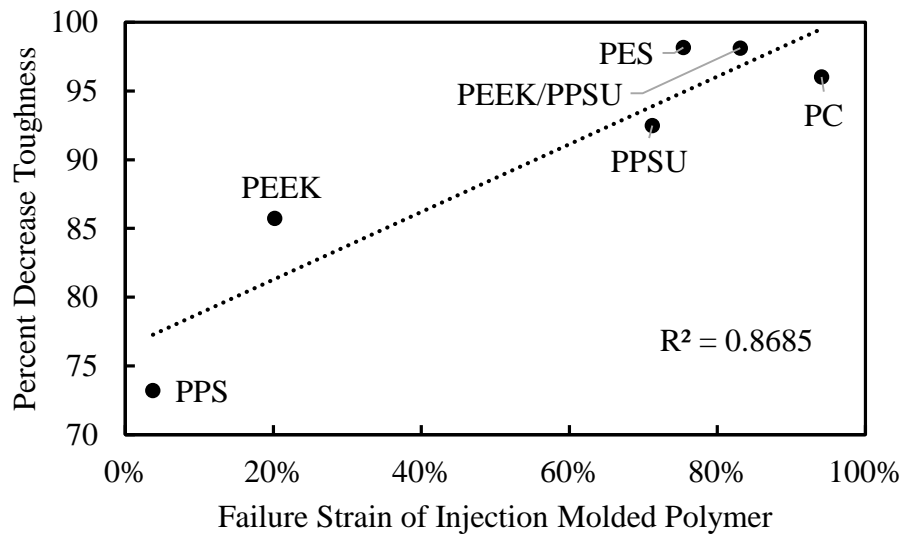


Figure 6.7. (A) The percent decrease in toughness from injection molded samples with longitudinal roughness as a function of the ratio of the upper to lower yield strength. (B) The percent decrease in toughness from injection molded samples with surface porosity as a function of the failure strain of injection molded samples.

difficulty for a polymer with a high upper yield point and low lower yield point is that once active, local dissipation mechanisms are relatively ineffective and may allow large local strains and early damage. These mechanisms are numerous and depend on the complexity of the polymer chain [210]. For example, a study on polycarbonate identified deformation mechanisms that included phenylene ring rotations, carbonate group reorientations, and isopropylidene group rearrangements [211]. In polymers with a low ratio of upper to lower yield strength, continued deformation after yield and gross chain movement is more difficult. Polymers with this smoother transition possess local dissipation mechanisms that remain as reasonable barriers to further local deformation and fracture. The yield strength, therefore, is analogous to the activation energy in a chemical reaction. These results are also in agreement with the finding that the greatest effect of notches is the severe decrease in elongation to break and toughness, with much less of an effect on yield strength [155, 156].

From a broad perspective, the impact of notches and surface topography on strength depends largely on the capacity of the geometrical defect to completely embrittle the polymer. If the ductility is decreased in a way that that circumvents gross yield, then the strength can drastically decrease. For example PEEK (**Figure 6.3a**) still yields when surface porous and thus has comparable strength levels to the smooth state while PEEK blended with PPSU (**Figure 6.3b**) has a dramatic decrease in strength with porosity due to embrittlement and failure occurring in the elastic regime.

From a local point of view, the effect of notches and surface flaws can be explained by the following four main effects: (1) Notches act as stress concentrators and create non-uniform stress fields resulting in high local stresses. (2) The local strain rate at the notch

tip is magnified and is greater than elsewhere in the part. (3) A triaxial stress state is created in the region of the notch. (4) High local strain hardening is produced ahead of the notch tip [155, 209]. In addition to the loss in toughness, these effects can change the fracture mode from ductile to brittle behavior. The ability of a material to deform plastically near the notch is important in determining the polymers notch sensitivity and tendency toward brittle fracture. However, in polymers the availability of a dissipation mechanism for plastic flow is necessary but insufficient to have low notch sensitivity. This dissipation mechanism must have sufficient strength as well, highlighted by the correlation with notch sensitivity and the ratio of upper and lower yield strength and not only with absolute ductility.

It is important to consider that notch sensitivity is an extremely complex property influenced by many factors in addition to the chemical structure of the polymers [155]. These factors include the method of fabrication, the molecular orientation, the moisture content, the thermal history, and the crystallinity of the specimens. Our results demonstrate that PEEK and PPS, the two crystalline polymers tested in this study (22.8% and 39.0% crystalline, respectively) had the smallest percent decrease in toughness for all three surface modifications. In general, polymers with increased crystallinity are more resistant to crack propagation than completely amorphous polymers as the two-phase structure provides a barrier to crack propagation and can accommodate both amorphous and crystalline modes of plasticity [77-79]. Furthermore, crystallinity is a property known to drive the mechanical properties such as yield strength, modulus, and impact resistance [212]. The availability of the plastic deformation at or near the crystalline regions and the confinement of plasticity

in the amorphous regions provides an effective local dissipation mechanism for mitigating the impact of local stress concentrations on mechanical behavior.

To help us further understand the observed findings, namely why the strength of PEEK-SP is highly preserved, the percent decrease in strength for each polymer was plotted versus other known material properties that may provide insight into the reasons for observed experimental behaviors. Though crystallinity helps explain the preservation of toughness, it alone cannot account for the percent decrease in strength, nor did a trend exist when percent decrease in strength was plotted versus the Notched Izod strength or the toughness. However, when the percent decrease in strength is plotted versus the fracture toughness, a strong correlation is observed (**Figure 6.8**).

Fracture toughness is a property which measures the capacity of a material containing a crack to resist fracture by quantifying the relative magnitude of the local stress fields at the crack tip. Fracture toughness is not considered an intrinsic material property compared to modulus or yield strength; however, it does provide relative resistance to local crack propagation. The correlation between rough and surface porous polymer's capacity to maintain properties with fracture toughness suggests that the surface flaws introduced in this study may produce local stress field magnitudes that correlate to those of fracture mechanics.

To further explore the idea that the fracture toughness might control the mechanical properties of polymers and to help elucidate the understanding of PEEK's mechanical properties, fatigue tests were run on each polymer discussed above (**Figure 6.5**). In metals, the yield strength is a somewhat reliable predictor of fatigue life across diverse material chemistries (**Figure 6.9a**). In contrast, as shown in **Figure 6.9b**, the yield

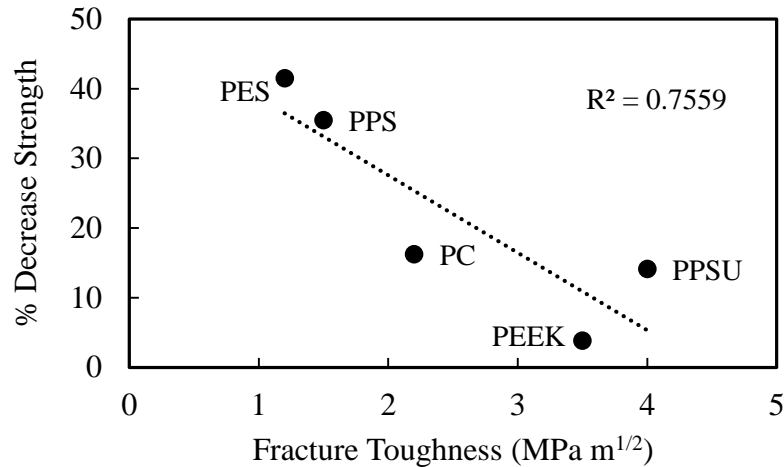
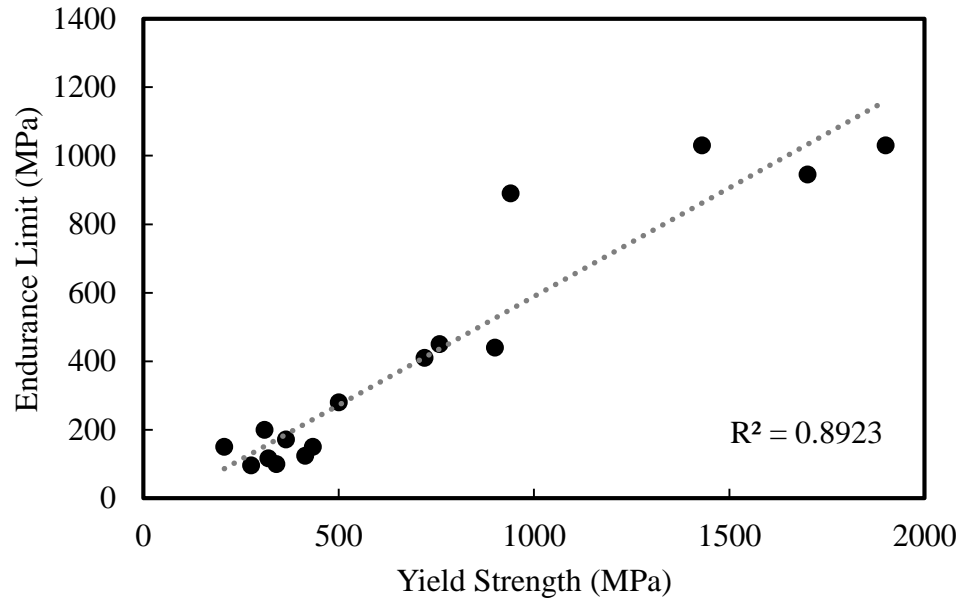


Figure 6.8. Percent decrease in strength of polymers with the creation of a surface porosity versus the fracture toughness.

strength fails to predict the fatigue strength of polymers. However, the fracture toughness shows a strong correlation with the normalized endurance limit (stress at runout/yield strength) (**Figure 6.10**). This is not surprising, as fracture toughness indicates the amount of stress required to propagate a preexisting flaw and the effect of cyclic stress is to initiate microscopic cracks at stress concentrations and subsequently enable those cracks to propagate [213]. Taken together with the findings from the surface porous samples, there appears to be a relationship between the fracture toughness of polymers and their mechanical properties in both porous and smooth states. The full extent of this relationship is not fully understood at this point, but the data here demonstrate that fracture toughness is the best predictor of the polymers fatigue strength and capacity to sustain properties with surface porosity.

(A)



(B)

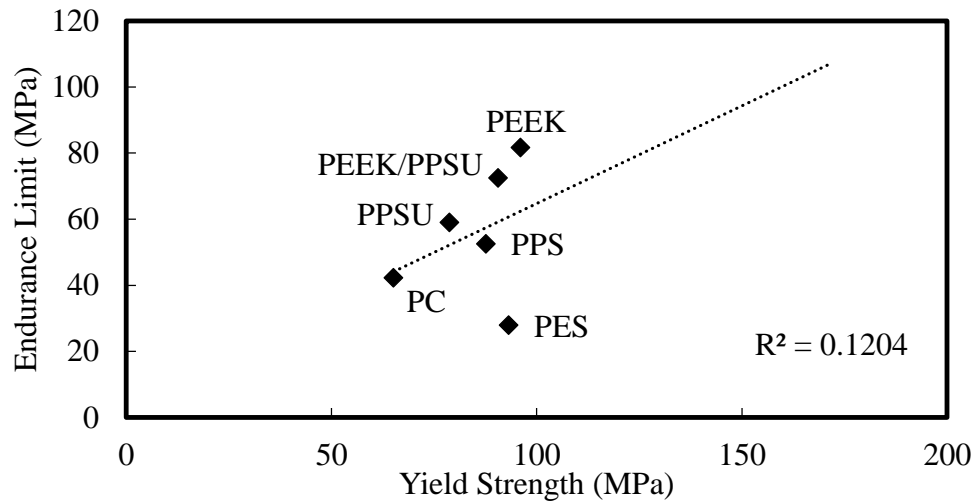


Figure 6.9. (A) Endurance limit of commercial alloys (aluminum, steel, titanium, zinc, and magnesium alloys) versus yield strength. (B) Endurance limit of the polymers used in this study versus yield strength.

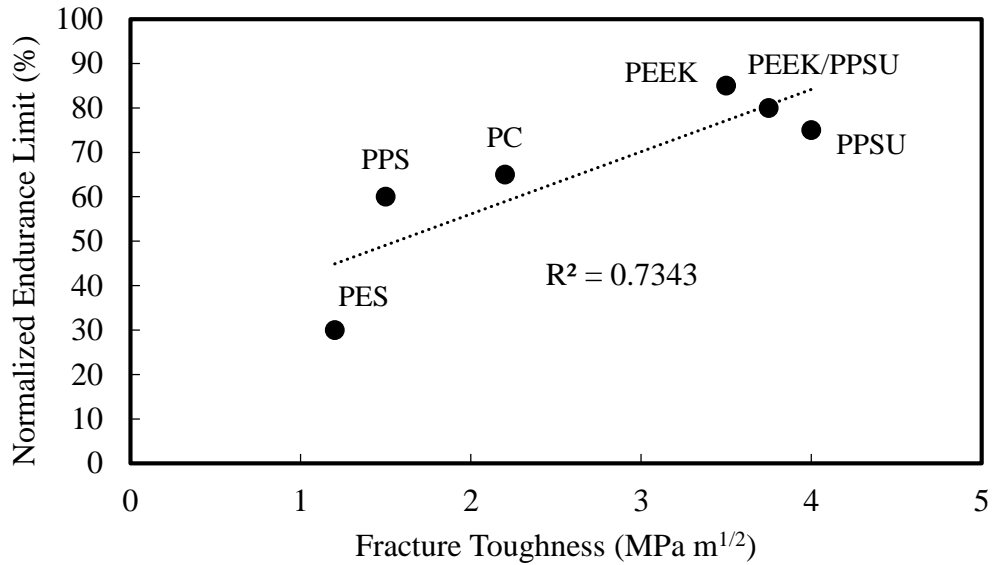


Figure 6.10. Normalized endurance limit of the polymers used in this study versus fracture toughness.

This work also characterized the fatigue life of select surface porous polymers, as fatigue is often a source of failure in orthopaedic polymeric implants due to the cyclic loading conditions in the body [158, 214]. Furthermore, since fatigue is due largely to the growth of cracks, notches, or scratches on a specimen, surface porosity may cause a great reduction in fatigue life, especially for notch-sensitive materials [192]. Tensile fatigue tests were run on surface porous PEEK, PPSU, PEEK/PPSU, and PC and compared to their injection molded counterparts. In general, the surface porosity resulted in a reduction in fatigue strength. These results are not surprising as surface flaws often lead to a detrimental decrease in the fatigue resistance of polymers provided that there are not significant internal voids or flaws [1, 40, 42]. Furthermore, the results indicate that the surface topography has a greater effect on the fatigue life than the tensile strength, in agreement with a previous study on porous polypara-phenylene scaffolds [43].

It is also of note that for many of the presented fatigue curves, two distinct failure regions occur: (I) a lower slope, linear region at lower cycle numbers demonstrating a strong dependence of cycles-to-failure on stress and (II) a region at higher cycle numbers of much higher slope demonstrating a weaker dependence of cycles-to-failure on stress. These two regions are generic responses for all polymer systems and are referred to as plasticity controlled failure (Region I) and slow crack growth (Region II) [215]. In general, the first region is characterized by ductile failure and the accumulation of large strains and is observed at high stresses and short time scales. The second region is generally characterized by brittle fracture and very little macroscopic strain and occurs at lower stresses and larger cycle numbers.

The switch in fatigue failure from plasticity-controlled to crack-growth controlled is quite evident in the S-N curves of IM PPSU, PC, PES, and PPS (**Figure 5**). In addition to the change in slope on the stress-strain curves, there was also a notable change in failure from ductile failure with significant plastic deformation to more brittle failure in these samples. The strain accumulation was also significantly decreased in Region II. Another observation of importance is the change in slope and the shift of Region II to lower cycle number in the SP samples compared to the IM samples (most notably **Figure 5b, d**). Because the transition from the first to the second regime will depend, among other factors, on the size of the initial flaw/crack that is present in the sample, this is an expected result due to the addition the porosity/flaws.

The local stress fields are not always significant enough to impact overall ductility and cause a decrease in strength, but often are significant enough to favor early fatigue crack nucleation and a drop in fatigue strength. The results demonstrate that PEEK

maintains its strength even at high cycle fatigue and has the smallest decrease in fatigue life with the addition of surface porosity. This is likely due to the semicrystalline and two-phase microstructure as represented by the high fracture toughness as described previously.

It should be noted that these results are not unique to polymers. Porous metal implants and porous-coated metallic implants have been used for decades to improve the osseointegration and fixation of implants in applications such as joint replacement [216]. Though these implants tend to be made out of high strength alloys, porosity can significantly reduce the fatigue strength of such devices. For example, the high cycle fatigue strength of porous coated Ti-6Al-4V is approximately 68-79% lower than the fatigue strength of uncoated Ti-6Al-4V due to stress concentrations at the porous coating/substrate interface and within the porous coating resulting in local stresses as high as six times the nominally applied stress [217, 218]. Porous tantalum, another clinically used material, retains only about 30% of the strength and 10% of fatigue strength of the fully dense material [219]. In fact, the fatigue strength of porous tantalum is below the fatigue strength of the PEEK-SP [134].

Additional fatigue tests were performed on transversely roughened and longitudinally roughened PEEK. As shown in **Figure 6.5**, all topographical defects decrease the fatigue life of PEEK. Consistent with the tensile data, longitudinally roughened ($\sigma_N = 76.9\text{MPa}$), transversely roughened ($\sigma_N = 75.0\text{MPa}$), and surface porous ($\sigma_N = 60.0\text{MPa}$) samples demonstrated respectively lower fatigue lives. In previous fatigue studies, transverse specimens exhibited a lower fatigue strength than longitudinal specimens [194], leading to the recommendation that, if tool or grinding marks cannot be avoided, they should run in a direction parallel to the primary loading direction [220] as is

common in fatigue test standards. It is clear that careful evaluation of the effect of the surface roughness and porosity on the fatigue properties of polymers must be undertaken as advantages offered by rough and porous implants may be offset by the fatigue-inducing effects of the surface defects themselves [32].

While it was evident that the surface topography can lead to a decrease in mechanical properties, it was important to explore whether the decreases in mechanical properties of the surface porous samples were due to the surface defects alone or also due to the thermal treatment. To answer this question, PEEK-SP samples were subjected to a quenching and annealing protocol followed by mechanical characterization. The effect of quenching and annealing on the morphology and properties of PEEK is well understood and has shown the following trends [28, 221-223]: when annealed between the glass transition temperature ($T_g = 150^\circ\text{C}$) and the melting temperature ($T_m = 343^\circ\text{C}$), crystallinity increases with annealing temperature, but is little affected by annealing time. Higher annealing temperatures, and therefore crystallinity levels, cause an increase in yield stress and modulus but a decrease in ductility, impact strength, and toughness. Quenching can lead to low levels of crystallinity and therefore a decrease in strength but an increase in toughness and ductility.

As shown in **Figure 6.6**, quenching of PEEK-SP significantly decreases the strength and the modulus as expected but, surprisingly, only slightly increases the failure strain. Subsequent annealing after quenching increases the strength and modulus with no significant change in ductility. Taken together, the results indicate that the loss of ductility with the creation of a surface porosity is due to the stress concentrations from the pores and not as a result of thermal processing or crystallinity changes. In contrast, the drop in

yield strength caused by porosity is explained mainly by the sample's loss of cross sectional bearing-area and not stress concentration effects as demonstrated by the high strength calculated when using A_{LB} compared to the large decrease in strength when calculate using A_T and corroborated by the quenching and annealing data. This in agreement with previous studies in which the reduction in load-bearing area was found to have a more fundamental correlation with a loss in mechanical properties than the effect of stress concentrations [224-226]. Though stress concentration effects are complex, their effects may be approximated by minimum load-bearing areas [227].

While we recognize that in most orthopaedic applications the implant will not be under tensile loading, it was important to explore the tensile response, as surface defects are more detrimental under tensile stress than compressive stress. For example, a porous scaffold can be plastic in compression but brittle in tension, caused by the stress-concentrating effect of a crack, which leads to fast fracture in tension [228]. We therefore choose to probe the effects of topography on the mechanical properties of polymeric biomaterials in the most severe application. However, **Chapter 7** will seek to explore the effect of surface topography on the compressive response of these materials. In particular, the compressive yield strength of the porous layer will be explored and future work will seek to study the compressive fatigue response of the material. Together these studies aim to definitely determine whether surface porous polymers, and surface porous PEEK in particular, are viable materials for orthopaedic applications.

6.5. Conclusion

This study characterized the effects of surface roughness and porosity on the mechanical behavior of high strength polymers. The materials investigated represented a wide range of chemistries and structure. These results illustrate that care must be taken in the design of polymeric implants, especially when introducing topographical changes to promote osseointegration, to ensure they maintain adequate load-bearing capacity. The following observations have been made:

- (1) Surface roughness in the direction perpendicular to the applied load had a greater effect on the strength and ductility than surface roughness in the longitudinal direction but less of an effect than surface porosity.
- (2) The greatest effect of notches on the stress-strain response is the severe decrease in elongation to break and toughness, with much less of an effect on yield strength. The fatigue strength is more notch-sensitive than the tensile strength.
- (3) The fracture toughness of polymers strongly correlates to both the decrease in strength with the addition of surface porosity and the fatigue strength and is thereby a predictor of the mechanical behavior across the range of high strength polymers considered here.
- (4) Polymer structure impacted the materials relative capacity to maintain monotonic and cyclic materials properties in the face of surface roughness and porosity. Generally, amorphous polymers with large ratios of upper and lower yield points demonstrated a more significant drop in ductility and fatigue strength with the introduction of porosity compared to crystalline polymers with smaller ratios in their upper and lower yield strength

CHAPTER 7

MECHANICAL PROPERTIES OF THE SURFACE POROUS LAYER OF PEEK-SP

7.1. Introduction

Surface porous polyetheretherketone (PEEK-SP) has significant potential in orthopaedic applications due to its favorable bulk mechanical properties and its promising *in vitro* and *in vivo* results [134], but the mechanics of the porous region itself are not well understood. Due to the nature of the loading on many orthopaedic implants, it is critical to consider the compressive, shear, and wear resistance of PEEK-SP.

The evaluation of the compressive properties of PEEK-SP is important as many implants are subject to compressive loading *in vivo*. For example, the human spine is subjected to large compressive loads during daily activities. During standing or walking the compressive load reaches 1000 N [162] and is much higher during activities such as lifting [161, 229]. After interbody fusion of the spine, much of this load is transferred through the inserted cage until the space is bridged with new bone. In the knee, biomechanical studies of the joint during loading have consistently estimated maximum joint compressive forces to be about 4 to 4.5 times bodyweight during daily activities but can be as high as 8 times bodyweight during downhill walking [230]. Because the tibiofemoral contact area of most total knee designs is 100 to 300 mm², these implants will be under significant stress. From these two examples, it is clear that careful consideration of the compressive properties of PEEK-SP must be undertaken to understand how the material will perform *in vivo*. Furthermore, many applications of medical devices subject the implant to shear loading [231]. Though we previously tested the interfacial shear

strength of PEEK-SP, it is important to consider the shear strength within the porous network itself.

The abrasion resistance of PEEK-SP is also critical. Since the 1980s, PEEK and its composites have been evaluated as candidates for bearing materials in joint replacements, particularly as a replacement for ultra-high molecular weight polyethylene (UHMWPE) [232]. Most studies have considered the use of carbon fiber reinforced (CRF) PEEK due to its superior wear resistance than neat PEEK. Studies have shown that the CFR-PEEK offers a far superior wear resistance over UHMWPE against either metal or ceramic couples [233]. Work investigating use of a CFR-PEEK acetabular cup against alumina femoral heads demonstrated that such wear couples approach the bearing performance of hard-on-hard surfaces [234]. A thorough examination has also been given to the bioactivity of wear particles produced from PEEK devices. Multiple studies evaluated the cytotoxicity of wear debris from CFR-PEEK devices *in vitro* and found no cytotoxic or mutagenic potential [235, 236] although fibroblast attachment to particles was greater than UHMWPE [237]. The *in vivo* response has also been characterized. CFR PEEK wear particles injected into the knees of mice showed comparable biological activity to UHMWPE particles [238] and PEEK particles injected into the spinal canal of rabbits proved harmless to the spinal cord and nerve roots [239]. In non-articulating applications, micromotion at the bone-implant interface can cause the formation of wear debris which can lead to an inflammatory response and bone resorption [240, 241]. The ASTM testing standard for medical device coatings highlights that particle shedding might occur during surgical insertion of an implant or as the result of micromotion of the implant after insertion [242].

Despite the low risk of PEEK debris, it is nevertheless important to consider the wear and abrasion resistance of PEEK-SP. It is generally agreed that porosity is detrimental to the wear resistance of materials, though some experiments show exceptions [243]. Porosity increases the surface roughness of materials, decreases the real area of contact between two sliding surfaces, and consequently increases the contact pressure which promotes material removal during sliding [244]. The wear rate has been shown to increase with increasing porosity and the improvement of the tribological properties of some coatings is becoming the actual goal of achieving the minimum porosity coatings [245, 246].

The focus of this Chapter is to study the mechanics of the porous layer relevant to orthopaedic applications. Compression testing provided understanding of the strength and stiffness of the porous layer decoupled from the underlying solid PEEK. Microcomputed tomography scans (μ CT) of the surface porous layer at various compressed states were used to understand the pore layer deformation mechanisms. The μ CT studies revealed the bending, buckling, and collapse of cells with increasing compression, consistent with previous experimental results [247] and numerical simulations on polymer foams [248]. Abrasion testing demonstrated that the wear rate of PEEK-SP is not higher than injection molded PEEK (PEEK-IM) due to a difference in wear mechanism. The results presented here are important in the future design and use of PEEK-SP implants.

7.2. Materials and Methods

Samples of various layer thicknesses and porosities were manufactured and analyzing using μ CT according to the methods outlined in **Chapter 3**. Specifically, the

abrasion samples were manufactured using the oven method; all other samples were processed on the hot plate. To probe the mechanics of the pore layer, monotonic compression, *in situ* μ CT compression, shear, and abrasion tests were performed as described in **Chapter 3**.

7.3. Results

7.3.1. Pore morphometry characterization

The average layer thickness and percent porosity of the compression samples is shown in **Table 1**. No difference in pore sizes or strut spacing were measured from those reported in **Chapter 5** (pore size: SP-250 = $284 \pm 35 \mu\text{m}$, SP-350 = $341 \pm 49 \mu\text{m}$, SP-450 = $416 \pm 54 \mu\text{m}$).

Table 7.1. Pore morphology of PEEK-SP samples used in compression testing.

	Thin Pore Layer		Thick Pore Layer	
	Pore Layer Thickness (mm)	% Porosity	Pore Layer Thickness (mm)	% Porosity
SP-250	0.918 ± 0.22	68.1 ± 2.3	2.25 ± 0.093	72.7 ± 1.9
SP-350	1.40 ± 0.089	71.3 ± 0.19	2.73 ± 0.053	75.4 ± 2.9
SP-450	1.09 ± 0.071	70.8 ± 1.5	2.19 ± 0.21	72.1 ± 1.8

7.3.2. Compression Testing

Average yield stresses and moduli values are summarized for all samples in **Table 7.2**. No significant differences were found between pore sizes but the thinner pore layer demonstrated a higher modulus and yield strength ($p < 0.000001$ and $p < 0.00001$, respectively). Representative stress-strain responses of PEEK-SP are shown in **Figure 7.1**. As demonstrated, the PEEK-SP curve can be decoupled into the solid and porous components. The pore layer shows the typical three stage response of porous materials:

linear elasticity, plastic deformation, and densification (**Figure 7.2**). After densification, the fully dense material behaves as the solid and closely parallels the solid stress-strain response.

Table 7.2. Modulus and yield strength of the PEEK-SP samples tested in this study. Values represent the average \pm one standard deviation.

	Thin Pore Layer		Thick Pore Layer	
	Modulus (MPa)	Offset Yield (MPa)	Modulus (MPa)	Offset Yield (MPa)
SP-250	110 \pm 12	11.7 \pm 0.73	60.8 \pm 7.6	4.48 \pm 0.76
SP-350	109 \pm 18	7.17 \pm 0.52	61.8 \pm 6.8	4.33 \pm 0.63
SP-450	90.7 \pm 9.2	10.6 \pm 0.76	52.5 \pm 8.1	4.51 \pm 0.67

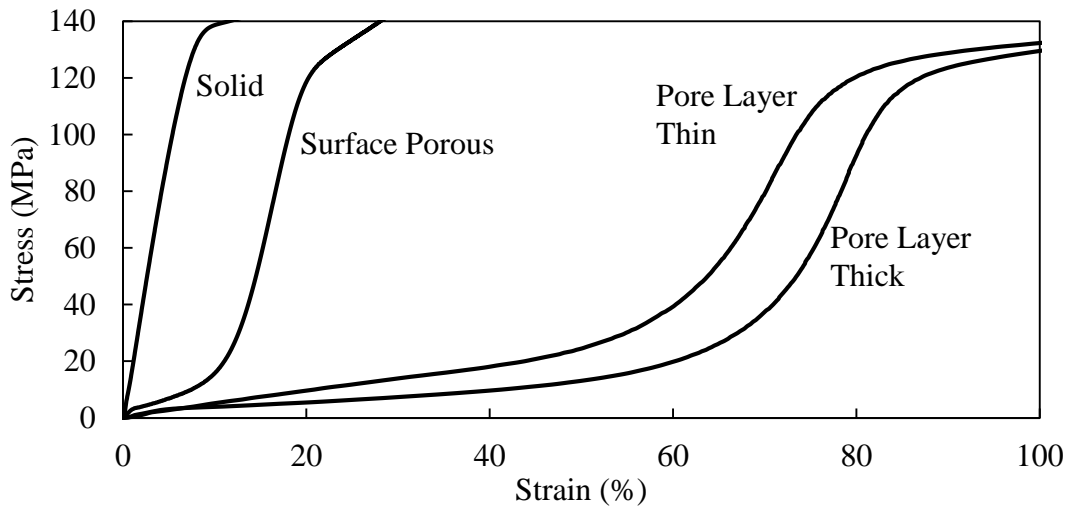


Figure 7.1. Stress-strain response of PEEK-SP-350 relative to the response of just the solid and pore layer components only.

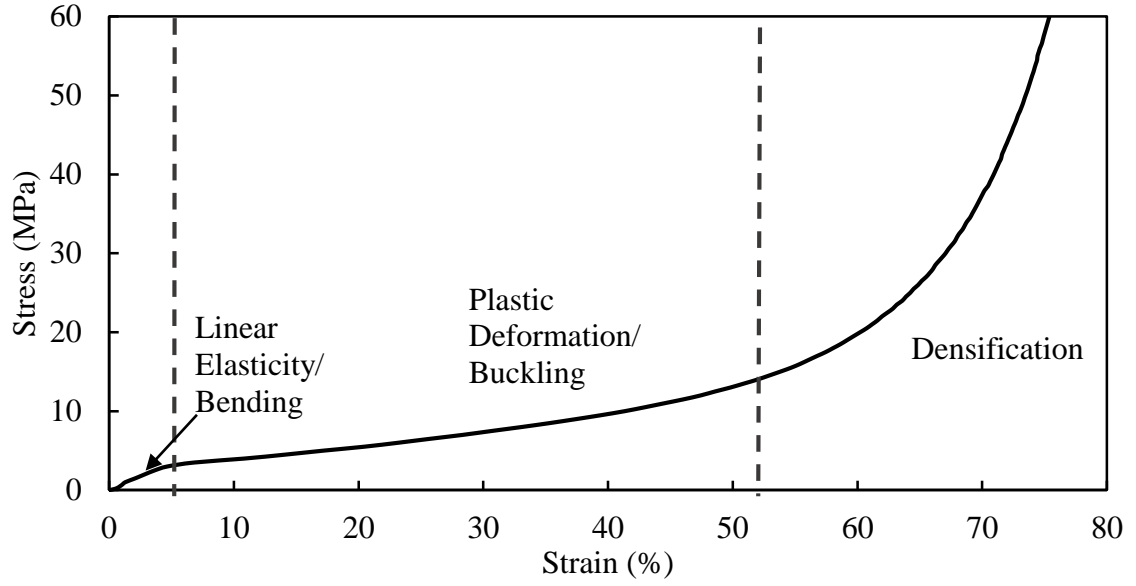


Figure 7.2. Stress-strain behavior of the pore layer isolated from the stress-strain response of PEEK-SP. The response demonstrates the typical three staged response of porous foam materials: linear elasticity (i.e. bending), plastic yielding (i.e. buckling), and densification.

Figure 7.3a compares the experimentally measured modulus of the samples to the theoretical modulus predicted by **Equation 1**

$$E^* = E_s(1 - V_f)^2 \quad (1)$$

where E^* and E_s are the elastic moduli of the porous materials and the material without porosity, respectively, and V_f is the pore volume fraction [249]. The experimental moduli were lower than the theoretical values, regardless of pore size or pore layer thickness.

Figure 7.3b compares the experimental compressive yield strength to the theoretical yield strength predicted by Gibson and Ashby's model for strength of open-cell foams in **Equation 2**

$$\sigma_y^* = 0.23\sigma_y(1 - V_f)^{3/2} \left[1 + (1 - V_f)^{1/2} \right] \quad (2)$$

where σ_y^* is the yield strength of the foam and σ_y is the yield strength of the solid material [150]. **Equation 2** is only applicable for $70\% \leq V_f \leq 96\%$. In general, the experimental

yield strength of samples with the thinner pore layer were greater than the theoretical, regardless of pore size, and the samples with the thicker pore layer were below the experimental.

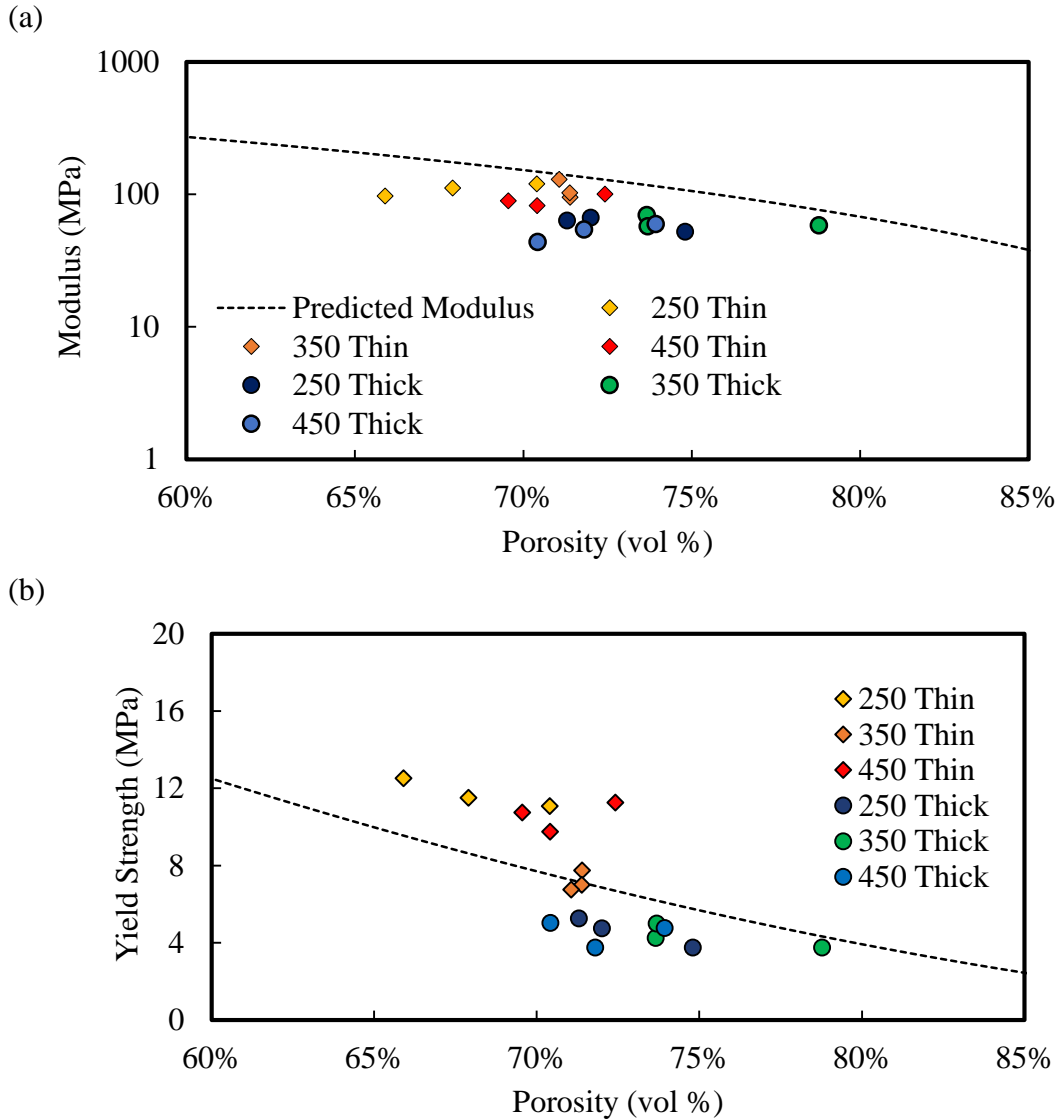


Figure 7.3. (a) Experimental modulus of PEEK-SP samples compared to the theoretical modulus predicted by Equation 1. (b) Experimental yield strength of PEEK-SP samples compared to the theoretical yield strength predicted by Equation 2.

7.3.3. μ CT Compression

The *in situ* μ CT compression testing (n=3) revealed that the percent porosity and strut spacing decreased as a function of strain (**Figure 7.4**). The data also demonstrates good agreement with the prior compression results. **Figure 7.5** shows representative μ CT reconstructions of the sample at various strains. Pore morphometrics were also evaluated as a function of various regions of sample 1. The sample was divided into three regions: the bottom 1/3 of the sample near the solid-pore interface, the middle 1/3 of pore layer, and the top 1/3 of pore layer at air-pore interface. The results (**Figure 7.6**) demonstrate uniform deformation throughout the sample.

(a)

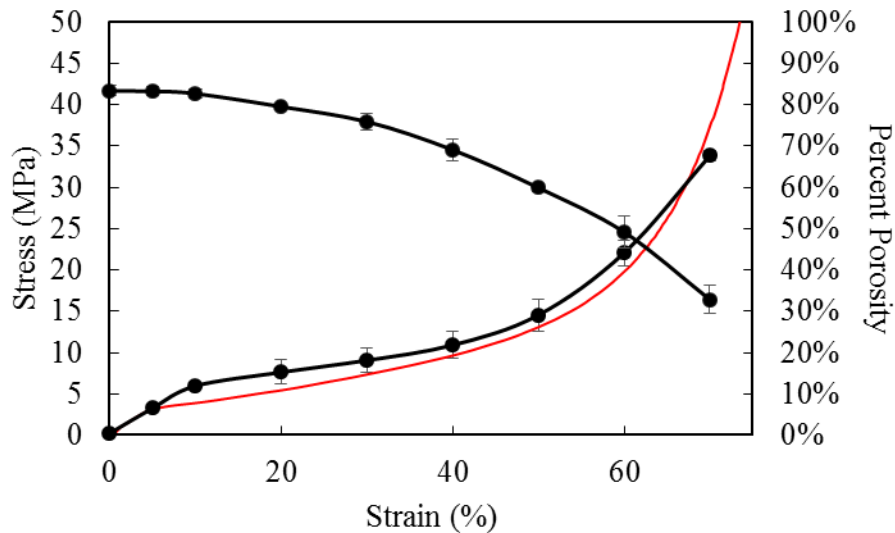


Figure 7.4. Microstructural response of PEEK-SP to deformation. (a) Plot of average percent porosity versus strain with the stress-strain plot included for comparison. The red line is a representative stress-strain curve from **Figure 7.1** demonstrating good agreement between the two tests. Error bars represent \pm one standard deviation. (b) Plot of average strut spacing versus strain \pm one standard deviation.

(b)

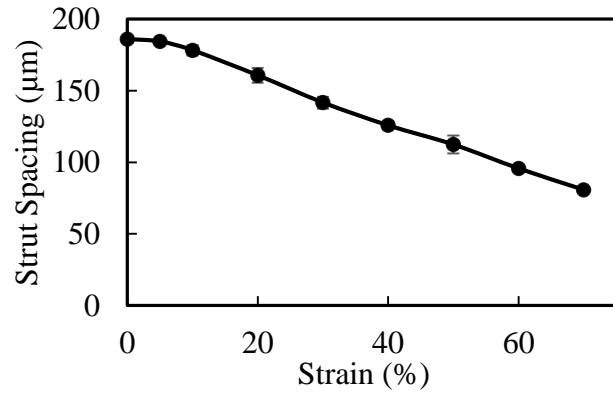


Figure 7.4. Continued.

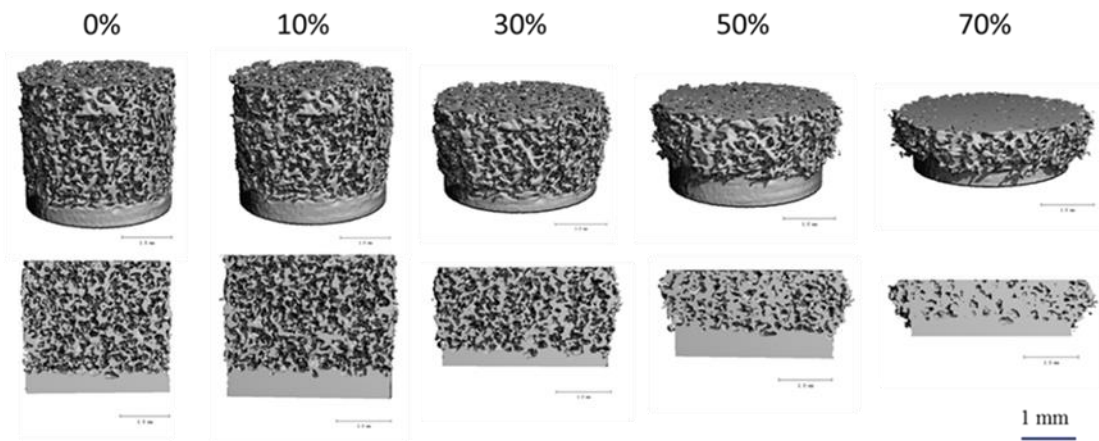


Figure 7.5. μ CT reconstructions of the porous layer at various strains.

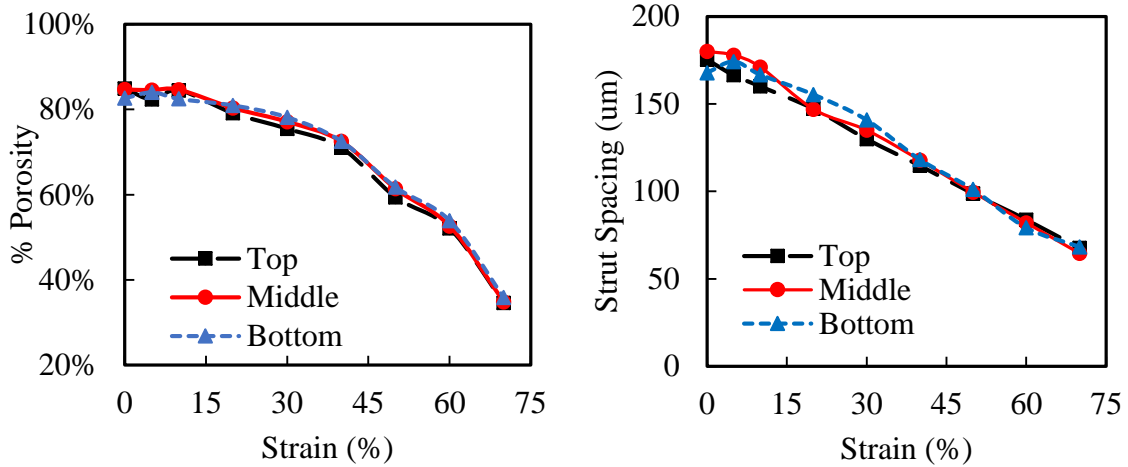


Figure 7.6. Characterization of the pore structure as a function of deformation in three regions of a representative sample: bottom 1/3 of pore layer at the pore-solid interface, middle 1/3 of pore layer, and top 1/3 of pore layer at pore-air interface. (a) Percent porosity as a function of strain. (b) Strut spacing as a function of strain.

7.3.4. Shear Testing

The shear strength and modulus of fully porous samples with two different percent porosities is shown in **Table 3**. The samples with lower porosity had significantly higher strengths and moduli ($p < 0.01$).

Table 7.3. Shear strength and modulus of fully porous samples with two different percent porosities.

	Strength	Modulus	Porosity
n = 5	7.69 ± 1.6	20.1 ± 6.3	$83 \pm 2 \%$
n = 2	11.6 ± 0.03	52.1 ± 11	$76 \pm 2 \%$

7.3.5. Taber Abrasion Test

Average mass loss values after 100 cycles are summarized in **Table 7.4**. No significant differences were found between any of the samples. Representative before and after 100 cycles of abrasion are shown in **Figure 7.7**. Optical microscopy revealed some

particulate from the wheel stuck in the pore network of the SP samples. μ CT reconstructions comparing the pore structure before and after abrasion revealed a collapsed pore network (**Figure 7.8**) instead of particle shedding. μ CT analysis also demonstrated a reduced layer thickness for PEEK-SP-250 abraded compared to non-abraded samples ($0.645 \pm 0.051 \mu\text{m}$ vs $0.684 \pm 0.053 \mu\text{m}$, respectively, $p < 0.05$). No difference in layer thickness was found between abraded and non-abraded samples in the 350 or 450 groups. A change in strut spacing was also observed for PEEK-SP-250 abraded compared to non-abraded samples ($149 \pm 2.3 \mu\text{m}$ vs $156 \pm 0.55 \mu\text{m}$, respectively, $p < 0.05$) and for 350 abraded compared to non-abraded ($226 \pm 3.6 \mu\text{m}$ vs $232 \pm 2.7 \mu\text{m}$, respectively, $p < 0.05$). No change in strut spacing between 450 groups was observed.

Table 7.4. Measured mass loss after 100 cycles. No significant differences were found between any of the samples.

Sample	Mass Loss (mg)
SP 250	31.4 ± 9.2
SP 350	27.6 ± 12.3
SP 450	29.0 ± 3.3
IM	39.0 ± 18

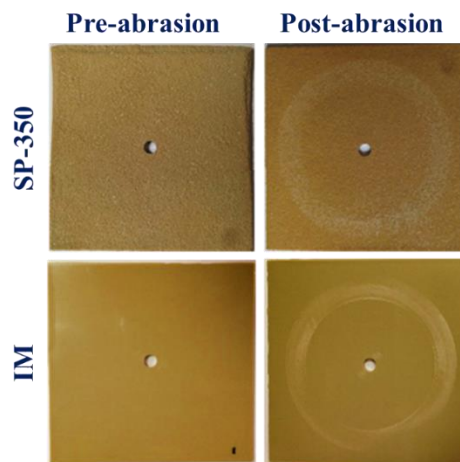


Figure 7.7. Images of the surface before and after abrasion. (a) Pictures of the surface before and after abrasion.

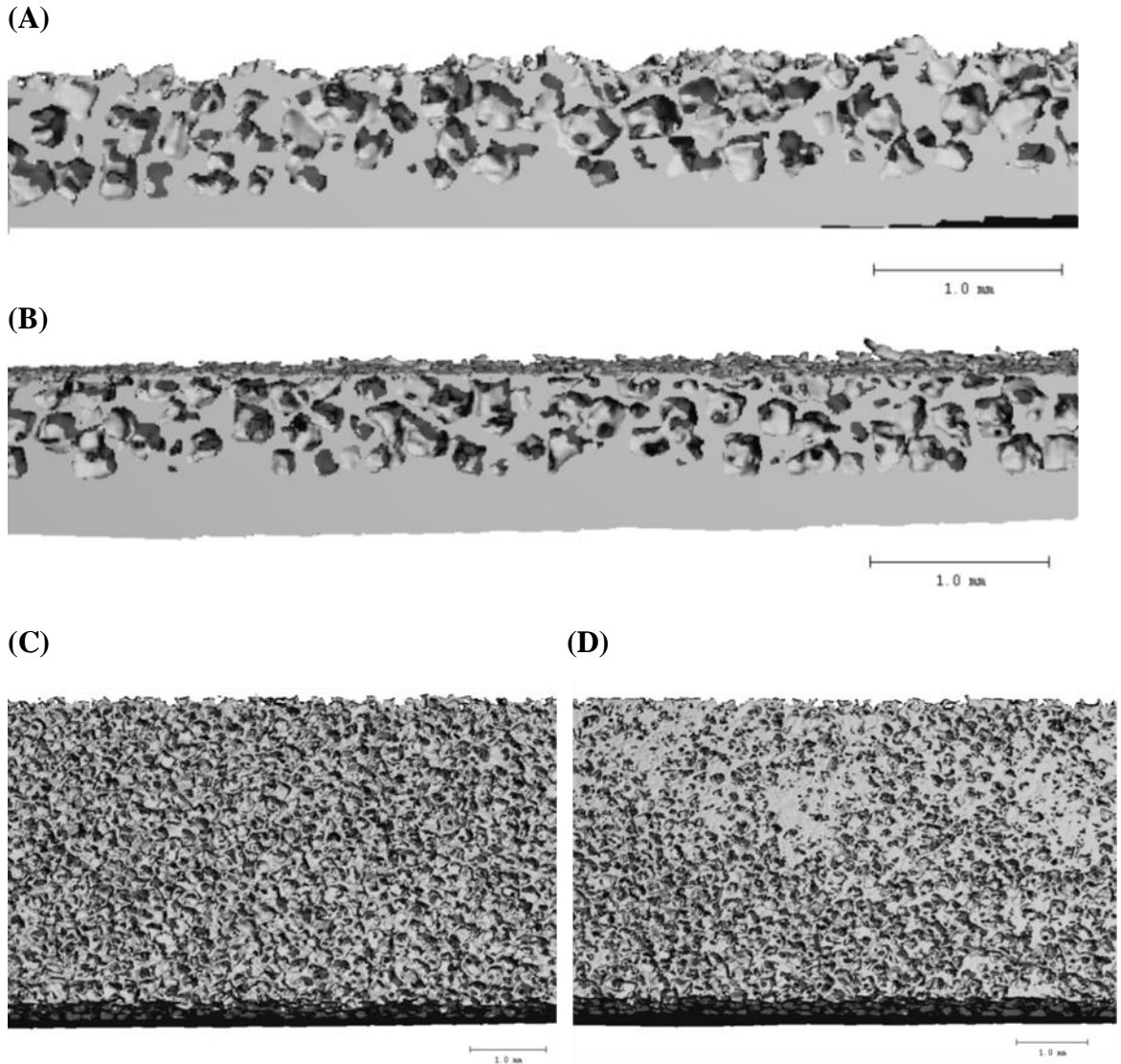


Figure 7.8. Representative μ CT reconstructions of surfaces before and after abrasion. (A) Cross-section of PEEK-SP-250 pre-abrasion. (B) PEEK-SP-250 post-abrasion. (C) Surface of PEEK-SP-250 pre-abrasion. (D) Surface of PEEK-SP-250 post-abrasion.

7.4. Discussion

While previous Chapters characterized the bulk mechanical properties of PEEK-SP [134] and the mechanics of solid PEEK are well known [250], mechanical properties of the pore layer relevant to many load-bearing orthopaedic applications have not been evaluated. In this Chapter we evaluated the compressive, shear, and wear properties of PEEK-SP to provide understanding of the structure-property relationship and to inform future design of implants incorporating this technology.

Compression testing of PEEK-SP demonstrated three stages of deformation in the surface porous layer – bending, buckling, and densification – regardless of pore size or layer thickness. This deformation behavior is characteristic of foams and has been described previously [247, 248]. It is therefore helpful to consider PEEK-SP as a composite material consisting of a solid PEEK core and an outer PEEK foam. Foams generally have reduced mechanical stiffness and strength but enhanced compressibility [247] and can accommodate large strains.

In the initial regime of deformation, the cell wall ‘struts’ undergo elastic deformation and uniaxially bend corresponding to a small drop in pore size. The elastic regime of PEEK-SP occurs below ~5% strain. With increasing deformation up to ~50% strain, the struts buckle and the material experiences plastic flow. The free volume inherent due to the porosity leads to cell collapse and results in a rapid drop in the average cell size over the strain corresponding to the plastic regime (**Figure 7.4**). The increase in axial strain takes place without a significant increase in transverse strain, highlighting the unique relationship between axial and transverse strains (Poisson effect) for foams [247]. The transverse strain becomes significant once the foam reaches the densification stage. Once

all struts have buckled, densification occurs (>50% strain) and the change in cell size slows. Upon densification the material approaches the stress-strain response of the solid material (**Figure 7.1**).

All samples demonstrated similar stress-strain responses and there was no observed difference in pore size. This is in agreement with previous studies on porous polymers showed that the percent porosity has a much bigger influence on properties than pore size [100]. While pore size shows little effect, the compressive response was significantly different for the two layer thicknesses. The variation in strength and stiffness with layer thickness is primarily due to the fact that as the layer thickness increased, the porosity increased. This can be explained by the following: to create thicker porous layers, the PEEK had to be pressed greater distances through the salt network. These greater distances required a higher force resulting in greater packing of the salt and subsequently a higher percent porosity. This relationship between layer thickness and percent porosity of the compression samples is highlighted in **Figure 7.9**. It is envisioned that thin pore layers could be processed with higher porosity by pre-compressing the salt layer used in the sample processing. However, future work is needed to explore ways to create thick pore layers with lower porosity using the same processing method.

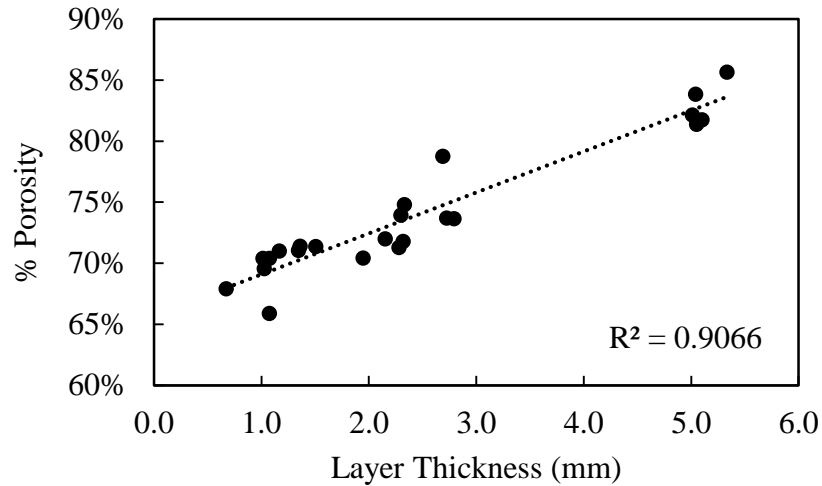


Figure 7.9. Relationship between the percent porosity and the pore layer thickness.

The compression tests demonstrated that PEEK-SP is much more ductile but yields at lower stresses than when tested in tension [134]. The pores allow for large strains in compression while initiating cracks in tension that significantly decrease the ductility. In contrast, when comparing strengths, compressive forces yield the pores at relatively low loads while in tension the solid core is able to carry the majority of the load. These results are clearly dependent on the fact that in compression the pore layer and solid region were tested in series; tension tests evaluated the pore layer and solid region in parallel. It is hypothesized that compressive testing of the pore layer and solid region in parallel would result in a much higher yield strength with lower corresponding strains. Furthermore, tensile testing of the pore layer and solid region in series would result in much lower yield strengths and would either give the tensile strength of the pore layer or the tensile strength at the interface (tensile adhesion test, ASTM F1147-05). These results are important to consider when evaluating PEEK-SP as a potential material in load-bearing orthopedic applications.

Although the differential porosities explain most of the observed compression results, it is important to note that the yield strength of thin pore layers lie, in general, above the theoretically predicted yield strength and the yield strength of the thick layers lie below. These observed differences could be due to the effects of the substrate. Structural support of the underlying substrate might lead to greater measured strengths in the thinner pore layers; in the thicker pore layers, this effect would most likely be negligible. Substrate effects, commonly studied in thin films [251-256], can be due to different microstructures near the interface or due to the constraint of the substrate on the films deformation mechanism. To evaluate whether there existed different microstructure in the various layers, the percent porosity as a function of the normalized pore layer depth for the thinnest and thickest pore layers studied in the monotonic compression were plotted in **Figure 7.10**. As shown, the thin layer not only has a lower porosity throughout the pore layer, but the transition to the solid (the interface thickness) is a much greater percent of the overall pore layer thickness. Therefore, the less porous microstructure near the interface, in combination with the lower overall porosity, leads to an increase in the observed yield strength.

The *in situ* μ CT compression scans provided further insight into deformation of the pore layer. The data demonstrated very good agreement between the pore morphometrics of all three samples indicating that the PEEK-SP structure created is very consistent with high reproducibility. The results also showed uniform deformation throughout the sample (Figure 7.7). Importantly, the μ CT compression data reveals that the sample can deform up to 50% of its original size and still offer high porosity for ingrowth (over 60% porous, or 70% of the original open space). The stress at 50% strain is around 14 MPa. This indicates that in an application such as lumbar spinal fusion, where the average cage is

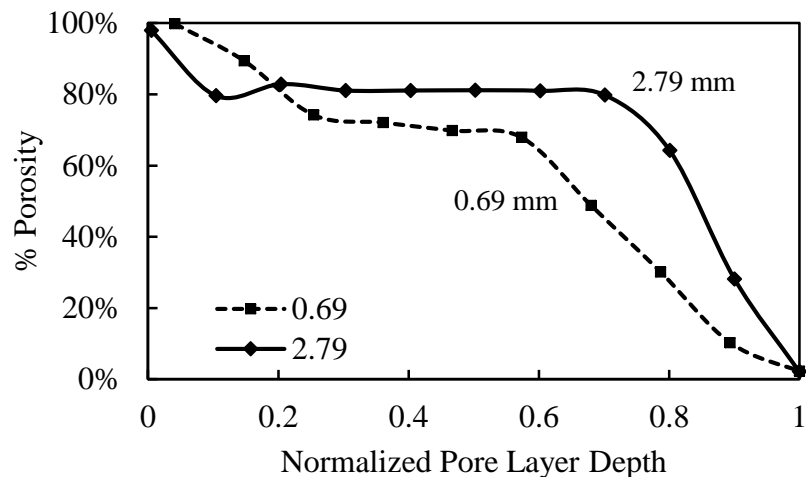


Figure 7.10. Percent porosity as a function of normalized pore depth for the thinnest pore layer (0.69 mm) and thickest pore layer (2.79 mm).

between 90 and 330 mm², a surface porous PEEK implant could withstand a minimum of 1260 N and as much as 4620 N of load while still offering high porosity for ingrowth. These loads are above those commonly placed on the spine during daily activities [257].

Abrasion on PEEK-SP and PEEK-IM yielded unexpected results. While porous samples were expected to wear at a higher rate than their smooth counterparts, no differences in the mass loss was observed between surface porous PEEK samples and IM PEEK. Although the coefficient of friction on PEEK-SP samples is undoubtedly higher, visual inspection and μ CT analysis revealed a difference in wear mechanism. The normal mechanism of wear in this test setup is particle shedding. However, the main mechanism for the SP groups appears to be flattening of the top pore layer due to shearing and compressive loads and slight densification of the pores (**Figure 7.8**). It is hypothesized that after the top pore layer has been totally flattened and smoothed along the wear path, resulting in a more uniform surface, the SP surfaces behaves similarly to the IM samples resulting in similar mass loss.

It is important to note that, despite use of the vacuum during abrasion and numerous rounds of sonication (>10 per sample), observation of the samples under a microscope revealed ceramic wheel particles trapped in the deformed pore layer. These trapped particles are not soluble so extended cycles of sonicating failed to remove them from the pores. To provide insight into whether trapped particles were the cause for the lower than expected wear on SP samples, one of the trapped particles was removed and weighed. The scale, with a 0.1mg resolution, failed to register the mass of the particle indicating there would have to be an enormous number of such particles to change the mass in any significant way. It is also possible that PEEK wear particles became stuck in the pore network. However, the results indicate that the primary explanation for the lack of difference in SP and IM wear is due to differing wear mechanisms.

This Chapter provides insight into the deformation mechanics of the porous layer on PEEK-SP and demonstrates that the material is suitable for load bearing applications such as spinal fusion. PEEK-SP exhibited the ability to withstand physiologically relevant loads while still maintaining a high degree of porosity available for bone-ingrowth. Furthermore, no increase in wear was observed on surface porous samples. While future work is needed to explore the time-dependent deformation (creep) and cyclic compression resistance, the results thus far are promising for future applications of the material in orthopaedics.

7.5. Conclusions

This study probed the mechanics of the pore layer of surface porous PEEK and the following observations have been made:

- (1) The compressive response of PEEK-SP is characterized by three stages – linear elasticity (bending), plastic deformation (buckling), and densification – as predicted by numerical models of foam deformation.
- (2) Pore size has no effect on any of the measured mechanical properties.
- (3) The overall percent porosity correlates to changes in layer thickness due to the higher pressure used during processing of thicker pore layers.
- (4) Variations in porosity drive the observed differences in strength and stiffness.
- (5) There was no observed increase in mass loss during abrasion on surface porous samples; the mechanism of wear on smooth samples was particle shedding but was pore layer collapse on porous surfaces.
- (6) PEEK-SP can withstand physiologically relevant loads while still maintaining a high degree of porosity available for bone-ingrowth.

CHAPTER 8

CONCLUSIONS

This work was the first to create and examine surface porous polymer technology for orthopaedic applications. The need for such a technology is evident as the use of polymers in orthopaedics is steadily increasing. In some markets, such as spinal fusion and soft tissue anchors, polyetheretherketone (PEEK) is already the material of choice in the majority of implants. In other applications, such as craniofacial, dental, and total joint replacements, the possibility of using PEEK and other polymers as replacements for metallic implants has begun to be explored. Despite PEEK's widespread use, it is often associated with poor osseointegration which can lead to implant loosening and ultimately failure of the device. Many attempts have been explored to improve the osseointegration of PEEK but none have had widespread clinical success. However, the surface porous PEEK (PEEK-SP) technology developed in this work demonstrates an improved cellular response with bone ingrowth while providing a structure with mechanical properties capable of withstanding the loads in common orthopaedic applications.

The overall goal of this research was to create a thin porous surface layer on a solid PEEK device to improve the integration of PEEK implants with the surrounding bone while maintaining the structural integrity necessary for load-bearing applications. It was first demonstrated that a melt extrusion and porogen leaching process could be used to create a novel PEEK-SP structure. The pore microstructure was reliably controlled via careful processing. The key processing variables – porogen size, time, temperature, pressure, and flow displacement – were tuned to control the percent porosity, pore size, and pore layer depth. Though a wide range of pore sizes are feasible with this process, samples with 200-

500 μ m pores were created as they have previously been demonstrated to be optimal for bone ingrowth. The layer thickness was varied from only 200 μ m thick – a single pore layer – to over 6000 μ m thick. The percent porosity was between 60-85% as determined by the random packing of cubes and the force used to push the polymer into the salt layer. This volume fraction is also optimal for the intended application, though it is envisioned that a wider range of porosities are achievable using different mixtures of porogen sizes. In addition, samples were created with bimodal pore sizes, gradients in pore sizes, and with hydroxyapatite particles mixed in to form a composite material. Many other microstructures are possible opening up a wide range of potential applications.

Preliminary *in vitro* data showed that PEEK-SP supported greater proliferation and cell-mediated mineralization (calcium deposition) compared to smooth PEEK and Ti6Al4V, suggesting enhanced differentiation. These results were independent of pore size and suggested the ability of PEEK-SP to facilitate bone ingrowth and improve the integration of the implant. To confirm this potential, implants with one surface porous face were placed into critically sized defects in a rat femoral segmental defect model. Histological examination and μ CT analysis provided evidence of bone ingrowth as early as 6 weeks. The degree of fibrous encapsulation in and around the porous surface was greatly reduced in comparison to the control (smooth PEEK) surfaces. Furthermore, the morphology of the ingrown bone was cubic in nature, suggesting complete growth into the cubic pores. Despite the promising results, more work is needed to determine the strength of the bone-implant interface.

Mechanical tests were performed on PEEK-SP to determine the effect of the surface porosity on its ability to carry load and maintain the structural integrity necessary in

complex loading environments. Tensile tests showed that the surface porous processing had no effect on the modulus, resulted in a minimal decrease in load carrying capacity, but decreased the failure strain by ~50%. While the maximum force the polymer was able to sustain was only slightly decreased, the area was increased due to the void volume and therefore the strength calculated using the total cross-sectional area was decreased. To explore whether the loss in ductility was due to the stress concentrations from the pores or from the thermal treatment, PEEK-SP samples were subjected to a quenching and annealing protocol followed by mechanical characterization. The results indicated that the loss of ductility with the creation of a surface porosity is due to the stress concentrations from the pores and not as a result of thermal processing or crystallinity changes. PEEK-SP also preserved 73% of the fatigue resistance of injection-molded PEEK.

Further testing probed the mechanics of the pore layer itself to determine the durability and strength of the pore layer. Interfacial shear testing showed the pore layer shear strength to be greater than 23MPa, notably higher than trabecular bone which implies that failure will originate from bone itself and not the solid-porous interface even when high-quality bone has fully integrated. Abrasion testing demonstrated that PEEK-SP did not wear at a higher rate than injection molded PEEK. Despite a higher roughness and coefficient of friction, the pore layer was deformed and the pores collapsed with no increase in particle shedding. Compression testing confirmed that the pore layer behaves in the typical three stage response of porous materials: linear elasticity, plastic deformation, and densification. After densification, the fully dense material behaves as the solid and closely parallels the solid material's stress-strain response. *In situ* μ CT compression revealed that the sample can deform up to 50% of its original size and still offer high porosity for

ingrowth (over 60% porous, or 70% of the original open space). In all mechanical testing, pore size was found to have no effect.

This work also looked more broadly at the effect of topography and surface porosity on the mechanical properties of polymers. The surface porous process was applied to a range of thermoplastics and the properties were compared to injection molded and surface roughened polymers. It was demonstrated that the pores have a greater notch effect than surface roughness and that all polymers tested were notch sensitive. The data showed that the greatest effect of notches is the decrease in failure strain and toughness with less of an effect on strength. Fatigue testing of surface porous polymers demonstrated that fatigue strength is more notch sensitive than the tensile strength. Despite similar trends across all the polymers, there was great variation in the notch sensitivity of the polymers that correlated to their respective fracture toughness.

To provide understanding of the roughened and surface porous results, the link between polymer structure and the capacity to maintain mechanical properties with notches was examined. Amorphous polymers with large ratios of upper to lower yield points demonstrated a more significant drop in properties while crystalline polymers with small differences in upper to lower yield points maintained their strength and ductility to a greater degree. In both cases of surface roughness and surface porosity, PEEK maintained the best combination of strength and ductility, providing further evidence as it being a material of choice in orthopaedic load bearing applications.

This thesis has a few limitations. All mechanical testing was performed in air at room temperature. Despite PEEK's mechanical properties being relatively insensitive over the room temperature to body temperature range and its extremely stable structure

providing no cause for concern in the harsh environment of the body, more physiologically relevant tests would be useful in understanding how the material would behave in clinical applications. In addition, some relevant mechanical properties remain to be studied, namely the compressive fatigue and creep response of the surface porous material. Furthermore, the range of pore sizes studied was fairly small. Much smaller and larger pores might result in observed differences in both the mechanical properties of the material as well as the biological response. Finally, we have yet to systematically separate out the effects of chemistry and topography in our *in vitro* studies.

Therefore, future development of the surface porous technology should focus on four key areas: (1) Further characterization of the mechanical properties to ensure the material can maintain its structural integrity in the intended applications, (2) Characterization of the mechanical properties under physiologically relevant conditions, (3) Additional animal studies to provide further understanding on the ability of PEEK-SP to promote osseointegration, and (4) *In vitro* studies to fundamentally separate chemistry and roughness effects.

While this thesis has showed that PEEK-SP has favorable mechanical properties, more work is needed to probe additional properties. In addition to the instantaneous deformation that compressive loading can result in, it is important to consider the time-dependent deformation. Orthopaedic polymers are susceptible to creep, the non-recoverable material flow in response to continuous loading, which can result in a significant alteration of implant geometry and biomechanical performance [258]. Long-term creep tests have shown PEEK to have excellent creep resistance at room temperature [259] and only 1% strain per month at elevated temperatures for stress levels relevant to

orthopaedic applications (5-10 MPa) [258]. However, the creep resistance of PEEK-SP has yet to be studied. In addition, the study of the material's resistance to cyclic creep (progressive deformation) would be beneficial. Furthermore, it is important to study the compressive fatigue resistance of PEEK-SP as the compressive loads will often be cyclic in nature. Testing under physiologically relevant conditions is also needed to ensure no change in mechanical properties; these tests should be run at body temperature in a salt water bath. Finally, application specific testing, such as insertion tests or torsion testing, is needed to ensure the material will meet the demands placed on it by the human body.

Further characterization of the *in vivo* response of PEEK-SP will provide understanding of the bone formation within the pore network and will help elucidate how early the bone forms, the quantitative mechanics of the bone-implant interface, and whether the improved integration results in better functional outcomes. Future *in vitro* work will seek to understand and separate the effects of chemistry and topography. Most studies demonstrating poor osseointegration of PEEK have been on smooth implants while many studies highlighting the favorable response of titanium have been on rough titanium implants. In fact, smooth titanium has shown limited bone contact and a fibrous interface with low shear strength [190, 260]. The literature, therefore, indicates that surface topography, not chemistry, is the dominant factor in both cellular response and osseointegration but future work seeks to demonstrate this in a systematic and fundamental study.

Ultimately, this work demonstrated the feasibility of creating a surface porous PEEK construct that would maintain adequate mechanical properties for orthopaedic applications while providing a surface that promoted bone ingrowth and superior

integration. Although numerous applications can be envisioned, one of the most promising is the introduction of this material in spinal fusion. Five billion dollars are spent annually on revision surgeries to correct failed spinal fusion surgeries where poor fixation of the implants is a major cause (PEEK is used in >50% of surgeries). This technology was FDA 510(k) cleared on the COHERE™ Cervical Interbody Fusion Device (Vertera Spine, Atlanta, GA) in 2015 to address this problem and the first human case is expected soon. While the research in this thesis furthered the understanding of the link between polymer processing, structure, and properties and demonstrated the creation and characterization of a novel material, the true goal is the improvement of human health and the improvement of current clinical outcomes.

REFERENCES

1. Kurtz, S.M. and J.N. Devine, *PEEK biomaterials in trauma, orthopedic, and spinal implants*. *Biomaterials*, 2007. **28**(32): p. 4845-4869.
2. Rajaei, S.S., et al., *Spinal fusion in the United States: analysis of trends from 1998 to 2008*. *Spine (Phila Pa 1976)*, 2012. **37**(1): p. 67-76.
3. Awaja, F., et al., *Cell Adhesion to PEEK Treated by Plasma Immersion Ion Implantation and Deposition for Active Medical Implants*. *Plasma Processes and Polymers*, 2012. **9**(4): p. 355-362.
4. Sagomonyants, K.B., et al., *The in vitro response of human osteoblasts to polyetheretherketone (PEEK) substrates compared to commercially pure titanium*. *Biomaterials*, 2008. **29**(11): p. 1563-1572.
5. Abu Bakar, M.S., P. Cheang, and K.A. Khor, *Mechanical properties of injection molded hydroxyapatite-polyetheretherketone biocomposites*. *Composites Science and Technology*, 2003. **63**(3-4): p. 421-425.
6. Abu Bakar, M.S., et al., *Tensile properties, tension-tension fatigue and biological response of polyetheretherketone-hydroxyapatite composites for load-bearing orthopedic implants*. *Biomaterials*, 2003. **24**(13): p. 2245-2250.
7. Tan, K.H., et al., *Scaffold development using selective laser sintering of polyetheretherketone-hydroxyapatite biocomposite blends*. *Biomaterials*, 2003. **24**(18): p. 3115-3123.
8. Converse, G.L., T.L. Conrad, and R.K. Roeder, *Mechanical properties of hydroxyapatite whisker reinforced polyetheretherketone composite scaffolds*. *Journal of the Mechanical Behavior of Biomedical Materials*, 2009. **2**(6): p. 627-635.
9. Zhang, G., et al., *Long-term compressive property durability of carbon fibre-reinforced polyetheretherketone composite in physiological saline*. *Biomaterials*, 1996. **17**(8): p. 781-789.
10. Scotchford, C.A., et al., *Use of a novel carbon fibre composite material for the femoral stem component of a THR system: in vitro biological assessment*. *Biomaterials*, 2003. **24**(26): p. 4871-4879.
11. Han, C.-M., et al., *The electron beam deposition of titanium on polyetheretherketone (PEEK) and the resulting enhanced biological properties*. *Elsevier*, 2009. **31**: p. 3465-3470.

12. Yao, C., D. Storey, and J. Webster, *Nanostructured metal coatings on polymers increase osteoblast attachment*. International Journal of Nanomedicine, 2007. **2**(3): p. 487-492.
13. Ha, S.W., et al., *Surface analysis of chemically-etched and plasma-treated polyetheretherketone (PEEK) for biomedical applications*. Surface & Coatings Technology, 1997. **96**(2-3): p. 293-299.
14. Briem, D., et al., *Response of primary fibroblasts and osteoblasts to plasma treated polyetheretherketone (PEEK) surfaces*. Journal of Materials Science-Materials in Medicine, 2005. **16**(7): p. 671-677.
15. Marcus Jarman-Smith, et al., *Porosity in Polyaryletheretherketone*, in *PEEK Biomaterials Handbook*, S.M. Kurtz, Editor. 2011, Elsevier Science. p. 181-200.
16. Shenton, M.J. and G.C. Stevens, *Surface modification of polymer surfaces: atmospheric plasma versus vacuum plasma treatments*. Journal of Physics D: Applied Physics, 2001. **34**(18): p. 2761.
17. Karageorgiou, V. and D. Kaplan, *Porosity of 3D biomaterial scaffolds and osteogenesis*. Biomaterials, 2005. **26**(27): p. 5474-91.
18. Reitman, M., et al., *Morphology and Crystallin Architecture of Polyaryetherketones*, in *PEEK Biomaterials Handbook*, S.M. Kurtz, Editor. 2011, William Andrew.
19. Dawson, P. and D. Blundell, *X-ray data for poly(aryl ether ketones)*. Polymer, 1980. **1**.
20. Sasuga, T. and M. Hagiwara, *Radiation deterioration of several aromatic polymers under oxidative conditions*. Polymer, 1987. **28**(11): p. 1915-1921.
21. Li, H.M., et al., *The effects on polyetheretherketone and polyethersulfone of electron and γ irradiation*. Dielectrics and Electrical Insulation, IEEE Transactions on, 1999. **6**(3): p. 295-303.
22. Godara, A., D. Raabe, and S. Green, *The influence of sterilization processes on the micromechanical properties of carbon fiber-reinforced PEEK composites for bone implant applications*. Acta Biomaterialia, 2007. **3**(2): p. 209-220.
23. Wenz, L.M., et al., *In vitro biocompatibility of polyetheretherketone and polysulfone composites*. J Biomed Mater Res, 1990. **24**(2): p. 207-15.
24. Katzer, A., et al., *Polyetheretherketone--cytotoxicity and mutagenicity in vitro*. Biomaterials, 2002. **23**(8): p. 1749-59.

25. Hamdan, S. and G.M. Swallowe, *The strain-rate and temperature dependence of the mechanical properties of polyetherketone and polyetheretherketone*. Journal of Materials Science, 1996. **31**(6): p. 1415-1423.
26. Rae, P.J., E.N. Brown, and E.B. Orler, *The mechanical properties of poly(ether-ether-ketone) (PEEK) with emphasis on the large compressive strain response*. Polymer, 2007. **48**(2): p. 598-615.
27. Cady, C.M., et al., *Determining the constitutive response of polymeric materials as a function of temperature and strain rate*. J. Phys. IV France, 2003. **110**: p. 27-32.
28. Chivers, R.A. and D.R. Moore, *The effect of molecular weight and crystallinity on the mechanical properties of injection moulded poly(aryl-ether-ether-ketone) resin*. Polymer, 1994. **35**(1): p. 110-116.
29. Cebe, P., S.Y. Chung, and S.-D. Hong, *Effect of thermal history on mechanical properties of polyetheretherketone below the glass transition temperature*. Journal of Applied Polymer Science, 1987. **33**(2): p. 487-503.
30. Evans, N.T., et al., *Impact of surface porosity and topography on the mechanical behavior of high strength biomedical polymers*. Journal of the Mechanical Behavior of Biomedical Materials, 2016. **59**: p. 459-473.
31. Ratner, B.D., et al., *Biomaterials Science: An Introduction to Materials in Medicine*. 2012: Elsevier Science.
32. Hargreaves, B.A., et al., *Metal-induced artifacts in MRI*. AJR Am J Roentgenol, 2011. **197**(3): p. 547-55.
33. Stradiotti, P., et al., *Metal-related artifacts in instrumented spine. Techniques for reducing artifacts in CT and MRI: state of the art*. European Spine Journal, 2009. **18**(1): p. 102-108.
34. BOBYN, J.D., et al., *Producing and Avoiding Stress Shielding: Laboratory and Clinical Observations of Noncemented Total Hip Arthroplasty*. Clinical Orthopaedics and Related Research, 1992. **274**: p. 79-96.
35. Nagels, J., M. Stokdijk, and P.M. Rozing, *Stress shielding and bone resorption in shoulder arthroplasty*. J Shoulder Elbow Surg, 2003. **12**(1): p. 35-9.
36. Williams, D.F., A. McNamara, and R.M. Turner, *Potential of polyetheretherketone (PEEK) and carbon-fibre-reinforced PEEK in medical applications*. Journal of Materials Science Letters, 1987. **6**(2): p. 188-190.
37. Rubin, C.T., *Skeletal strain and the functional significance of bone architecture*. Calcif Tissue Int, 1984. **36 Suppl 1**: p. S11-8.

38. Rubin, C.T. and L.E. Lanyon, *Regulation of bone mass by mechanical strain magnitude*. Calcif Tissue Int, 1985. **37**(4): p. 411-7.
39. Skinner, H.B., *Composite technology for total hip arthroplasty*. Clin Orthop Relat Res, 1988(235): p. 224-36.
40. Brown, S.A., et al., *Characterization of short-fibre reinforced thermoplastics for fracture fixation devices*. Biomaterials, 1990. **11**(8): p. 541-7.
41. Brantigan, J.W., A. Neidre, and J.S. Toohey, *The Lumbar I/F Cage for posterior lumbar interbody fusion with the variable screw placement system: 10-year results of a Food and Drug Administration clinical trial*. Spine J, 2004. **4**(6): p. 681-8.
42. Brantigan, J.W., et al., *Lumbar interbody fusion using the Brantigan I/F cage for posterior lumbar interbody fusion and the variable pedicle screw placement system: two-year results from a Food and Drug Administration investigational device exemption clinical trial*. Spine (Phila Pa 1976), 2000. **25**(11): p. 1437-46.
43. Akhavan, S., et al., *Clinical and histologic results related to a low-modulus composite total hip replacement stem*. J Bone Joint Surg Am, 2006. **88**(6): p. 1308-14.
44. Glassman, A.H., et al., *A low stiffness composite biologically fixed prosthesis*. Clin Orthop Relat Res, 2001(393): p. 128-36.
45. Jiya, T., et al., *Posterior lumbar interbody fusion using non resorbable poly-ether-ether-ketone versus resorbable poly-l-lactide-co-d,l-lactide fusion devices. Clinical outcome at a minimum of 2-year follow-up*. European Spine Journal, 2011. **20**(4): p. 618-622.
46. Cho, D.-Y., et al., *Preliminary Experience Using a Polyetheretherketone (PEEK) Cage in the Treatment of Cervical Disc Disease*. Neurosurgery, 2002. **51**(6): p. 1343-1350 10.1227/01.NEU.0000309109.71345.19.
47. Jockisch, K.A., et al., *Biological response to chopped-carbon-fiber-reinforced peek*. J Biomed Mater Res, 1992. **26**(2): p. 133-46.
48. Nieminen, T., et al., *Amorphous and crystalline polyetheretherketone: Mechanical properties and tissue reactions during a 3-year follow-up*. J Biomed Mater Res A, 2008. **84**(2): p. 377-83.
49. Gittens, R.A., et al., *Implant osseointegration and the role of microroughness and nanostructures: Lessons for spine implants*. Acta Biomater, 2014.
50. Athanasou, N.A., J. Quinn, and C.J. Bulstrode, *Resorption of bone by inflammatory cells derived from the joint capsule of hip arthroplasties*. J Bone Joint Surg Br, 1992. **74**(1): p. 57-62.

51. Wazen, R.M., et al., *Micromotion-induced strain fields influence early stages of repair at bone-implant interfaces*. Acta Biomater, 2013. **9**(5): p. 6663-74.
52. Maniatopoulos, C., R.M. Pilliar, and D.C. Smith, *Threaded versus porous-surfaced designs for implant stabilization in bone-endodontic implant model*. J Biomed Mater Res, 1986. **20**(9): p. 1309-33.
53. Robotti, P. and G. Zappini, *Thermal Plasma Spray Deposition of Titanium and Hydroxyapatite on Polyaryletheretherketone Implants*, in *PEEK Biomaterials Handbook*, S.M. Kurtz, Editor. 2011, William Andrew. p. 119-144.
54. Buser, D., et al., *Enhanced bone apposition to a chemically modified SLA titanium surface*. Journal of Dental Research, 2004. **83**(7): p. 529-533.
55. Hacking, S.A., et al., *Surface roughness enhances the osseointegration of titanium headposts in non-human primates*. J Neurosci Methods, 2012. **211**(2): p. 237-44.
56. Deng, Y., et al., *Effect of surface roughness on osteogenesis in vitro and osseointegration in vivo of carbon fiber-reinforced polyetheretherketone-nanohydroxyapatite composite*. Int J Nanomedicine, 2015. **10**: p. 1425-47.
57. Wang, H., et al., *Tailoring of mesenchymal stem cells behavior on plasma-modified polytetrafluoroethylene*. Adv Mater, 2012. **24**(25): p. 3315-24.
58. Shalabi, M.M., et al., *Implant surface roughness and bone healing: a systematic review*. Journal of Dental Research, 2006. **85**(6): p. 496-500.
59. Wong, M., et al., *Effect of Surface-Topology on the Osseointegration of Implant Materials in Trabecular Bone*. Journal of Biomedical Materials Research, 1995. **29**(12): p. 1567-1575.
60. Kieswetter, K., et al., *Surface roughness modulates the local production of growth factors and cytokines by osteoblast-like MG-63 cells*. Journal of Biomedical Materials Research, 1996. **32**(1): p. 55-63.
61. Poulsson, A.H.C. and R.G. Richards, *Surface Modifications Techniques of Polyaryletheretherketone, Including Plasma Surface Treatment*, in *PEEK Biomaterials Handbook*. 2011, William Andrew. p. 145-162.
62. Fricke, K., et al., *Investigation of Surface Etching of Poly(Ether Ether Ketone) by Atmospheric-Pressure Plasmas*. Ieee Transactions on Plasma Science, 2012. **40**(11): p. 2900-2911.
63. Poulsson, A.H.C., et al., *Osseointegration of machined, injection moulded and oxygen plasma modified PEEK implants in a sheep model*. Biomaterials, 2014. **35**(12): p. 3717-3728.

64. Schröder, K., et al., *Similarities between Plasma Amino Functionalized PEEK and Titanium Surfaces Concerning Enhancement of Osteoblast Cell Adhesion*. Journal of Adhesion Science and Technology, 2010. **24**(5): p. 905-923.
65. Wang, H., et al., *Enhanced osteoblast responses to poly ether ether ketone surface modified by water plasma immersion ion implantation*. Colloids and Surfaces B: Biointerfaces, 2014. **117**(0): p. 89-97.
66. Suska, F., et al., *Enhancement of CRF-PEEK osseointegration by plasma-sprayed hydroxyapatite: A rabbit model*. J Biomater Appl, 2014.
67. Lee, J.H., et al., *In vitro and in vivo evaluation of the bioactivity of hydroxyapatite-coated polyetheretherketone biocomposites created by cold spray technology*. Acta Biomaterialia, 2013. **9**(4): p. 6177-6187.
68. Van Noort, R., *Titanium: The implant material of today*. Journal of Materials Science, 1987. **22**(11): p. 3801-3811.
69. Cook, S.D. and A.M. Rust-Dawicki, *Preliminary evaluation of titanium-coated PEEK dental implants*. J Oral Implantol, 1995. **21**(3): p. 176-81.
70. Devine, D.M., et al., *Coating of carbon fiber-reinforced polyetheretherketone implants with titanium to improve bone apposition*. J Biomed Mater Res B Appl Biomater, 2013. **101**(4): p. 591-8.
71. Wang, H., et al., *Mechanical and biological characteristics of diamond-like carbon coated poly aryl-ether-ether-ketone*. Biomaterials, 2010. **31**(32): p. 8181-8187.
72. Tan, K.H., et al., *Fabrication and characterization of three-dimensional poly(ether-ether-ketone)/-hydroxyapatite biocomposite scaffolds using laser sintering*. Proceedings of the Institution of Mechanical Engineers, Part H: Journal of Engineering in Medicine, 2005. **219**(3): p. 183-194.
73. Rezwani, K., et al., *Biodegradable and bioactive porous polymer/inorganic composite scaffolds for bone tissue engineering*. Biomaterials, 2006. **27**(18): p. 3413-3431.
74. Hench, L.L., *Bioceramics: From Concept to Clinic*. Journal of the American Ceramic Society, 1991. **74**(7): p. 1487-1510.
75. LeGeros, R.Z., *Properties of osteoconductive biomaterials: calcium phosphates*. Clin Orthop Relat Res, 2002(395): p. 81-98.
76. Bobyn, J.D., et al., *Characteristics of bone ingrowth and interface mechanics of a new porous tantalum biomaterial*. J Bone Joint Surg Br, 1999. **81**(5): p. 907-14.
77. Hertzberg, R.W., H. Nordberg, and J. Manson, *Fatigue crack propagation in polymeric materials*. Journal of Materials Science, 1970. **5**(6): p. 521-526.

78. Pruitt, L.A. and A.M. Chakravartula, *Mechanics of Biomaterials: Fundamental Principles for Implant Design*. 2011: Cambridge University Press.
79. Lampman, S., *Fatigue Testing and Behavior*, in *Characterization and Failure Analysis of Plastics*. 2003, A S M International.
80. Rao, I.J. and K.R. Rajagopal, *A study of strain-induced crystallization of polymers*. International Journal of Solids and Structures, 2001. **38**(6–7): p. 1149-1167.
81. Soboyejo, W., *Mechanical Properties of Engineered Materials*. 2002: CRC Press.
82. Lesser, A.J., *Fatigue Behavior of Polymers*, in *Encyclopedia of Polymer Science and Technology*. 2002, John Wiley & Sons, Inc.
83. Sauer, J.A. and G.C. Richardson, *Fatigue of polymers*. International Journal of Fracture, 1980. **16**(6): p. 499-532.
84. Lesser, A.J., *Changes in mechanical behavior during fatigue of semicrystalline thermoplastics*. Journal of Applied Polymer Science, 1995. **58**(5): p. 869-879.
85. Riddell, M.N., G.P. Koo, and J.L. O'Toole, *Fatigue mechanisms of thermoplastics*. Polymer Engineering & Science, 1966. **6**(4): p. 363-368.
86. Scheirs, J., *Compositional and Failure Analysis of Polymers: A Practical Approach*. 2000: Wiley.
87. International, A. and S. Lampman, *Characterization and Failure Analysis of Plastics*. 2003: A S M International.
88. Hildebrand, T., et al., *Direct three-dimensional morphometric analysis of human cancellous bone: microstructural data from spine, femur, iliac crest, and calcaneus*. J Bone Miner Res, 1999. **14**(7): p. 1167-74.
89. Lin, A.S., et al., *Microarchitectural and mechanical characterization of oriented porous polymer scaffolds*. Biomaterials, 2003. **24**(3): p. 481-9.
90. Blundell, D.J. and B.N. Osborn, *The morphology of poly(aryl-ether-ether-ketone)*. Polymer, 1983. **24**(8): p. 953-958.
91. Chalmers, J., W. Gaskin, and M. Mackenzie, *Crystallinity in poly (aryl-ether-ketone) plaques studied by multiple internal reflection spectroscopy*. Polymer Bulletin, 1984. **11**(5): p. 433-435.
92. Oest, M.E., et al., *Quantitative assessment of scaffold and growth factor-mediated repair of critically sized bone defects*. J Orthop Res, 2007. **25**(7): p. 941-50.

93. Van der Stok, J., et al., *Selective laser melting-produced porous titanium scaffolds regenerate bone in critical size cortical bone defects*. J Orthop Res, 2013. **31**(5): p. 792-9.
94. Dupont, K.M., et al., *Human stem cell delivery for treatment of large segmental bone defects*. Proceedings of the National Academy of Sciences, 2010. **107**(8): p. 3305-3310.
95. Rai, B., et al., *Combination of platelet-rich plasma with polycaprolactone-tricalcium phosphate scaffolds for segmental bone defect repair*. J Biomed Mater Res A, 2007. **81**(4): p. 888-99.
96. Wojtowicz, A.M., et al., *Coating of biomaterial scaffolds with the collagen-mimetic peptide GFOGER for bone defect repair*. Biomaterials, 2010. **31**(9): p. 2574-82.
97. Czekanska, E.M., et al., *In search of an osteoblast cell model for in vitro research*. Eur Cell Mater, 2012. **24**: p. 1-17.
98. Place, E.S., N.D. Evans, and M.M. Stevens, *Complexity in biomaterials for tissue engineering*. Nat Mater, 2009. **8**(6): p. 457-70.
99. Nagels, J., M. Stokdijk, and P.M. Rozing, *Stress shielding and bone resorption in shoulder arthroplasty*. Journal of Shoulder and Elbow Surgery, 2003. **12**(1): p. 35-39.
100. DiRienzo, A.L., et al., *Porous poly(para-phenylene) scaffolds for load-bearing orthopedic applications*. Journal of the Mechanical Behavior of Biomedical Materials, 2014. **30**(0): p. 347-357.
101. Pereira, H.D., et al., *Migration of "bioabsorbable" screws in ACL repair. How much do we know? A systematic review*. Knee Surgery, Sports Traumatology, Arthroscopy, 2013: p. 1-9.
102. Kurtz, S.M., *An Overview of PEEK Biomaterials*, in *PEEK Biomaterials Handbook*. 2011, William Andrew. p. 1-8.
103. Arima, Y. and H. Iwata, *Effect of wettability and surface functional groups on protein adsorption and cell adhesion using well-defined mixed self-assembled monolayers*. Biomaterials, 2007. **28**(20): p. 3074-3082.
104. Ha, S.W., et al., *Surface activation of polyetheretherketone (PEEK) and formation of calcium phosphate coatings by precipitation*. Journal of Materials Science-Materials in Medicine, 1997. **8**(11): p. 683-690.
105. Bakar, A., et al., *Tensile properties, tension-tension fatigue and biological response of polyetheretherketone-hydroxyapatite composites for load-bearing orthopedic implants*. Biomaterials, 2003. **24**(13): p. 2245-2250.

106. Karageorgiou, V. and D. Kaplan, *Porosity of 3D biomaterial scaffolds and osteogenesis*. *Biomaterials*, 2005. **26**(27): p. 5474-5491.
107. Landy, B.C., et al., *Mechanical and in vitro investigation of a porous PEEK foam for medical device implants*. *J Appl Biomater Funct Mater*, 2013. **11**(1): p. e35-44.
108. Sinclair, S.K., et al., *Host bone response to polyetheretherketone versus porous tantalum implants for cervical spinal fusion in a goat model*. *Spine (Phila Pa 1976)*, 2012. **37**(10): p. E571-80.
109. Zhou, J., et al., *The repair of large segmental bone defects in the rabbit with vascularized tissue engineered bone*. *Biomaterials*, 2010. **31**(6): p. 1171-9.
110. Muller, U., et al., *Do human osteoblasts grow into open-porous titanium?* *Eur Cell Mater*, 2006. **11**: p. 8-15.
111. Zardiackas, L.D., et al., *Structure, metallurgy, and mechanical properties of a porous tantalum foam*. *Journal of Biomedical Materials Research*, 2001. **58**(2): p. 180-187.
112. Goldstein, S.A., *The mechanical properties of trabecular bone: dependence on anatomic location and function*. *J Biomech*, 1987. **20**(11-12): p. 1055-61.
113. He, Q., et al., *Porous Surface Modified Bioactive Bone Cement for Enhanced Bone Bonding*. *Plos One*, 2012. **7**(8).
114. Zhao, Y., et al., *Cytocompatibility, osseointegration, and bioactivity of three-dimensional porous and nanostructured network on polyetheretherketone*. *Biomaterials*, 2013. **34**(37): p. 9264-9277.
115. Shimko, D.A., et al., *Effect of porosity on the fluid flow characteristics and mechanical properties of tantalum scaffolds*. *Journal of Biomedical Materials Research Part B: Applied Biomaterials*, 2005. **73B**(2): p. 315-324.
116. Eshraghi, S. and S. Das, *Mechanical and microstructural properties of polycaprolactone scaffolds with one-dimensional, two-dimensional, and three-dimensional orthogonally oriented porous architectures produced by selective laser sintering*. *Acta Biomater*, 2010. **6**(7): p. 2467-76.
117. Kurtz, S.M., *A Primer on UHMWPE*, in *UHMWPE Biomaterials Handbook: Ultra High Molecular Weight Polyethylene in Total Joint Replacement and Medical Devices*. 2009, Elsevier Science. p. 1-6.
118. Wang, L., et al., *Characterization of porous polymethylmethacrylate space maintainers for craniofacial reconstruction*. *J Biomed Mater Res B Appl Biomater*, 2013. **101**(5): p. 813-25.

119. Suwanprateeb, J. and R. Chumnanklang, *Three-dimensional printing of porous polyethylene structure using water-based binders*. J Biomed Mater Res B Appl Biomater, 2006. **78**(1): p. 138-45.
120. Cheal, E.J., M. Spector, and W.C. Hayes, *Role of loads and prosthesis material properties on the mechanics of the proximal femur after total hip arthroplasty*. J Orthop Res, 1992. **10**(3): p. 405-22.
121. Bobyn, J.D., et al., *The effect of porous surface configuration on the tensile strength of fixation of implants by bone ingrowth*. Clin Orthop Relat Res, 1980(149): p. 291-8.
122. Yao, C., D. Storey, and T.J. Webster, *Nanostructured metal coatings on polymers increase osteoblast attachment*. Int J Nanomedicine, 2007. **2**(3): p. 487-92.
123. Dalby, M.J., et al., *The control of human mesenchymal cell differentiation using nanoscale symmetry and disorder*. Nature Materials, 2007. **6**(12): p. 997-1003.
124. Meyer, U., et al., *Basic reactions of osteoblasts on structured material surfaces*. European cells & materials, 2005. **9**: p. 39-49.
125. Nieminen, T., et al., *Amorphous and crystalline polyetheretherketone: Mechanical properties and tissue reactions during a 3-year follow-up*. Journal of Biomedical Materials Research Part A, 2008. **84A**(2): p. 377-383.
126. Jockisch, K.A., et al., *Biological response to chopped-carbon-fiber-reinforced peek*. Journal of Biomedical Materials Research, 1992. **26**(2): p. 133-146.
127. Götz, H.E., et al., *Effect of surface finish on the osseointegration of laser-treated titanium alloy implants*. Biomaterials, 2004. **25**(18): p. 4057-4064.
128. Aspenberg, P., et al., *INTERMITTENT MICROMOTION INHIBITS BONE INGROWTH - TITANIUM IMPLANTS IN RABBITS*. Acta Orthopaedica Scandinavica, 1992. **63**(2): p. 141-145.
129. Guldborg, R.E., et al., *Trabecular bone adaptation to variations in porous-coated implant topology*. J Biomech, 1997. **30**(2): p. 147-53.
130. Toth, J.M., et al., *Polyetheretherketone as a biomaterial for spinal applications*. Biomaterials, 2006. **27**(3): p. 324-34.
131. Roeder, R., et al., *Porous and Bioactive PEEK Implants for Interbody Spinal Fusion*. Advanced Materials and Processes, 2009. **167**(10): p. 46-48.
132. Tan, K.H., et al., *Fabrication and characterization of three-dimensional poly(ether- ether- ketone)/-hydroxyapatite biocomposite scaffolds using laser sintering*. Proc Inst Mech Eng H, 2005. **219**(3): p. 183-94.

133. Lewallen, E.A., et al., *Biological Strategies for Improved Osseointegration and Osteoinduction of Porous Metal Orthopedic Implants*. Tissue Eng Part B Rev, 2014.
134. Evans, N.T., et al., *High-strength, surface-porous polyether-ether-ketone for load-bearing orthopedic implants*. Acta Biomater, 2015. **13**: p. 159-67.
135. Zhao, Y., et al., *Cytocompatibility, osseointegration, and bioactivity of three-dimensional porous and nanostructured network on polyetheretherketone*. Biomaterials, 2013. **34**(37): p. 9264-9277.
136. Siddiq, A.R. and A.R. Kennedy, *Porous poly-ether ether ketone (PEEK) manufactured by a novel powder route using near-spherical salt bead porogens: Characterisation and mechanical properties*. Materials Science and Engineering: C, 2015. **47**: p. 180-188.
137. Shu, L.H., et al., *Biologically inspired design*. CIRP Annals - Manufacturing Technology, 2011. **60**(2): p. 673-693.
138. Pompe, W., et al., *Functionally graded materials for biomedical applications*. Materials Science and Engineering: A, 2003. **362**(1-2): p. 40-60.
139. Watari, F., et al., *Biocompatibility of materials and development to functionally graded implant for bio-medical application*. Composites Science and Technology, 2004. **64**(6): p. 893-908.
140. Leong, K.F., et al., *Engineering functionally graded tissue engineering scaffolds*. Journal of the Mechanical Behavior of Biomedical Materials, 2008. **1**(2): p. 140-152.
141. Bandyopadhyay, A., et al., *Application of Laser Engineered Net Shaping (LENS) to manufacture porous and functionally graded structures for load bearing implants*. Journal of Materials Science-Materials in Medicine, 2009. **20**: p. 29-34.
142. Miao, X. and D. Sun, *Graded/gradient porous biomaterials*. Materials, 2009. **3**(1): p. 26-47.
143. Hsu, Y.H., I.G. Turner, and A.W. Miles, *Fabrication of porous bioceramics with porosity gradients similar to the bimodal structure of cortical and cancellous bone*. J Mater Sci Mater Med, 2007. **18**(12): p. 2251-6.
144. Tampieri, A., et al., *Porosity-graded hydroxyapatite ceramics to replace natural bone*. Biomaterials, 2001. **22**(11): p. 1365-1370.
145. Thomopoulos, S., V. Birman, and G.M. Genin, *Structural Interfaces and Attachments in Biology*. 2012: Springer New York.

146. Griffon, D.J., et al., *Chitosan scaffolds: interconnective pore size and cartilage engineering*. Acta biomaterialia, 2006. **2**(3): p. 313-320.
147. Salem, A., et al., *Interactions of 3T3 fibroblasts and endothelial cells with defined pore features*. Journal of biomedical materials research, 2002. **61**(2): p. 212-217.
148. Oh, S.H., et al., *In vitro and in vivo characteristics of PCL scaffolds with pore size gradient fabricated by a centrifugation method*. Biomaterials, 2007. **28**(9): p. 1664-1671.
149. O'Brien, F.J., et al., *The effect of pore size on cell adhesion in collagen-GAG scaffolds*. Biomaterials, 2005. **26**(4): p. 433-441.
150. Gibson, L.J. and M.F. Ashby, *Cellular Solids: Structure and Properties*. 1999: Cambridge University Press.
151. Halawa, M., et al., *The shear strength of trabecular bone from the femur, and some factors affecting the shear strength of the cement-bone interface*. Archives of orthopaedic and traumatic surgery, 1978. **92**(1): p. 19-30.
152. Wu, S.-H., et al., *Porous titanium-6 aluminum-4 vanadium cage has better osseointegration and less micromotion than a poly-ether-ether-ketone cage in sheep vertebral fusion*. Artificial Organs, 2013. **37**(12): p. E191-E201.
153. Boyan, B.D., et al., *Role of material surfaces in regulating bone and cartilage cell response*. Biomaterials, 1996. **17**(2): p. 137-146.
154. Gregory, D.R. and R.G. Griskey, *Flow of molten polymers through porous media*. AIChE Journal, 1967. **13**(1): p. 122-125.
155. Takano, M. and L.E. Nielsen, *The notch sensitivity of polymeric materials*. Journal of Applied Polymer Science, 1976. **20**(8): p. 2193-2207.
156. Sobieraj, M.C., S.M. Kurtz, and C.M. Rimnac, *Notch sensitivity of PEEK in monotonic tension*. Biomaterials, 2009. **30**(33): p. 6485-6494.
157. Nielsen, L.E., *FATIGUE BEHAVIOR OF SOME FILLED POLYMERS*. Bulletin of the American Physical Society, 1975. **20**(3): p. 481-481.
158. Teoh, S.H., *Fatigue of biomaterials: a review*. International Journal of Fatigue, 2000. **22**(10): p. 825-837.
159. James, S.P., et al., *A fractographic investigation of PMMA bone cement focusing on the relationship between porosity reduction and increased fatigue life*. J Biomed Mater Res, 1992. **26**(5): p. 651-62.

160. Ishihara, S., et al., *On fatigue lifetimes and fatigue crack growth behavior of bone cement*. Journal of Materials Science: Materials in Medicine, 2000. **11**(10): p. 661-666.
161. Schultz, A.B. and G.B. Andersson, *Analysis of loads on the lumbar spine*. Spine, 1981. **6**(1): p. 76-82.
162. Nachemson, A., *Lumbar intradiscal pressure: experimental studies on post-mortem material*. Acta Orthopaedica, 1960. **31**(S43): p. 1-104.
163. Wilke, H.J., et al., *New in vivo measurements of pressures in the intervertebral disc in daily life*. Spine, 1999. **24**(8): p. 755-762.
164. Lian, J.B. and G.S. Stein, *Concepts of osteoblast growth and differentiation: basis for modulation of bone cell development and tissue formation*. Crit Rev Oral Biol Med, 1992. **3**(3): p. 269-305.
165. Zhao, G., et al., *Requirement for both micron- and submicron scale structure for synergistic responses of osteoblasts to substrate surface energy and topography*. Biomaterials, 2007. **28**(18): p. 2821-9.
166. Czekanska, E.M., et al., *A phenotypic comparison of osteoblast cell lines versus human primary osteoblasts for biomaterials testing*. J Biomed Mater Res A, 2014. **102**(8): p. 2636-43.
167. Zhou, Y.F., et al., *Does seeding density affect in vitro mineral nodules formation in novel composite scaffolds?* J Biomed Mater Res A, 2006. **78**(1): p. 183-93.
168. Ishaug-Riley, S.L., et al., *Three-dimensional culture of rat calvarial osteoblasts in porous biodegradable polymers*. Biomaterials, 1998. **19**(15): p. 1405-1412.
169. Cartmell, S.H., et al., *Effects of medium perfusion rate on cell-seeded three-dimensional bone constructs in vitro*. Tissue Eng, 2003. **9**(6): p. 1197-203.
170. Steinbrech, D.S., et al., *VEGF expression in an osteoblast-like cell line is regulated by a hypoxia response mechanism*. Am J Physiol Cell Physiol, 2000. **278**(4): p. C853-60.
171. Dai, J. and A.B. Rabie, *VEGF: an essential mediator of both angiogenesis and endochondral ossification*. J Dent Res, 2007. **86**(10): p. 937-50.
172. Mayer, H., et al., *Vascular endothelial growth factor (VEGF-A) expression in human mesenchymal stem cells: autocrine and paracrine role on osteoblastic and endothelial differentiation*. J Cell Biochem, 2005. **95**(4): p. 827-39.
173. Pruitt, L. and J. Furmanski, *Polymeric biomaterials for load-bearing medical devices*. JOM, 2009. **61**(9): p. 14-20.

174. Saini, M., et al., *Implant biomaterials: A comprehensive review*. World J Clin Cases, 2015. **3**(1): p. 52-7.
175. Parithimarkalaignan, S. and T.V. Padmanabhan, *Osseointegration: An Update*. The Journal of Indian Prosthodontic Society, 2013. **13**(1): p. 2-6.
176. Danza, M., et al., *Titanium alloys (AoN) and their involvement in osseointegration*. Dental research journal, 2012. **9**(Suppl 2): p. S207.
177. Ma, R. and T. Tang, *Current strategies to improve the bioactivity of PEEK*. International journal of molecular sciences, 2014. **15**(4): p. 5426-5445.
178. Lossdörfer, S., et al., *Microrough implant surface topographies increase osteogenesis by reducing osteoclast formation and activity*. Journal of Biomedical Materials Research Part A, 2004. **70**(3): p. 361-369.
179. Alla, R.K., et al., *Surface roughness of implants: a review*. Trends in Biomaterials and Artificial Organs, 2011. **25**(3): p. 112-118.
180. Lincks, J., et al., *Response of MG63 osteoblast-like cells to titanium and titanium alloy is dependent on surface roughness and composition*. Biomaterials, 1998. **19**(23): p. 2219-2232.
181. Kim, M.J., et al., *Microrough titanium surface affects biologic response in MG63 osteoblast-like cells*. Journal of biomedical materials research Part A, 2006. **79**(4): p. 1023-1032.
182. Schwartz, Z., et al., *Effect of micrometer-scale roughness of the surface of Ti6Al4V pedicle screws in vitro and in vivo*. J Bone Joint Surg Am, 2008. **90**(11): p. 2485-98.
183. Zhao, G., et al., *Osteoblast-like cells are sensitive to submicron-scale surface structure*. Clinical oral implants research, 2006. **17**(3): p. 258-264.
184. Balloni, S., et al., *Effects of titanium surface roughness on mesenchymal stem cell commitment and differentiation signaling*. The International journal of oral & maxillofacial implants, 2008. **24**(4): p. 627-635.
185. Olivares-Navarrete, R., et al., *The roles of Wnt signaling modulators Dickkopf-1 (Dkk1) and Dickkopf-2 (Dkk2) and cell maturation state in osteogenesis on microstructured titanium surfaces*. Biomaterials, 2010. **31**(8): p. 2015-2024.
186. Raines, A.L., et al., *Regulation of angiogenesis during osseointegration by titanium surface microstructure and energy*. Biomaterials, 2010. **31**(18): p. 4909-4917.
187. Hyzy, S., et al., *Microstructured titanium regulates interleukin production by osteoblasts, an effect modulated by exogenous BMP-2*. Acta biomaterialia, 2013. **9**(3): p. 5821-5829.

188. Kuboki, Y., et al., *BMP-induced osteogenesis on the surface of hydroxyapatite with geometrically feasible and nonfeasible structures: topology of osteogenesis*. Journal of biomedical materials research, 1998. **39**(2): p. 190-199.
189. Story, B.J., et al., *In vivo performance of a modified CSTi dental implant coating*. The International journal of oral & maxillofacial implants, 1997. **13**(6): p. 749-757.
190. Svehla, M., et al., *Morphometric and mechanical evaluation of titanium implant integration: comparison of five surface structures*. Journal of biomedical materials research, 2000. **51**(1): p. 15-22.
191. Kinloch, A., *Fracture Behaviour of Polymers*. 1983: Springer Netherlands.
192. Nielsen, L.E., *Fatigue Behavior of Some Filled Polymers*. Journal of Composite Materials, 1975. **9**(2): p. 149-156.
193. Landel, R.F. and L.E. Nielsen, *Mechanical Properties of Polymers and Composites, Second Edition*. 1993: Taylor & Francis.
194. Suhr, R.W., *The Effect of Surface Finish on High Cycle Fatigue of a Low Alloy Steel, The Behaviour of Short Fatigue Cracks*. 1986, London: Mechanical Engineering Publications.
195. Bayoumi, M.R. and A.K. Abdellatif, *Effect of surface finish on fatigue strength*. Engineering Fracture Mechanics, 1995. **51**(5): p. 861-870.
196. Lohbauer, U., R. Frankenberger, and N. Krämer, *Surface Quality Controls Mechanical Strength and Fatigue Lifetime of Dental Ceramics and Resin Composites, Ceramic Materials*. 2010: Sciyo.
197. Weiss, B. and A. Hadrboletz, *Fatigue behaviour of iron based sintered materials: A review*. Fatigue '99: Proceedings of the Seventh International Fatigue Congress, Vols 1-4, ed. X.R. Wu and Z.G. Wang. 1999, Beijing: China Higher Education Press Beijing. 1803-1810.
198. Boccaccini, A.R., *Influence of stress concentrations on the mechanical property-porosity correlation in porous materials*. Journal of Materials Science Letters, 1998. **17**(15): p. 1273-1275.
199. Van der Stok, J., et al., *Selective laser melting-produced porous titanium scaffolds regenerate bone in critical size cortical bone defects*. Journal of Orthopaedic Research, 2013. **31**(5): p. 792-799.
200. Mitsak, A.G., et al., *Effect of polycaprolactone scaffold permeability on bone regeneration in vivo*. Tissue Eng Part A, 2011. **17**(13-14): p. 1831-9.

201. Harvey, E., et al., *Effect of flexibility of the femoral stem on bone-remodeling and fixation of the stem in a canine total hip arthroplasty model without cement*. The Journal of Bone & Joint Surgery, 1999. **81**(1): p. 93-107.
202. Morton, A.G. and I.R. Lane Jr, *Titanium Castings for Marine Propellers*, in *Titanium Science and Technology*. 1973, Springer. p. 119-130.
203. Olivares-Navarrete, R., et al., *Integrin alpha2beta1 plays a critical role in osteoblast response to micron-scale surface structure and surface energy of titanium substrates*. Proc Natl Acad Sci U S A, 2008. **105**(41): p. 15767-72.
204. Olivares-Navarrete, R., et al., *Rough titanium alloys regulate osteoblast production of angiogenic factors*. Spine J, 2013. **13**(11): p. 1563-70.
205. Zhan, H., *Numerical characterization of the mechanical properties of metal nanowires*. 2013.
206. Jones, D.R.H. and M.F. Ashby, *Engineering Materials 2: An Introduction to Microstructures, Processing and Design*. 2005: Elsevier Science.
207. Wallenberger, F.T. and P.A. Bingham, *Fiberglass and Glass Technology: Energy-Friendly Compositions and Applications*. 2009: Springer US.
208. Simske, S., R. Ayers, and T. Bateman. *Porous materials for bone engineering*. in *Materials Science Forum*. 1997. Trans Tech Publ.
209. Goolsby, R.D. and A.M. Chatterjee, *Notch sensitivity and fractography of polyolefins*. Polymer Engineering & Science, 1983. **23**(3): p. 117-124.
210. Ward, I.M. and J. Sweeney, *Yielding and Instability in Polymers*, in *Mechanical Properties of Solid Polymers*. 2012, John Wiley & Sons, Ltd. p. 319-378.
211. Hutnik, M., A.S. Argon, and U.W. Suter, *Simulation of elastic and plastic response in the glassy polycarbonate of 4,4'-isopropylidenediphenol*. Macromolecules, 1993. **26**(5): p. 1097-1108.
212. Kong, Y. and J. Hay, *The measurement of the crystallinity of polymers by DSC*. Polymer, 2002. **43**(14): p. 3873-3878.
213. Ward, I.M. and J. Sweeney, *Breaking Phenomena*, in *Mechanical Properties of Solid Polymers*. 2012, John Wiley & Sons, Ltd. p. 379-447.
214. Ganguly, P., T. Moore, and L. Gibson, *A phenomenological model for predicting fatigue life in bovine trabecular bone*. Journal of biomechanical engineering, 2004. **126**(3): p. 330-339.

215. Kanters, M.J., T. Kurokawa, and L.E. Govaert, *Competition between plasticity-controlled and crack-growth controlled failure in static and cyclic fatigue of polymer systems*. Polymer Testing, 2016.
216. Kohn, D.H. and P. Ducheyne, *A parametric study of the factors affecting the fatigue strength of porous coated Ti-6Al-4V implant alloy*. Journal of biomedical materials research, 1990. **24**(11): p. 1483-1501.
217. Cook, S.D., et al., *Fatigue properties of carbon-and porous-coated Ti-6Al-4V alloy*. Journal of biomedical materials research, 1984. **18**(5): p. 497-512.
218. Yue, S., R. Pilliar, and G. Weatherly, *The fatigue strength of porous-coated Ti-6% Al-4% V implant alloy*. Journal of biomedical materials research, 1984. **18**(9): p. 1043-1058.
219. Papakyriacou, M., et al., *Influence of loading frequency on high cycle fatigue properties of b.c.c. and h.c.p. metals*. Materials Science and Engineering: A, 2001. **308**(1-2): p. 143-152.
220. Schaffer, J.P., *The Science and Design of Engineering Materials*. 1999: WCB McGraw-Hill.
221. Kemmish, D.J. and J.N. Hay, *The effect of physical ageing on the properties of amorphous PEEK*. Polymer, 1985. **26**(6): p. 905-912.
222. Nguyen, H.X. and H. Ishida, *Poly(aryl-ether-ether-ketone) and its advanced composites: A review*. Polymer Composites, 1987. **8**(2): p. 57-73.
223. Arzak, A., J.I. Eguiazábal, and J. Nazábal, *Effect of annealing on the properties of poly(ether ether ketone)*. Polymer Engineering & Science, 1991. **31**(8): p. 586-591.
224. Rice, R.W., *Evaluation and extension of physical property-porosity models based on minimum solid area*. Journal of Materials Science, 1996. **31**(1): p. 102-118.
225. Rice, R.W., *Comparison of Stress-Concentration Versus Minimum Solid Area Based Mechanical Property Porosity Relations*. Journal of Materials Science, 1993. **28**(8): p. 2187-2190.
226. Mugica, G.W., et al., *Effect of porosity on the tensile properties of low ductility aluminum alloys*. Materials Research, 2004. **7**: p. 221-229.
227. Rice, R.W., *Limitations of pore-stress concentrations on the mechanical properties of porous materials*. Journal of Materials Science, 1997. **32**(17): p. 4731-4736.
228. Gibson, L.J. and M.F. Ashby, *Cellular solids: structure and properties*. 1997: Cambridge university press.

229. McGill, S.M., *Loads on the lumbar spine and associated tissues*. 1990: CRC Press, Boca Raton.
230. Kuster, M.S., et al., *Joint load considerations in total knee replacement*. Journal of Bone & Joint Surgery, British Volume, 1997. **79**(1): p. 109-113.
231. Bandyopadhyay, A. and S. Bose, *Chapter 7.2 Mechanical Properties of Bioceramic Coatings on Medical Implants*, in *Characterization of biomaterials*. 2013, Newnes.
232. Kurtz, S.M. and J. Nevelos, *Arthroplasty Bearing Surfaces*, in *PEEK biomaterials handbook*. 2011, William Andrew.
233. Wang, A., et al., *Suitability and limitations of carbon fiber reinforced PEEK composites as bearing surfaces for total joint replacements*. Wear, 1999. **225–229**, **Part 2**: p. 724-727.
234. Scholes, S. and A. Unsworth, *The wear properties of CFR-PEEK-OPTIMA articulating against ceramic assessed on a multidirectional pin-on-plate machine*. Proceedings of the Institution of Mechanical Engineers, Part H: Journal of Engineering in Medicine, 2007. **221**(3): p. 281-289.
235. Jones, E., A. Wang, and R. Streicher. *Validating the limits for a PEEK composite as an acetabular wear surface*. in *27 th Annual Meeting of the Society for Biomaterials in conjunction with the 33 rd International Biomaterials Symposium*. 2001.
236. Howling, G., et al., *Biological response to wear debris generated in carbon based composites as potential bearing surfaces for artificial hip joints*. Journal of Biomedical Materials Research Part B: Applied Biomaterials, 2003. **67**(2): p. 758-764.
237. Maharaj, G., et al., *Characterization of wear in composite material orthopaedic implants. Part I: The composite trunnion/ceramic head interface*. Bio-medical materials and engineering, 1993. **4**(3): p. 193-198.
238. Utzschneider, S., et al., *Inflammatory response against different carbon fiber-reinforced PEEK wear particles compared with UHMWPE in vivo*. Acta Biomaterialia, 2010. **6**(11): p. 4296-4304.
239. Rivard, C.H., S. Rhalmi, and C. Coillard, *In vivo biocompatibility testing of peek polymer for a spinal implant system: a study in rabbits*. J Biomed Mater Res, 2002. **62**(4): p. 488-98.
240. Stadelmann, V.A., A. Terrier, and D.P. Pioletti, *Microstimulation at the bone-implant interface upregulates osteoclast activation pathways*. Bone, 2008. **42**(2): p. 358-64.

241. Scholes, S.C., et al., *The Location and Friction of Conventional UHMWPE, Novel Compliant Layer, and Hard Bearing Surfaces for use in Total Hip Prostheses*, in *Friction, Lubrication and Wear of Artificial Joints*, I.M. Hutchings, Editor. 2003, John Wiley & Sons.
242. *ASTM F1978-12, Standard Test Method for Measuring Abrasion Resistance of Metallic Thermal Spray Coatings by Using the Taber Abrase*. 2012, ASTM International: West Conshohocken, PA.
243. Chen, Q., D.Y. Li, and B. Cook, *Is porosity always detrimental to the wear resistance of materials?—A computational study on the effect of porosity on erosive wear of TiC/Cu composites*. *Wear*, 2009. **267**(5–8): p. 1153-1159.
244. Vardavoulias, M., C. Jouanny-Tresy, and M. Jeandin, *Sliding-wear behaviour of ceramic particle-reinforced high-speed steel obtained by powder metallurgy*. *Wear*, 1993. **165**(2): p. 141-149.
245. Malyshev, V., A. Volkhin, and B. Gantimirov, *Tribological Characteristics Improvement of Wear Resistant MAO-Coatings*. *Journal of Coatings*, 2013. **2013**.
246. ZHANG, L., et al., *Effect of porosity on wear resistance of SiC p/Cu composites prepared by pressureless infiltration*. *Transactions of Nonferrous Metals Society of China*, 2008. **18**(5): p. 1076-1082.
247. Di Prima, M.A. and G.I.o. Technology, *Thermo-mechanical and Micro-structural Characterization of Shape Memory Polymer Foams*. 2009: Georgia Institute of Technology.
248. Schraad, M.W. and F.H. Harlow, *A stochastic constitutive model for disordered cellular materials: Finite-strain uni-axial compression*. *International Journal of Solids and Structures*, 2006. **43**(11–12): p. 3542-3568.
249. Ji, S., Q. Gu, and B. Xia, *Porosity dependence of mechanical properties of solid materials*. *Journal of Materials Science*, 2006. **41**(6): p. 1757-1768.
250. Jones, D.P., D.C. Leach, and D.R. Moore, *Speciality Polymers 84 Mechanical properties of poly(ether-ether-ketone) for engineering applications*. *Polymer*, 1985. **26**(9): p. 1385-1393.
251. Hainsworth, S., T. Bartlett, and T. Page, *The nanoindentation response of systems with thin hard carbon coatings*. *Thin Solid Films*, 1993. **236**(1): p. 214-218.
252. Burnett, P. and D. Rickerby, *Assessment of coating hardness*. *Surface engineering*, 1987. **3**(1): p. 69-76.
253. Chechenin, N., J. Böttiger, and J. Krog, *Nanoindentation of amorphous aluminum oxide films I. The influence of the substrate on the plastic properties*. *Thin Solid Films*, 1995. **261**(1): p. 219-227.

254. Saha, R. and W.D. Nix, *Effects of the substrate on the determination of thin film mechanical properties by nanoindentation*. Acta Materialia, 2002. **50**(1): p. 23-38.
255. Gamonpilas, C. and E.P. Busso, *On the effect of substrate properties on the indentation behaviour of coated systems*. Materials Science and Engineering: A, 2004. **380**(1): p. 52-61.
256. Bilbrey, J. *Removing substrate effects from nanoindentation measurements*. June 11 2015.
257. Rohlmann, A., et al., *Activities of Everyday Life with High Spinal Loads*. PLoS ONE, 2014. **9**(5): p. e98510.
258. Ferguson, S.J., J.M. Visser, and A. Polikeit, *The long-term mechanical integrity of non-reinforced PEEK-OPTIMA polymer for demanding spinal applications: experimental and finite-element analysis*. Eur Spine J, 2006. **15**(2): p. 149-56.
259. Maksimov, R. and J. Kubat, *Time and temperature dependent deformation of poly(ether ether ketone) (PEEK)*. Mechanics of Composite Materials, 1997. **33**(6): p. 517-525.
260. Walsh, W.R., et al., *Plasma-sprayed titanium coating to polyetheretherketone improves the bone-implant interface*. The Spine Journal, 2015. **15**(5): p. 1041-1049.

VITA
NATHAN TIMOTHY EVANS

Nathan was born in Normal, IL and resided there until he was eight years old. In 1996, his family moved to Kennesaw, GA immediately after the conclusion of the Olympic Summer Games in Atlanta. Nathan graduated in 2007, from Kennesaw Mountain High School where he played basketball, golf, alto saxophone in the concert band, was voted most dependable in his class, and excelled in math and science. Initially undecided on his major, Nathan began his undergraduate studies at Georgia Tech in Atlanta, GA and quickly decided on Materials Science and Engineering for its practical applications and diversity of career options. After his freshman year, Nathan began a three year co-op at MedShape, an Atlanta-based orthopaedic implant startup, and this opportunity shaped the rest of his academic career. At MedShape, Nathan met Dr. Ken Gall, co-founder and CTO and also a professor at Georgia Tech. The fascinating work and the mentorship provided by Ken Gall led Nathan to continue working for him as an undergraduate researcher in the Advanced Materials Lab at Georgia Tech. Upon graduation, Nathan began his doctorate as a National Science Foundation Research Fellow in Materials Science and Engineering under Ken Gall. Outside of work, Nathan enjoys all things outdoors, exercising, travelling, and spending time with his wife, Raina.